Chapter 3
Low- and Intermediate-Mass Stars

Maria Lugaro and Alessandro Chieffi

Energy in stars is provided by nuclear reactions, which, in many cases, produce radioactive nuclei. When stable nuclei are irradiated by a flux of protons or neutrons, capture reactions push stable matter out of stability into the regime of unstable species. The ongoing production of radioactive nuclei in the deep interior of the Sun via proton-capture reactions is recorded by neutrinos emitted during radioactive decay. These neutrinos escape the inner region of the Sun and can be detected on Earth. Radioactive nuclei that have relatively long half lives may also be detected in stars via spectroscopic observations and in stardust recovered from primitive meteorites via laboratory analysis. The vast majority of these stardust grains originated from Asymptotic Giant Branch (AGB) stars. This is the final phase in the evolution of stars initially less massive than $\simeq 10\,M_{\odot}$, during which nuclear energy is produced by alternate hydrogen and helium burning in shells above the core. The long-lived radioactive nucleus ^{26}Al is produced in AGB stars by proton captures at relatively high temperatures, above 60 MK. Efficient production of ^{26}Al occurs in massive AGB stars ($> 4:5\,M_{\odot}$), where the base of the convective envelope reaches such temperatures. Several other long-lived radioactive nuclei, including ^{60}Fe, ^{87}Rb, and ^{99}Tc, are produced in AGB stars when matter is exposed to a significant neutron flux leading to the synthesis of elements heavier than iron. Here, neutron captures occur on a timescale that is typically slower than β-decay timescales, resulting in a process known as *slow* neutron captures (the *s*-process). However, when radioactive

M. Lugaro (✉)
Monash Centre for Astrophysics, Monash University, Clayton, VIC, Australia

Konkoly Observatory, Research Centre for Astronomy and Earth Sciences, Hungarian Academy of Sciences, Budapest, Hungary
e-mail: maria.lugaro@csfk.mta.hu

A. Chieffi
Istituto Nazionale Astronomia Fisica INAF, Roma, Italy
e-mail: achieffi@iasf-roma.inaf.it

R. Diehl et al. (eds.), *Astrophysics with Radioactive Isotopes*, Astrophysics and Space Science Library 453, https://doi.org/10.1007/978-3-319-91929-4_3

nuclei with half lives greater than a few days are produced, depending on the temperature and the neutron density, they may either decay or capture a neutron, thus branching up the path of neutron captures and defining the final *s*-process abundance distribution. The effect of these *branching points* is observable in the composition of AGB stars and stardust. This nucleosynthesis in AGB stars could produce some long-living radioactive nuclei in relative abundances that resemble those observed in the early solar system.

3.1 The Missing Element

The element with 43 protons in its nucleus, lying between molybdenum and ruthenium, was known for a long time as the *missing* element. Since the nineteenth century there had been many unsuccessful attempts at its discovery. Finally, in 1937 Italian physicist Emilio Segré and chemist Carlo Perrier found two isotopes of the missing element through measurements of radioactivity from discarded cyclotron parts: they observed several decay periods and proved they were occurring at Z=43. Hence the missing element did not exist in nature because of its instability against nuclear decay. The discoverers named the missing element technetium (Tc), from $\tau\epsilon\chi\nu\eta\tau\acute{o}\varsigma$, which means artificial in Greek, since it was the first element produced artificially. Fifteen years later, it was shown that Tc is not only made by men but also by stars. In 1952, astronomer Paul Merrill observed the absorption lines corresponding to the atomic structure of Tc in the spectra of several giant stars. Merrill was at first cautious about this result. To start with, the element he identified did not even exist on Earth. Second, up to then it was assumed, and not proved wrong, that all stars had the same chemical composition. This was in agreement with the accepted theory of the time that the elements were all produced during the Big Bang and their abundances in the Universe were not modified by any further process. Merrill's discovery in that respect was truly revolutionary: given the relatively short half lives of the Tc isotopes (a few Myrs at most), the Tc lines were the first indisputable demonstration that this radioactive element was made *in situ* in the stars where it was observed. This finding brought a radical change in the way we understand the origin of the elements, and the theory of stellar nucleosynthesis introduced in Chap. 2 began to take shape and garnered authority. In this chapter we discuss the life of those stars that, like our Sun, evolve twice through Red Giant stages. We describe how they produce long lived radioactive nuclei, like Tc, in their interiors, how the signature of such radioactivity is carried outside the star, and how it can be observed.

3.2 The Production of Radioactive Nuclei in Stellar Interiors

In Sect. 3.2.1 we first derive the four basic equations that control the quasi-equilibrium configuration of a self-gravitating gas sphere, namely, the hydrostatic equilibrium equation (that describes the balance between the pressure gradient and

gravity) and the energy transport equation (due to photons and/or convection), plus the two associated continuity equations for mass and energy flux. Then, we show that energy losses, which occur mainly from the stellar surface in stars of mass less than $\sim 10\,M_{\odot}$, force the gas to contract and to heat, in accordance with the virial theorem. The progressive increase of the central temperature allows the activation of nuclear processes and we describe two sequences that convert protons into ^{4}He nuclei (α particles): the PP chain and the CNO cycle. Since proton capture inevitably pushes matter out of the stability, both these sequences produce radioactive nuclei that decay by emitting neutrinos.

In Sect. 3.2.2 we briefly describe the quest for solar neutrinos and the various experiments that eventually allowed the demonstration that the lower than predicted neutrino flux from the Sun (the so-called Solar Neutrino Problem) is the consequence of neutrino oscillations among their three different flavors.

3.2.1 The Stellar Energy Source and Radioactive Isotopes

A star is, in first approximation, a spherically symmetric, gaseous cloud contracting under its own gravity and progressively heating up while losing energy from its surface in the form of photons. A strong temperature gradient, with the temperature decreasing from the centre to the surface, pushes the photon flux outward until the *mean free path*[1] of the photons eventually becomes larger than their distance from the surface, allowing their escape. The Virial theorem links the energy gained by the gravitational field $\Delta\Omega$ to that absorbed by the gas ΔU: $\Delta U = -\Delta\Omega/3(\gamma - 1)$, where γ is the ratio between two specific heats, that at constant pressure and that at constant volume, of the contracting gas. A stable quasi-equilibrium configuration exists for such a structure provided that $\gamma > 4/3$. In this case, a fraction of the energy gained by the gravitational field must be liberated from the structure before the gas cloud can contract further. In the case of a perfect gas ($\gamma = 5/3$) we obtain the classical result $\Delta U = -(1/2)\Delta\Omega$, stating that half of the gravitational energy liberated by each infinitesimal contraction is absorbed by the gas and half must be lost before an additional contraction can occur. The timescale over which the energy is lost from the system drives the timescale of contraction and keeps the structure in a quasi-equilibrium configuration. If, instead, γ drops to 4/3, all the gravitational energy is absorbed by the gas and no time delay is required before a new contraction can occur. This is an unstable situation leading to collapse. In the evolutionary phases we discuss in this chapter γ remains well above 4/3 and hence a stable quasi-equilibrium configuration is always assured.

The balancing forces required to maintain a stable stellar quasi-equilibrium configuration are due to pressure gradients and gravity. So, the first main equation of stellar structure describes the equilibrium between these two forces, at any given

[1] The average distance a particle travels between collisions.

distance from the center of the star r:

$$dP/dr = -GM\rho/r^2 \tag{3.1}$$

where P is the pressure, G the gravitational constant, M the cumulative mass inside r, and ρ the density. Associated to this equation is a continuity equation for mass:

$$dM/dr = 4\pi r^2 \rho. \tag{3.2}$$

By assuming, to zero order, that ρ is constant within the star, the integration of Eq. (3.2) implies that:

$$\rho \propto M/R^3. \tag{3.3}$$

Since the pressure at the surface of the star is much lower than where the radius approaches zero, the center of the star, the equation of hydrostatic equilibrium, (3.1), basically says that

$$P_c \propto M\rho/R_s \tag{3.4}$$

where P_c is the central pressure and R_s the stellar radius. By inserting the relation (3.3) into (3.4) one obtains:

$$P_c \propto M^2/{R_s}^4. \tag{3.5}$$

If the equation of state is that of a perfect gas, i.e. $P \propto \rho\, T/\mu$, relation (3.5) becomes:

$$T_c \propto \mu\, M/R \tag{3.6}$$

where T is the temperature and μ is the mean molecular weight. This equation provides an important basic relationship among central temperature (T_c), mass, and radius of a star, which only relies on the assumption of hydrostatic equilibrium.

The second major equation describing the structure of the quasi-equilibrium configuration of a star determines the energy flux through the structure. In stationary situations the energy is transported by photons or electrons and application of the first Fick's law leads to the well known equation:

$$dT/dr = -3\kappa\rho L/(16ac\pi r^2 T^3) \tag{3.7}$$

where κ is the opacity coefficient representing the impenetrability of a gas to light, L the luminosity representing the amount of energy radiated per unit time, a the radiation constant, and c the speed of light. Furthermore, in this case a continuity equation

$$dL/dr = 4\pi r^2 \rho\epsilon \tag{3.8}$$

controls the conservation of energy, where ϵ represents the net local energy budget, i.e., the sum of the nuclear energy production rate $\epsilon_{\rm nuc}$, the neutrino energy loss rate ϵ_ν, and the gravitational energy rate $\epsilon_{\rm g}$. Since the central temperature T_c is much higher than the surface temperature, it is possible to obtain a basic relationship between central temperature, mass, luminosity and radius of a star, i.e.:

$$T_c^{\,4} \propto ML/R^4. \tag{3.9}$$

By combining this relation with the previous relation (3.6), derived from hydrostatic equilibrium (3.1), one eventually obtains the fundamental relation between mass and luminosity:

$$\mathrm{L} \propto \mu^4 \mathrm{M}^3. \tag{3.10}$$

Frequently, the energy produced locally cannot be transported quickly enough by radiation or conduction, and interior shells formally in an equilibrium condition can become unstable in the sense that a displacement from their equilibrium position is not fully counteracted by a restoring force. Instead, matter is accelerated even further from its original position and large scale motions of matter (*convection*) is established. Under these conditions energy is predominantly transported by buoyancy-driven motions of bulk material due to their much larger mean free path with respect to that of photons. A temperature gradient quite different from that described by Eq. (3.7) must then be used in these regions. A direct consequence of these large scale motions is that matter is mixed throughout an unstable region.

The system formed by the two basic equations related to hydrostatic equilibrium and energy transport plus the two associated continuity equations and the equation of state (supplemented by an opacity coefficient $\kappa = f(\rho, T, \text{chem.comp.})$ and a total energy generation coefficient $\epsilon = f(\rho, T, \text{chem.comp.})$) constitutes the basic set of equations that describes the internal structure of a quasi-equilibrium (non rotating) stellar configuration at a given time. The temporal evolution of such a structure is determined by the rate at which energy is lost to the surroundings: the faster the energy is lost, the faster the structure evolves. Typical stellar luminosities range between $\sim 4 \times 10^{33}$ erg/s for a star of $1\,\mathrm{M}_\odot$ and $\sim 4 \times 10^{36}$ erg/s for a star of $6\,\mathrm{M}_\odot$ and the associated lifetimes can be estimated by dividing the total amount of available energy by the loss rate L, i.e. the stellar luminosity. If the only energy source was the gravitational field, the lifetime of a contracting gas cloud would be of the order of a few tens of millions of years (the Kelvin-Helmholtz timescale). Instead, as was known since the 1920s from radioactive dating of terrestrial rocks, that the age of the Earth is several Gyrs, much longer than the Kelvin-Helmholtz timescale. Thus, the Sun must be powered by different means. The lifetime of most stars is much larger than permitted by their gravitational energy reservoir alone. Instead of simple contraction, energy losses are replaced by the activation of nuclear fusion reactions among charged nuclear particles near the stellar core.

The efficiency of nuclear reactions, i.e., their *rate*, depends on the abundances of the reactant nuclei and the cross section of each reaction averaged over a Maxwellian

distribution of relative velocities between the target and the projectile nuclei. For charged particle reactions the rate is mainly controlled by the Coulomb barrier generated by the number of protons in a nucleus. The nuclear reactions that activate at the lowest temperatures are those involving capture of protons, i.e., the nucleus of the lightest and most abundant element: hydrogen (H). Nature, however, does not allow the build up of stable nuclei made only of protons because in order to glue nucleons (i.e., proton and neutrons) together in a nucleus via the strong nuclear force, the repulsive electromagnetic force acting between protons needs to be diluted with a certain number of neutrons. The distribution of stable nuclei in the [N=number of neutrons, Z=number of protons] plane, the *chart of nuclides*, clearly shows that the region where nuclei are stable lies close to the N=Z line (the *valley of* β *stability*) up to the element Ca, and then bends slightly towards the neutron-rich side as the repulsion between higher number of protons needs to be diluted with more and more neutrons. Nuclei outside this valley are radioactive, i.e., unstable, and decay towards their closest stable daughter through β-decay weak interaction reactions (as described in Chaps. 1, 2, 4, and 9). It follows that the build up of progressively heavier nuclei through the addition of protons naturally pushes the matter out of the stability valley, producing radioactive nuclei that decay back towards stability via β^+ decay.

A detailed analysis of the nuclear reactions involving the fusion of protons (H burning) foresees the existence of two processes. The PP chain activates at temperatures $\simeq$10 MK and operates through a sequence of proton captures and β decays starting with a weak interaction p+p fusion. The processes involved in the PP chain are listed in Table 3.1 together with the mass defect (Q values) in MeV and the energy carried away by neutrinos. If the neutrino emission is described by an energy continuum, the maximum energy of this spectrum is reported. A direct build up of progressively heavier nuclei through successive proton captures stops very early, at ^{3}He, because of the low cross section of the ^{3}He+p reaction. Also, proton captures on the second most abundant isotope, ^{4}He (or α particle, $N = Z = 2$), cannot even begin, because nuclei with atomic mass number A=N+Z=5 are unstable and hence rarely available as reaction targets for proton capture. In order to proceed with proton captures beyond ^{3}He it is necessary to build up enough ^{3}He nuclei

Table 3.1 The reactions of the PP chain of burning H to He

Reaction	Q_{tot} (MeV)	Q_ν (MeV)
$p + p \rightarrow d + e^+ + \nu$	1.442	0.42(spectrum)
$d + p \rightarrow {}^3He$	5.494	
${}^3He + {}^3He \rightarrow {}^4He + 2p$	12.860	
${}^3He + {}^4He \rightarrow {}^7Be$	1.587	
${}^7Be + e^- \rightarrow {}^7Li + e^+ + \nu$	0.862	0.861(90%)−0.383(10%) (lines)
${}^7Be + p \rightarrow {}^8B \rightarrow {}^8Be + e^+ + \nu \rightarrow 2\alpha$	18.209	14.060(spectrum)
${}^7Li + p \rightarrow {}^8Be \rightarrow \alpha + \alpha$	17.347	

to activate the capture of this nucleus by either another ^{3}He nucleus, or ^{4}He. The activation of ^{3}He captures allows to overcome the non-existence of nuclei with A=5, though it still does not allow the build up of an appreciable amount of nuclei heavier than He. In fact, the product of the ^{3}He+^{3}He reaction is an α particle plus two protons, while the product of the ^{3}He+^{4}He reaction is ^{7}Be, whose fate, either proton or electron capture leads to the formation of ^{8}Be, which very quickly decays in two α particles. In synthesis, the fusion of H mainly produces He, together with a number of radioactive nuclei that decay into their respective stable daughter nuclei emitting a neutrino. The energies and the number of neutrinos produced in these decays reflect the relative importance of the various PP-chain branches and the efficiency of the nuclear reactions in stars.

The second process converting protons to α particles is the CNO cycle. Given the high Coulomb barrier of the CNO nuclei, this cycle becomes efficient at temperatures (T $>$ 20 MK), significantly higher than those relevant to the PP chain. The main section of this sequence is characterized by the continuous conversion of C to N and viceversa. Let us start, e.g., with the capture of a proton by a ^{12}C (Table 3.2). The outcome of this fusion is the radioactive nuclide ^{13}N that quickly decays β^{+} into ^{13}C. Efficient proton captures by ^{13}C lead to the synthesis of ^{14}N. Proton captures by ^{14}N produce ^{15}O, a radioactive nuclide that quickly decays in ^{15}N. The fusion of a proton and a ^{15}N particle has, as the main outcome, a ^{12}C nucleus plus an α particle. The sequence sketched above is called the CN cycle. If the temperature exceeds T $\sim$ 25–30 MK, also oxygen enters the game and the full CNO cycle activates: ^{16}O begins to capture protons forming radioactive ^{17}F that decays to ^{17}O. The capture of a proton by this particle leads to a compound nucleus that preferentially splits into ^{14}N and an α particle, and that partly turns into ^{18}F, which quickly decays to ^{18}O. Proton captures on ^{18}O produce preferentially ^{15}N

Table 3.2 The individual reactions of the CNO cycle of H burning, together with their respective reaction Q values

Reaction	Q_{tot} (MeV)
$^{12}C + p \rightarrow ^{13} N$	1.944
$^{13}N \rightarrow ^{13} C + e^{+} + \nu$	2.220
$^{13}C + p \rightarrow ^{14} N$	7.551
$^{14}N + p \rightarrow ^{15} O$	7.297
$^{15}O \rightarrow ^{15} N + e^{+} + \nu$	2.754
$^{15}N + p \rightarrow ^{12} C + \alpha$	4.966
$^{15}N + p \rightarrow ^{16} O$	12.127
$^{16}O + p \rightarrow ^{17} F$	0.600
$^{17}F \rightarrow ^{17} O + e^{+} + \nu$	2.761
$^{17}O + p \rightarrow ^{14} N + \alpha$	1.192
$^{17}O + p \rightarrow ^{18} F$	5.607
$^{18}F \rightarrow ^{18} O + e^{+} + \nu$	1.656
$^{18}O + p \rightarrow ^{15} N + \alpha$	3.981
$^{18}O + p \rightarrow ^{19} F$	7.994

plus an α particle. The activation of the channel ^{15}N(p,γ)^{16}O closes the NO cycle, processing material back into oxygen. The total abundance by number of the CNO isotopes remains constant with time because the proton capture on any of them (and the subsequent β^+ decays) just produce another isotope in the same set.

For T > 25–30 MK, the full CNO cycle becomes efficient and quickly reaches a quasi-equilibrium in which the abundance of each nucleus settles on a steady state value determined by the balance between its production and destruction. For example, the equilibrium abundance of ^{13}C (assuming that ^{13}N decays instantaneously) is given by:

$$\frac{dY_{^{13}C}}{dt} = Y_{^{12}C}\ Y_p\ \rho\ N_A\ <\sigma\ v>_{^{12}C+p}\ -\ Y_{^{13}C}\ Y_p\ \rho\ N_A\ <\sigma\ v>_{^{13}C+p} = 0$$

where Y_i refers to the abundance by number of a given species i, t is time, ρ is the density, N_A is Avogadro's number and $<\sigma\ v>_j$ is the Maxwellian averaged product of the velocity v times the nuclear cross section σ for a given capture j. The equilibrium condition immediately gives:

$$\frac{Y_{^{12}C}}{Y_{^{13}C}} = \frac{<\sigma\ v>_{^{13}C\ p}}{<\sigma\ v>_{^{12}C\ p}}$$

which means that the relative abundances between isotopes of the CNO cycle depend only on the ratio between the respective cross sections for proton capture. Typical isotopic and elemental ratios obtained in the temperature range 30 ≤ T ≤ 100 MK are given in Table 3.3.

The neutrinos emitted by the decay of radioactive nuclei synthesized by the CNO cycle have characteristic energies different from those emitted by the PP chain. Their detection would provide precious information about the relative efficiency of the various reactions involved in the CNO cycle.

In addition to the PP chain and the CNO cycle there is another sequence of proton captures that can become efficient in stars, although it does not play a role in the energy budget. In the temperature range 40–50 MK the proton captures listed in the upper part of Table 3.4 quickly bring to their equilibrium values the

Table 3.3 Typical isotopic ratios of the fully-developed CNO cycle of hydrogen burning

Isotopic ratio	Value	Value (solar)
$Y_{^{12}C}/Y_{^{13}C}$	$\simeq$4	89
$Y_{^{14}N}/Y_{^{15}N}$	$\simeq 4\times10^4$–10^5	272
$Y_{^{17}O}/Y_{^{16}O}$	$\simeq 10^{-2}$–10^{-3}	3.8×10^{-4}
Y_C/Y_N	$\simeq 7\times10^{-3}$–2.5×10^{-2}	3.2
Y_N/Y_O	$\simeq$60–350	0.13
$Y_{^{18}O}/Y_{^{16}O}$	$\simeq 2\times10^{-6}$ for $T < 50 : 60\,MK$	2×10^{-3}
$Y_{^{18}O}/Y_{^{16}O}$	Declines to $\simeq 5\times10^{-8}$ at T$\simeq$100 MK	2×10^{-3}

Table 3.4 The reactions of the Ne-Na-Mg-Al cycle, and their reaction Q values

Reaction	Q_{tot} (MeV)
$^{20}Ne + p \rightarrow ^{21} Na$	5.979
$^{21}Na \rightarrow ^{21} Ne + e^+ + \nu$	3.548
$^{21}Ne + p \rightarrow ^{22} Na$	6.739
$^{22}Na \rightarrow ^{22} Ne + e^+ + \nu$	2.842
$^{22}Ne + p \rightarrow ^{23} Na$	8.794
$^{23}Na + p \rightarrow ^{20} Ne + \alpha$	2.377
$^{23}Na + p \rightarrow ^{24} Mg$	11.693
$^{24}Mg + p \rightarrow ^{25} Al$	6.548
$^{25}Al \rightarrow ^{25} Mg + e^+ + \nu$	4.277
$^{25}Mg + p \rightarrow ^{26} Al$	6.307
$^{26}Al \rightarrow ^{26} Mg + e^+ + \nu$	4.004
$^{26}Al + p \rightarrow ^{27} Si$	12.275
$^{26}Mg + p \rightarrow ^{27} Al$	8.271
$^{27}Si \rightarrow ^{27} Al + e^+ + \nu$	4.812
$^{27}Al + p \rightarrow ^{28} Si$	11.585
$^{27}Al + p \rightarrow ^{24} Mg + \alpha$	1.601

abundances of ^{20}Ne, ^{21}Ne, ^{22}Ne, and ^{23}Na, forming also in this case a *NeNa* cycle. For temperature in excess of 50 MK the ^{23}Na(p,γ)^{24}Mg channel competes with the ^{23}Na(p,α)^{20}Ne so that matter from the NeNa cycle leaks towards more massive nuclei. At temperatures of order of 60 MK also the proton captures listed in the lower part of Table 3.4 fully activate so that all the nuclei between ^{20}Ne and ^{27}Al reach their equilibrium abundances. Is it worth noting that ^{26}Al, a long-lived radioactive nucleus with half life 7.17×10^5 years, is included within this sequence. ^{26}Al can be ejected into the interstellar medium by stellar outflows (winds) and its decay into ^{26}Mg can be detected as diffuse γ-ray emission (Sect. 7.4) when the metastable ^{26}Mg relaxes towards its ground state. Moreover, it can be included in dust grains that form around stars and decay within the already formed minerals. This nucleus is thoroughly discussed in Sect. 3.6.1, and in Chaps. 4, 7 and 9. Typical $Y_{^{26}Al}/Y_{^{27}Al}$ equilibrium ratios produced by H burning range between 3×10^{-2} at 60 MK and 0.8 at 100 MK. We refer the reader to the book by Cox and Giuli (1968) for a derivation of the basic stellar structure equations and detailed discussions of the physics involved in the study of stellar evolution.

Although the sequences of nuclear reactions that power stellar luminosity are now considered to be well understood, a wise Galilean approach suggests to verify experimentally (whenever possible) their occurrence in stars. Our Sun provides a unique opportunity to accomplish such verification via the detection of neutrinos produced by radioactive decay in its deep interior.

3.2.2 *The Sun: Neutrinos and the Nuclear Origin of Starlight*

The long-term stability of the Solar properties, in particular its luminosity and surface temperature, can be explained only if the solar energy source is of nuclear origin and specifically involves proton captures, which are associated with abundant fuel and a long time scale. As discussed above, such an energy source inevitably results in the production of radioactive nuclei, which decay into their stable daughter nuclei through weak processes, hence emitting neutrinos. The modeling of the internal structure of the Sun predicts a central temperature at present of the order of 15 MK, and hence that the PP chain dominates (99.6%) over the CNO cycle (0.4%) converting H into ^{4}He. The relative importance of the nuclear reactions in the PP chain in the Sun leads to the result that the majority (93%) of the neutrinos produced should come from $p(p, e^+\nu_e)d$ reactions (where d=deuterium, N=Z=1) and be of relatively low energy ($E \leq 0.42$ MeV, see Table 3.1), while only a minor fraction of the total neutrinos is expected to be emitted by the decay of ^{7}Be ($\simeq$7%, $E \simeq 0.86$ MeV) and ^{8}B(0.0075%, $E < 15$ MeV).

Figure 3.1 shows the rates of the nuclear reactions intervening in the PP chain and CNO cycle as a function of the mass coordinate for a 1 $M_\odot$ stellar model of

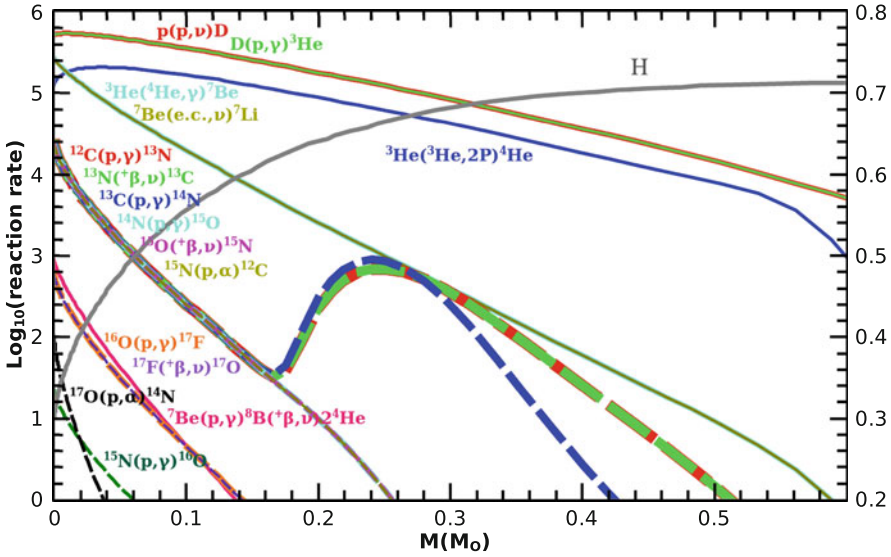

Fig. 3.1 Rates of the reactions involved in the PP chain and the CNO cycle as a function of the mass coordinate in a solar-like stellar model having approximately the age of the Sun of 4.6 Gyr. The H abundance is also plotted and its range shown on the right-side *y*-axis

solar "metallicity"[2] and an age close to the present age of the Sun, i.e., 4.6 Gyr. All the β^+ decays are concentrated very close to the center where the synthesis of unstable nuclei is concentrated. The relative importance of the various PP reactions, and hence of the associated neutrino fluxes, depend on the rates of the nuclear reactions involved, which, in turn, are a function of the density, temperature, and chemical composition. Since the internal structure of a model of the Sun depends on the adopted and somewhat uncertain input physics—e.g., the nuclear cross sections, the equation of state, the opacity, and the chemical composition of the gas from which the Sun formed—the detection of neutrinos from the Sun is fundamental not only to experimentally verify the nuclear origin of the Solar luminosity, but also to confirm the overall reliability of the modeling of the internal structure of the Sun and the adopted input physics.

It is therefore comprehensible that the quest for the solar neutrinos started early, more than 40 years ago, with the Davis experiment (1967–1985) (Bahcall et al. 1985; Cleveland et al. 1998). This experiment, based on the interaction between an electron neutrino and ^{37}Cl, has a threshold energy of the order of 0.8 MeV and hence could detect predominantly the ^{8}B neutrinos, which constitute a very minor fraction of the neutrino flux coming from the Sun. The Davis experiment provided two basic results, one very encouraging and another one very stimulating. First, it detected solar neutrinos, demonstrating beyond any doubt that proton captures are occurring in the interior of the Sun. Second, the detected neutrino flux was roughly one third of the predicted value. Such a result stimulated much further work and a huge amount of papers on this puzzle piled up over the decades. The discrepancy was considered by many physicists as a strong indication that the basic modeling of the Sun was wrong though, however, it must be reminded that it was confined to a very minor branching of the PP chain. The discrepancy became more serious with the advent of the GALLEX experiment (Hampel et al. 1998)—a collaboration among France, Germany, Italy, Israel, Poland, and USA, headed by MPIK Heidelberg, 1991–1997—and the SAGE experiment (Abdurashitov et al. 1999)—a Russian-American collaboration, 1990–2000. These modern sophisticated experiments were designed to detect the bulk of the neutrinos produced in the Sun, i.e., the low energy neutrinos produced by the p+p reaction. They confirmed both the detection of a firm neutrino signature from the Sun and the existence of a discrepancy between theoretical and observed fluxes. This result plunged the basics of solar modeling into a deep crisis because these experiments were sensible to the total number of electron neutrinos emitted by the Sun. This number is theoretically extremely robust, depending only on the basic assumption that the solar luminosity comes from the conversion of protons into α particles, and not on the details of the modeling of the internal structure of the Sun or of the cross sections of the nuclear reactions involved.

[2]The term metallicity indicates the abundance of metals in a star, where metals corresponds to all elements heavier than He. The metallicity of the Sun is $\simeq$0.02 by mass fraction, where abundances are normalised to a total of 1, which means that 2% of the solar matter is made up of elements heavier than He. The most abundant of these is oxygen, followed by carbon.

If the solar luminosity is powered by the conversion of protons into α particles, the total number of electron neutrinos emitted per second by the Sun must be 2.38×10^{39} ($L_\odot$ in MeV/s)/25 (energy provided per α nucleus in MeV) $\times$ 2 (number of ν_e produced per α nucleus) [ν_e s^{-1}], which corresponds, at one astronomical unit, to a flux equal to 6.78×10^{10} ν_e s^{-1}. Instead, the number of neutrinos detected by GALLEX and SAGE was half this predicted value.

One of the possible solutions of this puzzling result was identified since the 1960s (Gribov and Pontecorvo 1969) in the possible oscillation of neutrinos of different flavors, ν_e and ν_μ (ν_τ was discovered in 1975), a phenomenon that would have implied a non zero mass for the neutrinos. Such a solution was not considered very seriously up to the middle of the 1980s because the fit to the observed rate of the solar neutrinos would have required a very efficient oscillation among the three neutrinos flavours, a possibility thought to be quite improbable. However, Wolfenstein (1978) first and Mikheyev and Smirnov (1985) proposed what is presently called the Mikheyev-Smirnov-Wolfenstein (MSW) effect, i.e., that under proper conditions, in particular at high densities, the oscillation of the neutrinos could be strongly enhanced as a result of a coherent forward scattering when passing through matter. Such a revolutionary insight was among the reasons that led to the birth of the Sudbury Solar Neutrino Observatory (SNO) experiment (a Canadian, USA, and UK collaboration that started in 1985, McDonald et al. 2002), designed to detect all the three flavors of neutrinos. The adopted strategy was to catch neutrinos via three reactions:

$$\nu_{e^-} + {}^2H \rightarrow p + p + e^-$$

$$\nu_x + {}^2H \rightarrow p + n + \nu_x$$

$$\nu_x + e^- \rightarrow \nu_x + e^-$$

where x stands for e^-, μ or τ. The activation of these reactions required the building of an extremely clean detector filled with 1000 tonnes of heavy water. Data were collected in various phases between 1999 and 2006. Though the energy threshold for this experiment was around 6 MeV, so that only neutrinos emitted from the minor branch ^{7}Be(p,γ)^{8}B(e^+ ν_e)^{8}Be could be detected, this experiment showed unequivocally that neutrinos oscillate and put strong constraints on their physics. A proper inclusion of this result on the interpretation of the neutrinos emitted by the Sun led to a much better agreement between the expected and the observed neutrinos fluxes.

In spite of the great results obtained by the SNO experiment, it remained the fact that its very high energy threshold prevented the detection of the bulk of the neutrinos, that are emitted with much lower energies, of the order 200–300 keV. The following big step forward in the direction of both a better understanding of our Sun and also of the physics of the neutrinos was done with the advent of Borexino, an experiment designed to detect neutrinos over a large energy spectrum via the $\nu_x + e^- \rightarrow \nu_x + e^-$ reaction (where again x stands for e^-, μ or τ). It consists

of an unsegmented liquid detector featuring 300 tonnes of well shielded ultra pure scintillator viewed by 2200 photomultipliers. It was designed to drastically reduce the energy threshold to extremely low energies: roughly 250 keV. This experiment is located in Hall C of the Laboratori Nazionali del Gran Sasso in Italy and data started to be collected since 2007 and continued up to 2013. At present all three neutrinos fluxes produced by the PP chain where measured with unprecedented accuracy: $\Phi(\mathrm{PP}) = 6.6 \pm 0.7 \times 10^{10}\ \mathrm{cm^{-2}\,s^{-1}}$ (BOREXINO Collaboration et al. 2014), $\Phi(^7\mathrm{Be}) = 5.18 \pm 0.51 \times 10^{9}\ \mathrm{cm^{-2}\,s^{-1}}$ (Arpesella et al. 2008) and $\Phi(^8\mathrm{B}) = 2.4 \pm 0.4 \times 10^{6}\ \mathrm{cm^{-2}\,s^{-1}}$ (Bellini et al. 2010). These fluxes are in good agreement with the latest models of the Sun. For example Serenelli et al. (2011) published a very refined standard solar model (SSM) computed for two different initial chemical compositions of the Sun, i.e., Asplund et al. (2009) and Grevesse and Sauval (1998). For the Φ(PP) they obtain 6.03 ± 0.006 and 5.98 ± 0.006 ($10^{10}\,\mathrm{cm^{-2}\,s^{-1}}$) in the two cases, respectively. These two fluxes are very similar to each other and in excellent agreement with the one measured by the Borexino collaboration. As for the ^{7}Be branch, the two predicted fluxes are $\Phi(^7\mathrm{Be}) = 4.56 \pm 0.07$ and 5.00 ± 0.07 ($10^9\ \mathrm{cm^{-2}\,s^{-1}}$). In this case the flux predicted by the SSM computed by assuming the metallicity of Grevesse and Sauval (1998) is closer to the detected one. As for the $\Phi(^8\mathrm{B})$ the SSM predicts, for the two initial metallicities, 4.59 ± 0.14 and 5.58 ± 0.14 ($10^6\,\mathrm{cm^{-2}\,s^{-1}}$) and in this case the flux predicted by adopting the metallicity derived by Asplund et al. (2009) is the closest to that detected (even if somewhat higher).

The Borexino experiment was also able to detect neutrinos emitted by the very inefficient reaction $\mathrm{p} + \mathrm{p} + \mathrm{e}^- \ =^2\ \mathrm{H} + \nu_\mathrm{e}^-$ (pep), and also in this case the predicted and detected fluxes converge towards a similar value: Φ(pep)=$1.46 \pm 0.01(10^8\,\mathrm{cm^{-2}\,s^{-1}})$. Though it was not yet possible to detect neutrinos emitted by the processes involved in the CNO cycle, this experiment was capable to put stringent limits to their fluxes.

3.2.3 Solar Flares and Radioactivities

The Sun and the phenomenon of flaring high-energy particle and photon emission shows that stellar activity also includes episodes with transient acceleration of particles. During solar flares, positron annihilation γ-rays had been discovered, with the characteristic 511 keV line (Chupp 1971). This is observational proof of radioactive isotopes being created by energetic particle interactions in the upper stellar atmosphere. This results from spallation reactions that produce intermediate-mass isotopes from Fe, as well as light-isotope nuclear reactions from protons and He isotopes, where the Coulomb barrier for nuclear reactions can be overcome, and from (secondary) neutron reactions.

The resulting radioactive species that are expected are listed in Table 3.5. Many nuclear lines occur during the *prompt* phase of flares as a result of nuclear excitation, as flare-accelerated nucleons collide with nuclei in the upper atmosphere.

Table 3.5 Radioactivities in solar flares, sorted by ascending radioactive mean lifetime in hours (from Table 1 in Tatischeff et al. 2006)

Isotope	Lifetime [h]	β^+	Isotope	Lifetime [h]	β^+
^{13}N	0.24	*	^{43}Sc	5.61	*
^{11}C	0.49	*	^{44}Sc	5.73	*
^{52}Mn	0.51	*	^{52}Fe	11.94	*
^{60}Cu	0.57	*	^{58}Co	13.04	–
^{34}Cl	0.77	*	^{24}Na	21.58	–
^{47}V	0.78	*	^{55}Co	25.29	*
^{63}Zn	0.93	*	^{55}Co	25.29	*
^{49}Cr	1.02	*	^{57}Ni	51.36	*
^{51}Mn	1.11	*	^{52}Mn	193.59	*
^{18}F	2.64	*	^{48}V	553.08	*
^{56}Mn	3.72	–	^{7}Be	1842.73	–
^{45}Ti	4.44	*	^{58}Co	2453.50	*
^{61}Cu	4.81	*	^{56}Co	2674.17	*

The last column identifies the isotopes contributing to the gamma-ray emission from positron annihilation with the characteristic line at 511 keV

Characteristic nuclear and positron annihilation emission from radioactive species would be delayed, and therefore recognised to be present after the prompt flaring phase, although many of these characteristic lines occur both prompt and from radioactivities (Dennis et al. 2007). Measuring the radioactive production, a study of the mixing of different isotopes in the outer stellar envelope thus could be inferred from characteristic γ-ray lines (Ramaty et al. 1995; Murphy and Share 2005; Murphy et al. 2005; Tatischeff et al. 2006). The particle acceleration arises from reconnection events in the magnetic field higher up in the solar corona (see review by Aschwanden 2008). The radioactive emission thus also directly relates to the energy content of the solar flare itself (Kozlovsky et al. 2002).

3.3 Evolution After the Main Sequence: The First Giant Branch

In Sect. 3.3.1 we discuss the main evolutionary properties of stars once they leave the long lasting phase of central H burning described above, commonly referred to as the Main Sequence, and enter the phase known as the First, or Red, Giant Branch (RGB). At the end of central H burning a star is composed of a H-exhausted core made primarily of He and a H-rich envelope. Hydrogen burning shifts from the center to the base of the H-rich mantle while the envelope expands causing the surface of the star to reach radii 10–1000 times the solar radius and to cool down to a few thousand K. This expansion triggers the formation of large scale convective motion extending from the surface down to deep regions in the star where partial H burning occurred during the Main Sequence. Some products of this H burning are

thus brought to the surface in a process known as the 1st dredge-up. In this phase the He core grows in mass because the H-burning shell continuously converts H-rich matter into He-rich matter and deposits the ashes onto the He core. The temporal evolution of the He core depends on its initial size, i.e., the size it had just after the central H exhaustion, which is in turn mostly determined by the initial stellar mass. If the mass of the He core is less than $\simeq 0.35\,M_\odot$, which occurs for initial stellar masses less than $\sim 2\,M_\odot$, an *electron degenerate core* forms where matter reaches such extraordinarily high density, up to $\simeq 10^6$ g/cm^3, that the dominant contribution to its pressure arises from the Pauli exclusion principle, which prevents the electrons from occupying identical quantum states. This leads to an increase of the lifetime of this phase up to about 100 Myr, and forces the subsequent He ignition to occur quite far from the center. If the He core is instead more massive than $0.35\,M_\odot$, the electrons remain far from the degeneracy regime.

In Sect. 3.3.2 we discuss the conditions under which ^{7}Li, the stable daughter of radioactive ^{7}Be, may be produced, preserved, and brought to the stellar surface. This nucleus is typically destroyed in the PP chain (Table 3.1), because its destruction rate is efficient at temperatures lower than its production rate. A way to produce ^{7}Li was proposed in 1971 by Cameron and Fowler (1971): if freshly synthesized ^{7}Li is quickly brought to very low temperatures by mixing, then it can be preserved. If H burning occurs in a convective environment it is in principle possible to find a high Li abundance on the surface of a star, as observed in some stars belonging to the First Giant Branch. However, these observations are in fact difficult to explain because H burning occurs in a formally stable region well below the base of their convective envelopes. Additional mechanisms of mixing must be invoked to bring ^{7}Li-rich material into the convective envelope.

3.3.1 The First Giant Branch

During the Main Sequence phase of stellar evolution described in the previous section conversion of H into He via H burning in the centre of the star leads to a progressive increase of the mean molecular weight combined with a decrease of the amount of available fuel. The net result is a slight increase of the luminosity (because L scales with the fourth power of the molecular weight, Eq. (3.10) in Sect. 3.2.1), and a mild expansion of the surface of the star because of the formation of a molecular weight gradient (Stancliffe et al. 2009). Once H is exhausted in the central region of the star, the H-exhausted core, or He core, begins to contract on a gravitational timescale while the region of active nuclear burning smoothly shifts above the He core, where H is still abundant. Further evolution of the He core depends on its mass, which, in turn, depends on the initial total mass of the star. If the He-core is more massive than a threshold value of $\sim 0.35\,M_\odot$, which happens for an initial total mass of $\sim 2\,M_\odot$, its contraction induces strong heating of the He core itself, which quickly reaches a temperature of ~ 100 MK at which fusion reaction of α particles (He burning) is activated. If, instead, the core is less massive

than $0.35\,M_{\odot}$ the high densities reached render the electron gas degenerate, hence supporting the structure against gravity without the need for additional contraction.

This difference has a large impact on further evolution of the star because, in the latter case, the He core tends towards an almost isothermal configuration due to the large mean free path of degenerate electrons relative to that of photons. If the structure was isolated, as in the case of white dwarves, it would progressively cool down losing its stored energy through the surface. Instead, in the case discussed here, the degenerate structure heats up because it is surrounded by the H-burning shell, which continuously deposits freshly synthesized He onto the He core. The rate at which the maximum temperature increases with time in the degenerate He core is controlled by the growth rate of the He-core mass, which obviously coincides with the rate at which the H-burning shell converts H into He. Strong neutrino production (Itoh et al. 1989) in the center of the electron degenerate core, due to the interaction of photons with the plasma and/or to the scattering of photons on electrons, carries away energy from the core pushing the location of the maximum temperature outward in mass. The off-center location of the maximum temperature is the result of the balance between energy loss due to the neutrino emission, which scales directly with the density and pushes the maximum temperature outward, and the energy gain due to the compressional heating, which scales inversely with the density and pushes the temperature maximum back towards the center. The key stellar parameters that control the location of the maximum temperature are the CNO abundance and the initial mass of the star. The higher the CNO abundance, the faster the conversion of protons into α particles in the H-burning shell, the stronger the heating of the degenerate He core, and the closer the maximum temperature is to the center. The higher the initial mass of the star, the lower is the degree of electron degeneracy and the density in the He core, and hence the efficiency of neutrino production.

While the H-burning shell influences the evolution of the He core, the growth of the He core influences the evolution of the H-burning shell as well. In fact, the progressive heating of the core raises the temperature at the surface of the core, where H burning occurs. This results in a continuous positive feedback: the H burning shell deposits He onto the He core, which therefore heats up. Such a heating leads to an increase of the temperature and density in the H-burning shell, accelerating the H burning rate and increasing the conversion rate of H into He, and therefore the heating of the He core. As a consequence, the progressive increase of the H burning rate determined by the growth of the He core mass, forces the H rich mantle of the star to expand and to cool. The cooling of the stellar envelope triggers a large increase of the opacity because matter enters the partial ionization regime. The temperature gradient steepens, favoring the growth of convective instabilities that very quickly extend over a major part of the H-rich mantle from the surface down to near the outer border of the H-burning shell. A consequence of the growth of these convective motions within most of the H rich mantle is a large increase of the surface luminosity caused by the continuous increase of the H burning rate coupled to the fact that the convective envelope does not absorb or release energy but just transporting it outward.

Since convective motions play a fundamental role in the physical and chemical evolution of any star, we briefly sketch the basic physical reason that leads to the growth of these large scale motions. The equilibrium condition provided by counterbalancing pressure gradients and gravity in stars does not necessarily imply stationary matter: a bubble of stellar matter may be considered stable against motion if a restoring force pushes it back towards its rest position when, for any reason, it is slightly displaced from its equilibrium location. Such a restoring force is simply given by Archimede's force, i.e., it depends on the density contrast between that of the environment and that of the bubble. If the density of an element of matter displaced towards a lower/higher density region turns out to be even lower/higher than that of its new surroundings, the element will continue to *raise*/*sink* and move away from its rest position, otherwise it will move back towards its equilibrium location.

Changes in the physical structure of the bubble during its motion play an important role in determining its density and thus its behavior. Mechanical equilibrium with the environment is certainly well verified so that it can be safely assumed that the internal pressure within the bubble instantaneously readjusts to that of the environment. More difficult is to determine the amount of heat that the bubble can exchange with the environment while moving. In the simplest case in which the bubble does not exchange any heat with the surroundings until it has covered a certain distance (adiabatic approximation), and assuming that the region is chemically homogeneous, the critical condition for the onset of large scale motions of the matter is that the temperature gradient of the environment must exceed the adiabatic gradient (Schwarzschild criterion). While the radiative temperature gradient remains less than the adiabatic temperature gradient, an element of matter will remain more/less dense than its surroundings if displaced towards less/more dense regions (within stars these displacements are typically connected to movements outward/inward in mass), and hence it will experience a restoring force that will keep it anchored to its rest location. On the contrary, when the radiative temperature gradient exceeds the adiabatic temperature gradient stochastic motion of the matter is not hampered by a restoring force, but it is amplified leading to the growth of large scale motions. Hence, convective regions are associated with steep temperature gradients, which typically occur either close to regions where energy production is strongly concentrated, or in regions where the mean free path of the photons, which scales with the inverse of the opacity, becomes so small that radiation energy transport becomes inefficient.

The determination of the temperature gradient in convective regions is quite complex: here it suffices to say that while in the interior of a star the temperature gradient in a convective region remains very close to the adiabatic gradient, in a convective envelope the temperature gradient becomes much steeper (intermediate between the radiative and adiabatic case) because the low density in the outer envelope makes energy transport by convective eddies inefficient, so that both photons and eddies contribute to the outwards transport of thermal energy.

Since convective eddies have a very large mean free path with respect to that of photons, convection is a very efficient energy transport mechanism. In the specific

case of extended convective motions that form above the H-burning shell in Red Giant stars, energy transport is so efficient that virtually all the energy produced by the burning shell is transmitted to the surface without essentially any absorption by the convective layers. It follows that a star in the H-burning shell evolutionary phase is forced to increase in size to be able to get rid of the extra energy influx, while the drop of the surface temperature is limited by the presence of a maximum temperature gradient: the adiabatic temperature gradient, which cannot be overcome by much in the largest fraction of the envelope mass.

The mere existence of stars in the RGB phase constitutes evidence of (a) the presence of an active H-burning shell, demonstrated by the breaking of the mass-luminosity relation $L \propto M^3$ that holds during the Main Sequence phase, (b) the presence of a maximum temperature gradient, demonstrated by the only minor change of the surface temperature along the RGB, (c) the continuous increase of the energy production by the H-shell burning, demonstrated by the continuous increase of the surface luminosity, and (d) the presence of an electron degenerate core (for stars with initial mass less than $\simeq 2\,M_\odot$), demonstrated by the existence of a relatively long lasting, $\sim 10^8$ years, and thus observable RGB phase, which would be prevented if the He core was gravitationally contracting.

Soon after the formation of the H burning shell, the large scale motions that grow in the H-rich envelope and rapidly extend from the surface down to just above the top of the H-burning shell, bring to the stellar surface matter partially processed by proton-capture reactions during the Main Sequence phase. This mixing, referred to as the 1st dredge-up, modifies the stellar surface composition. The amplitude of these modifications depends on the initial stellar mass and metallicity, the general rule being that the amplitude of the changes of the surface composition scales with the initial stellar mass, directly up to $3\,M_\odot$ and then inversely for higher masses, and inversely with the metallicity. Figure 3.2 shows the abundance profiles of several nuclear species as a function of the mass location for a solar-like stellar model evolved to the RGB, just before the convective envelope deeply penetrates into the star. The solid vertical line shows the maximum inward penetration of the convective envelope. Since the convective motions reach layers in which the local chemical composition has previously been modified by nuclear burning, also the surface chemical composition is modified by the mixing induced by these large scale motions. In particular the surface He abundance is slightly increased by 0.02 dex, ^{3}He increases by one order of magnitude, ^{7}Li is destroyed, the $^{12}C/\,^{13}C$ ratio drops from the solar value of 89 to roughly 30, the $^{14}N/\,^{15}N$ ratio increases from the solar value of 272 to 500 while the oxygen isotopic ratios and those of heavier nuclei remain at their solar values. A detailed quantitative determination of these changes depends on the specific stellar model considered.

The evolution of the star after the 1st dredge-up is characterized by the H-burning shell progressively converting H from the convective envelope into He, which is deposited onto the inert He core. The continuous mass transfer from the envelope to the core progressively reduces the mass of the envelope while its chemical composition does not change any more because the temperature within the convective envelope is too low to activate nuclear reactions.

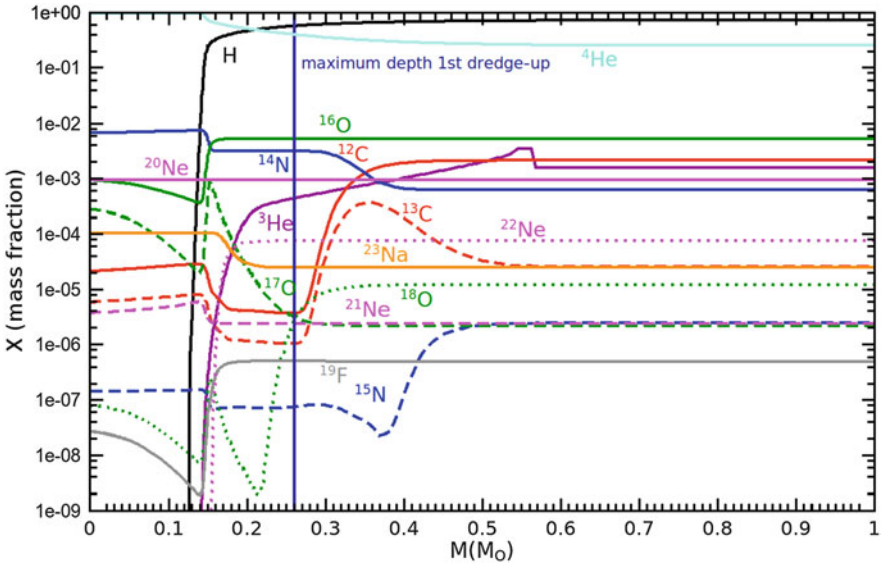

Fig. 3.2 Snapshot of the abundances of several nuclear species in a solar-like stellar model just before the onset of the 1st dredge-up. The maximum inward penetration of the convective envelope during the 1st dredge-up is marked by the vertical solid blue line

The evolution along the RGB ends when the maximum temperature in the core is high enough, $\simeq$100 MK, to activate the burning of He via 3α reactions, during which three α particles join into a ^{12}C nucleus. If the pressure is dominated by degenerate electrons the energy released by these reactions cannot be immediately balanced by an expansion of the core. Hence, He ignition occurs through a series of *flashes*, which progressively remove the degeneracy, shifting the burning towards the center. Once the electron degeneracy is fully removed, a quiescent central He-burning phase settles in.

All along the complex, and partly still mysterious, RGB evolutionary phase that links central H to central He burning, radioactive nuclei are produced by H-shell burning mainly via the CNO cycle. Most of them, however, have negligible life-times, so they could only be detected through the neutrinos they emit. Unfortunately, no Red Giant star is close enough to the Earth to allow the detection of neutrinos of nuclear origin produced in its interior. However, there are two unstable nuclei, ^{7}Be and ^{13}N, whose half life may be comparable or even larger than some stellar timescales: for ^{7}Be the half life is comparable to the envelope mixing turnover time, for ^{13}N the half life is comparable to proton-capture timescale in extremely metal-poor stars, because stars of lower metallicity are more compact and hotter, due to their lower opacity.

In the next section we discuss specifically the abundance of ^{7}Li, the stable daughter of ^{7}Be, in giant stars, which could provide important clues about the presence of additional motions extending below the base of the convective envelope.

This is important because, as we described above, the modeling of large scale motions within stars is still crude and their growth, timescale, and efficiency not yet well understood.

3.3.2 The Production of Li

Lithium (Li) isotopes[3] in stars are fragile as they are easily destroyed by proton-capture reactions once the temperature exceeds 3 MK. The destruction timescale drops from 100 Myr at 3 MK to only 0.3 Myr at 5 MK while their production through fusion reactions only occurs at much higher temperatures, between 10 MK and 25 MK. The lower limit is due to the fact that the synthesis of ^{7}Li is initiated by the ^{3}He(α,γ)^{7}Be reaction, which becomes efficient only at temperature of the order of 10 MK, while the upper value is due to activation of the ^{7}Be(p,γ)^{8}B reaction, which overcomes the electron capture reaction ^{7}Be(e^{-}, ν)^{7}Li above a temperature of the order of 25 MK. Hence, Li is efficiently produced in a temperature range where it is also efficiently destroyed and therefore there seems to be no room for Li production in a star. However, there are a number of Red Giant stars observed to be Li rich (Castilho et al. 2000; Balachandran 2005; Uttenthaler et al. 2007).

A possible way out of such a puzzling situation was recognized by Cameron and Fowler (1971) and is based on the idea that instabilities, such as convection, rotation-induced instabilities, thermohaline mixing, etc., may bring freshly made ^{7}Be from its production site to more external regions, where the temperature is low enough to inhibit proton captures on ^{7}Li, on a timescale shorter than that of electron capture of ^{7}Be. Note that the electron capture rate of ^{7}Be shows a mild increase as the temperature decreases.

A typical environment in which the Cameron-Fowler mechanism operates is during the Asymptotic Giant Phase (AGB) phase (Sect. 3.4.1), if the star is more massive than 4:5 $M_{\odot}$. These stars develop large scale motions in the H-rich mantle that extend from the surface down to regions where the temperature is high enough (>40 MK) for some nuclear burning to occur (Hot Bottom Burning), in particular via the ^{3}He(α,γ)^{7}Be reaction. Figure 3.3 shows the cumulative turnover time from the base of the convective envelope to the region of temperature T given in the abscissa for a 6 $M_{\odot}$ star of solar metallicity sometimes after the beginning of the AGB phase. The horizontal dashed grey line marks the typical timescale of the ^{7}Be(e^{-}, ν)^{7}Li reaction while the vertical dotted grey line shows the threshold temperature below which the timescale of the proton capture on ^{7}Li becomes larger than 300 Myr. In this environment ^{7}Be produced above 10 MK is successfully transferred before decaying to a region where its daughter ^{7}Li can survive.

[3]Lithium has two stable isotopes ^{6}Li and ^{7}Li, of which ^{7}Li is the more abundant representing 92% of solar Li.

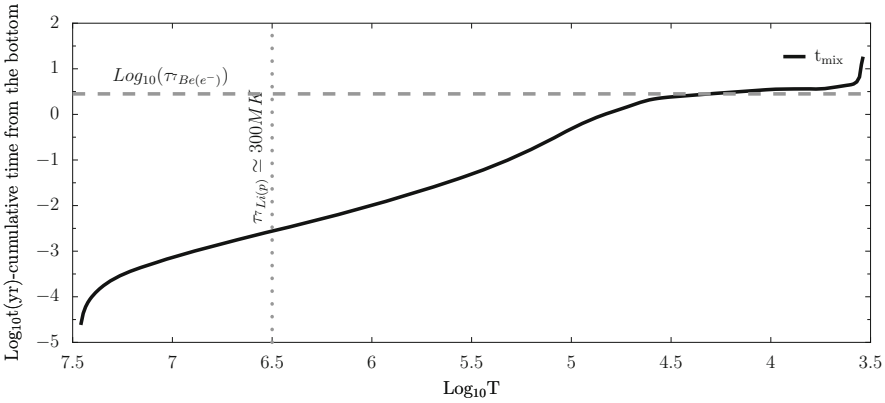

Fig. 3.3 The cumulative turnover time of the convective eddies computed from the base of the convective envelope up to the surface as a function of temperature, T. The star is a $6\,M_{\odot}$ star of solar metallicity some time after the beginning of the AGB phase. The horizontal dashed grey line marks the typical timescale of the ^{7}Be(e^{-}, ν)^{7}Li reaction while the vertical dotted grey line shows the threshold temperature below which the timescale of the proton capture on ^{7}Li becomes larger than 300 Myr

An increase of the Li abundance at the surface of RGB stars is more difficult to achieve. Though the turnover time scale within the convective envelope is also in this case rather short ($\simeq$1 year at $\mathrm{Log_{10}(L/L_{\odot})} \simeq 2$), the temperature at the base of the convective envelope always remains well below 5 MK, too low to lead to an appreciable production of ^{7}Be. Nonetheless, observations show the existence of a small number of Li-rich RGB stars (Castilho et al. 2000; Balachandran 2005; Uttenthaler et al. 2007). Figure 3.4 shows the internal structure of the region around the H-burning shell from a solar-like stellar model on the RGB. Here, ^{7}Be is synthesized well below the region where large scale motions of the matter and hence mixing of the chemical composition occur. In this environment the Cameron-Fowler mechanism could operate only by assuming the presence of presently unidentified instabilities able to drive some mixing between the region rich in ^{7}Be and the base of the convective envelope. The main constraint on this *extra* mixing is that it must get close enough to the active H-burning shell to reach the layers where the ^{7}Be production occur, but it must not enter the region of the main nuclear burning. The reason is that the speed at which a star climbs along the RGB is regulated by the speed at which H is converted into He (see above) which, in turn, also depends on the amount of fuel that continuously enters the burning region. If this extra mixing reached the active burning region, it would inevitably bring fresh H into the burning region, therefore altering the rate at which H is consumed by the H-burning shell and hence the timescale of evolution along the RGB. This evolutionary timescale is observationally well established from counting the number of stars on the RGB in many Galactic globular clusters, and already very well reproduced by current models of these stars without extra mixing.

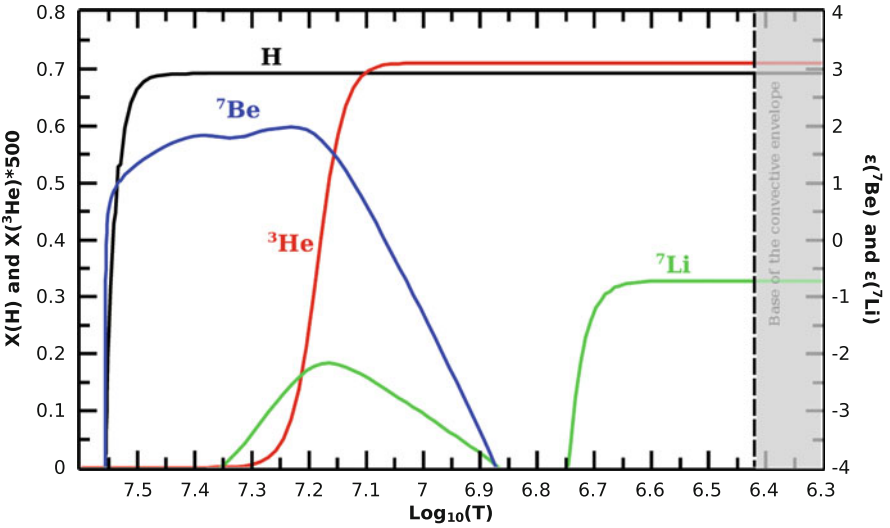

Fig. 3.4 Abundance profiles for H, ^{3}He, ^{7}Be, and ^{7}Li as function of the internal temperature in the region between the H-burning shell and the base of the convective envelope (grey area) for a solar-like stellar model on the RGB. The abundances of both ^{7}Be and ^{7}Li are given in the widely adopted logarithmic scale in which $\epsilon(X) = \mathrm{Log}_{10}(N_X/N_H) + 12$, where N_X and N_H represent the abundances of element X and of hydrogen by number. In this scale the hydrogen abundance is equal to 12

There are other hints that point towards the presence of extra-mixing phenomena in RGB stars (and perhaps in AGB stars too, as discussed in Sects. 3.6.1 and 3.6.2). The observed surface ^{12}C/^{13}C ratio and N abundance are, respectively, too low and too high with respect to the values predicted by the 1st dredge-up. Extra mixing would naturally lower the first ratio and raise the N abundance, this being the signature of H burning. A deeper mixing than predicted by current models would also reduce the abundance of ^{3}He in the stellar envelope, which is increased by the 1st dredge-up, by bringing this nucleus down to regions where it is destroyed. This reduction is needed to avoid an increase of the ^{3}He abundance in the interstellar medium, which is not observed, due to the material expelled by low-mass stars over the lifetime of the Galaxy.

Figures 3.5 and 3.6 show the isotopic abundances of several nuclei up to Al within a solar-like star while climbing the RGB (at $\mathrm{Log}(L/L_\odot) \simeq 3$). Note that we chose to use the temperature as the abscissa instead of mass to better clarify the temperature at which each nuclear species varies. The figures clearly shows that, for each given depth reached by an extra mixing process, a few nuclei are expected to be modified. For example, a drop of the oxygen abundance at the surface of an RGB star due to an extra mixing process (the depth reached by the extra mixing should extend down to at least 40 MK in this case), would also imply an increase of the surface abundances of both N and Na. Isotopes like ^{18}O and ^{22}Ne are expected to be fully destroyed, while the ^{12}C/^{13}C ratio should drop and the ^{14}N/^{15}N increase.

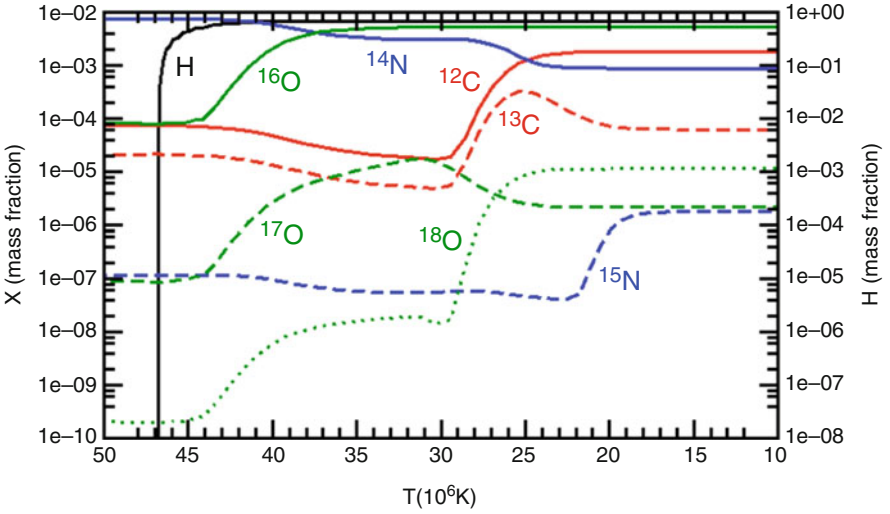

Fig. 3.5 Abundance profiles of the CNO isotopes as function of the temperature on the RGB in a solar-like stellar model

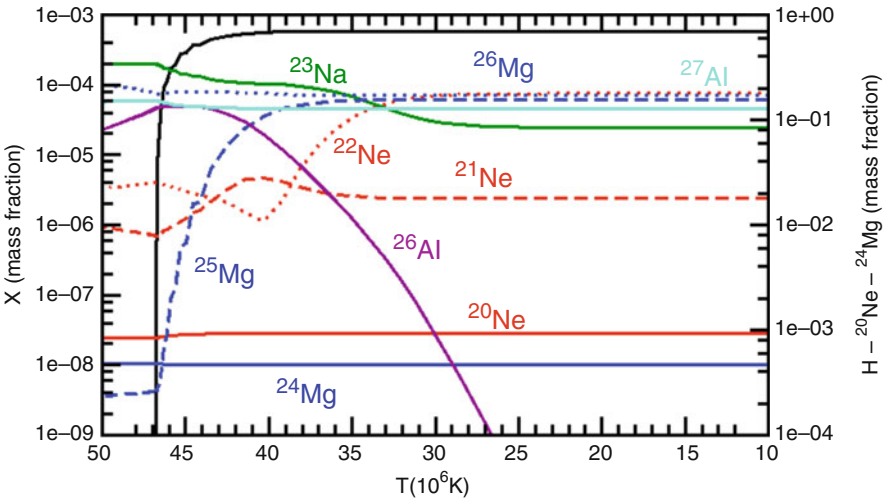

Fig. 3.6 Abundance profiles of the Ne, Na, Mg and Al isotopes as function of the temperature on the RGB in a solar-like stellar model

Note that in any case it would be very difficult to obtain a surface change of the Ne and the Mg abundances because their most abundant isotopes, ^{20}Ne and ^{24}Mg, are not modified unless the mixing reaches down to the location of main H burning.

In summary, our modeling of mixing in stars is still oversimplified and unrealistic as it is based on a simple buoyancy model. Observational evidence of stellar

abundances also involving radioactive nuclei and their daughters points out that mixing of matter outside the standard convective boundaries should occur in stars. These observations can be used to improve our description of mixing phenomena in stars.

3.4 Evolution in the Double Shell Burning Phase

We start Sect. 3.4.1 by describing the central He-burning phase and the direct scaling of the mass of the convective core resulting from He burning with the mass of the He core. The mass of the convective core determines the size of the initial He-exhausted core, an important parameter for subsequent evolutionary phases. As it happens previously when H burning shifts from the centre to a shell, also when He is exhausted in the core and He burning shifts from the centre to a shell, the envelope is forced to expand and convective motions extend from the external layers deeply inward into the star. In stars more massive than 4:5 $M_{\odot}$ the convective envelope even penetrates within the He core reducing its mass size and carrying to the stellar surface material processed by nuclear reactions (2nd dredge-up). If the He-exhausted core does not grow above $\sim$1.1 $M_{\odot}$, an electron degenerate core forms again, this time made of C and O, on top of which are located two burning shells: the He-burning and the H-burning shells. This marks the beginning of the double burning shell phase: the Thermally Pulsing Asymptotic Giant Branch (TP-AGB) phase.

The two key features of this phase are that (1) the two burning shells can not be simultaneously active, but they alternate within a cycle in producing the required energy and (2) He ignition within each cycle occurs through thermal runaway (or thermal pulse, TP) that ends when enough energy is injected in the He-burning zone to convert its temperature and density profiles into a configuration that allows stable burning. The frequency of these thermal instabilities scales directly with the He-core mass. Such an abrupt injection of a quite large amount of energy ($\sim 10^{48}$ erg) induces first the growth of a convective shell within the zone between the two shells (intershell) and second, soon after this convective region is extinguished, an expansion of the base of the H-rich envelope forces the convective envelope to penetrate well within the intershell zone (3rd dredge-up). The combination of these two successive convective episodes allows nuclei freshly synthetized by He burning to be carried up to the stellar surface. Moreover, the temperature at the base of the convective envelope scales directly with the He-core mass, and, in stars more massive that 4–5 $M_{\odot}$, reaches high enough values that H burning activates (Hot Bottom Burning, HBB).

In Sect. 3.4.2 we discuss Super-AGB stars, i.e., stars with initial mass in the interval between stars that develop an electron degenerate core after He is exhausted in the center and enter the AGB regime, and more massive stars that do not develop an electron degenerate core. Super-AGB stars ignite carbon out of center in semidegenerate conditions and go through a central C-burning phase. However, the

C-exhausted core is not massive enough to heat up to the Ne burning, so an electron degenerate ONeMg core forms. These stars then go through a thermally pulsing phase. The final fate of these stars depends on the capability of their ONeMg core to reach the critical mass of $\sim 1.35\,M_{\odot}$ required to activate electron captures on ^{24}Mg and ^{20}Ne. Stars with a core that does not reach this critical mass lose all their H-rich envelope and end their life as ONeMg white dwarves, while stars with a core that reaches this critical mass explode as *electron capture supernovae*.

We continue by briefly discussing mass loss during the AGB phase in Sect. 3.4.3. The strong increase in surface luminosity, coupled to luminosity variations and formation of dust grains in the atmospheres of AGB stars, strongly enhances the mass-loss rate in this phase with the consequence that all AGB stars lose their H-rich envelope, leaving behind the naked electron degenerate core as a cooling CO white dwarf. Finally, in Sect. 3.4.4, we discuss the different species of dust grains that form in the atmosphere of an AGB star. The key role here is played by the C/O number ratio in the atmosphere because the strong bond of the CO molecule results in trapping all of the atoms of the least abundant of the two elements. In an oxygen-rich gas (O>C) the species of dust are, for example, Al_3O_2 (corundum) and many different types of silicates (SiO, SiO_2, etc). In a carbon-rich gas (C>O), the species of dust are, for example, SiC (silicon carbide) and C itself (graphite). Some of this stellar AGB dust is now recovered from primitive meteorites, representing a real speck of an ancient AGB star under our control in the laboratory.

3.4.1 Asymptotic Giant Branch (AGB) Stars

As anticipated at the end of Sect. 3.3.1, once the central temperature in a RGB star exceeds 100 MK, He in the core starts being converted into ^{12}C via 3α reactions, and subsequently into ^{16}O via $^{12}C(\alpha, \gamma)\,^{16}O$ reactions. The cross section of the 3α reaction has a tremendous dependence on the temperature: it scales roughly as T^{23} in the range 100–300 MK, so that the energy produced by these reactions is very strongly concentrated towards the centre of the star where the temperature is at its maximum. The very large photon flux that forms in these conditions triggers the formation of large scale motions of the matter, which turn the material in the central part of the star (the convective core) in order to efficiently carry the energy outward. The mass of the convective core depends on the luminosity produced by the 3α reactions. This luminosity scales with the mass of the He core because the larger its mass, the larger is the amount of energy required to maintain the hydrostatic equilibrium (see Sect. 3.2). Hence, the size of the convective core scales directly with the mass of the He core. The mass of the He core, in turn, scales directly with the initial mass of the star, thus, in conclusion, the mass of the convective core scales directly with the initial mass of the star. Analogously to the Main Sequence central H-burning phase, the energy production in the core is dictated by the mass of the star (see Sect. 3.2.1). However, the role played by the total stellar mass in central H burning is in the central He-burning phase replaced by the He-core mass because

the density contrast between the He core and the H-rich mantle is so large that the core does not feel the presence of the H rich mantle and evolves as if it was a naked He core.

In the meantime, the temperature at the He/H interface is high enough that also an efficient H-burning shell is active leading to continuous deposition of fresh He onto the He core. Moreover, large convective motions develop (in most cases) in the outer H-rich envelope. The actual extension and temporal variation of these convective regions depends on the initial mass and chemical composition of the star.

At variance with H burning, no radioactive nuclei are produced by the 3α and the $^{12}C(\alpha, \gamma)\ ^{16}O$ reactions because they convert matter along the valley of β stability. Radioactivity during He burning is produced instead via the sequence of reactions that convert ^{14}N into ^{22}Ne via a double α capture and the radioactive decay of ^{18}F: $^{14}N(\alpha, \gamma)\ ^{18}Fe^{+} + \nu)\ ^{18}O(\alpha, \gamma)\ ^{22}Ne$. In H-exhausted regions, ^{14}N is by far the most abundant nuclear species after He because a main effect of the CNO cycle, which operated in the previous H-burning phase (see Sect. 3.2.1) is to convert most of the initial C and O, the two most abundant elements beyond H and He, into N. Hence, during He burning ^{22}Ne becomes the most abundant isotope, after C and O, once ^{14}N is fully consumed by α captures.

When He is exhausted in the centre, He burning moves smoothly outward in mass leaving behind a CO core that begins to contract on a dynamic timescale. Similar to the H-burning shell, also the He-burning shell produces more energy than required to balance gravity because energy production is controlled by the size of the underlying core, and not by the mass of the star. The CO core increases progressively in mass because of the continuous deposition of CO-rich material made in the He-burning shell, the He-burning shell increases its energy production accordingly. As a consequence, the overlying He+H-rich mantle is forced to expand substantially and to cool down so much that the H-burning shell switches off. As during the RGB phase, this expansion progressively inhibits energy transport by radiation and large scale motions of the matter progressively extend inward from the outer envelope. In stars initially more massive than 4–5 $M_{\odot}$ the convective envelope penetrates even inside the He core (2nd dredge-up). The main consequences of this are a change of the surface abundances and a reduction of the He-core mass. Similar to what happens during the RGB, the formation of an extended convective envelope forces the stars to expand at roughly constant surface temperature because the onset of convective motions fixes a maximum value for the temperature gradient (see Sect. 3.2.1) and increasing luminosity. This phase is called Asymptotic Giant Branch (AGB). The specific phase when the He-burning shell advances in mass eroding the He core from inside is called Early Asymptotic Giant Branch (E-AGB).

The competition between the advancing He-burning shell and the sinking of the convective envelope during the 2nd dredge-up fixes the maximum mass that the CO core (M_{CO}) reaches in this phase. If M_{CO} is larger than roughly 1.1 $M_{\odot}$, the core heats up to the C ignition temperature ($\sim 8 \times 10^8$ K), otherwise it turns into an electron degenerate CO core able to self-sustain against gravity without the need of additional contraction. The maximum initial stellar mass for which an electron degenerate CO core forms is of the order of 7–8 $M_{\odot}$, for solar metallicity

stars. While the evolution of stars without an electron degenerate core is dictated by the self gravity of the core, the evolution of stars with an electron degenerate core is controlled by the burning shells. In the following we concentrate on the further evolution of the latter case, i.e., the AGB, while Chap. 4 describes the further evolution of the first case.

On the AGB three main regions may be identified: the electron degenerate CO core, a He-rich layer (also referred to as *intershell* since it is located between the He- and the H-burning shells), and a H-rich mantle, most of which forms an extended convective envelope. As the He-burning shell approaches the border of the He core, it quenches because of the steep temperature drop associated with the drastic reduction of the mean molecular weight caused by the change from a He-dominated to a H-dominated chemical composition. Being less and less supported by the extinguishing He burning shell, the mantle is forced to shrink, heat up, and progressively re-activate the H-burning shell at its base. The H-burning shell starts to deposit fresh He onto the He shell forcing the intershell to heat up again. At this point a fascinating evolutionary phase begins in which nuclear burning and instabilities coexist, realizing a unique *habitat* in which a large number of nuclear species may be synthesized: the Thermally Pulsing AGB (TP-AGB) phase.

Quite schematically, the TP-AGB phase consists of a sequence of cycles each of which may be divided in two main phases: a quiescent H-burning phase during which the He-burning shell is inactive, and a He-burning phase during which the H-burning shell is inactive. Though the two shells do not operate simultaneously, they process roughly the same amount of mass per cycle so that the intershell mass changes slowly in time. The transition from the active He-burning phase to the active H-burning phase occurs quiescently in the sense that the energy provided by the H-burning shell progressively replaces that provided by the dimming He-burning shell. Instead, the transition from the active H-burning phase to the active He-burning phase occurs in a traumatic way, which is responsible for the peculiar sequence of events that characterizes the TP-AGB phase.

The reason for such a traumatic He ignition is that the pileup of fresh He on top of an inert intershell leads to a T, ρ profile in the intershell that is controlled by the compressional heating caused by the accretion of fresh He. This T, ρ profile is quite different from the typical one determined by the presence of an active burning shell. The large amount of energy required to turn the T, ρ profile from that determined by the accretion and that required by the steady He burning, coupled to the very steep dependence of the cross section of the 3α nuclear reaction on the temperature, determines the growth of a thermal runaway (or *thermal pulse*, TP) in which a huge amount of energy is released over a very short timescale. This runaway comes to an end when enough energy has been deposited in the intershell to turn the T, ρ profile into a profile suited for quiescent He burning. As an example, Fig. 3.7 shows as a gray line the typical Log(T), Log(ρ) profile produced by the advancing H-burning shell just prior to 3α ignition, while the black line shows the typical profile at the end of the thermal runaway during steady He burning. In this specific example roughly $\sim 10^{48}$ erg must be deposited in the intershell to perform the transition between the two configurations. This amount of energy is determined by the fact that the needed

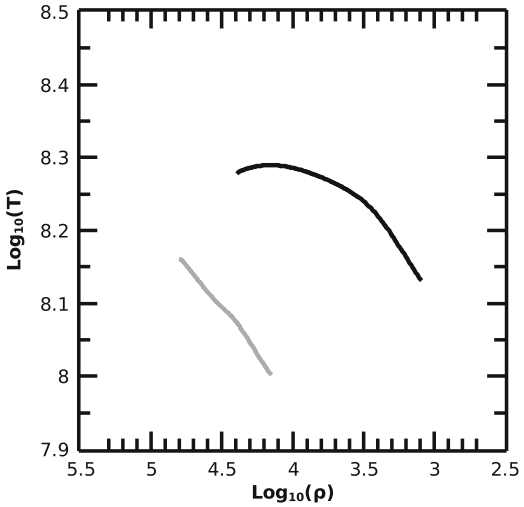

Fig. 3.7 The gray thick solid line shows the typical Log(T)-Log(ρ) profile in the intershell (in the range $10^{-3} < X_{He} < 0.9$) just prior the onset of a thermal pulse in a 3 $M_\odot$ of solar metallicity while the black thick solid line shows the typical profile in the same region at the end of the thermal runaway when the steady He burning occurs

change of the T, ρ structure in the intershell requires a reduction of the binding energy of the intershell.

The main effect of the rapid injection of energy into the intershell during the TP is the production of a very strong energy flux, which forces the growth of convective instabilities to efficiently carry the energy outward. This convective shell extends over most of the intershell region and plays a fundamental role in reshuffling the chemical composition within this region and hence influencing the detailed nucleosynthesis that occurs at this stage (see next sections). Once the TP comes to an end, the convective shell disappears and the quiescent He-burning shell phase begins. Another important side effect of the rapid energy injection caused by the TP is the expansion of the region above the He-burning shell, which forces a cooling of this region. The consequence is that the H-burning shell switches off, and the temperature gradient steepens. This favors the penetration of the convective envelope down into the intershell so that nuclei freshly synthetized in the deep interior of the star are efficiently brought up to the stellar surface (3rd dredge-up). Similar to what happens towards the end of the E-AGB phase, the He-burning shell progressively runs out of power as it approaches the border of the He-rich layer, where the temperature drops below the value necessary for the He burning. The overlying layers are forced to contract and heat so that a H-burning shell activates again and a new cycle starts.

To visually illustrate the sequence of events making up a full TP cycle and to make clear the peculiarity of the TP-AGB phase, Fig. 3.8 shows the temporal evolution of the internal structure of a typical AGB star through three consecutive TPs.

The quantitative characteristics of the TPs depend on the core and envelope masses, the general rule being that larger CO core masses correspond to higher frequencies of thermal pulses, higher temperatures, and shorter lifetimes of the He

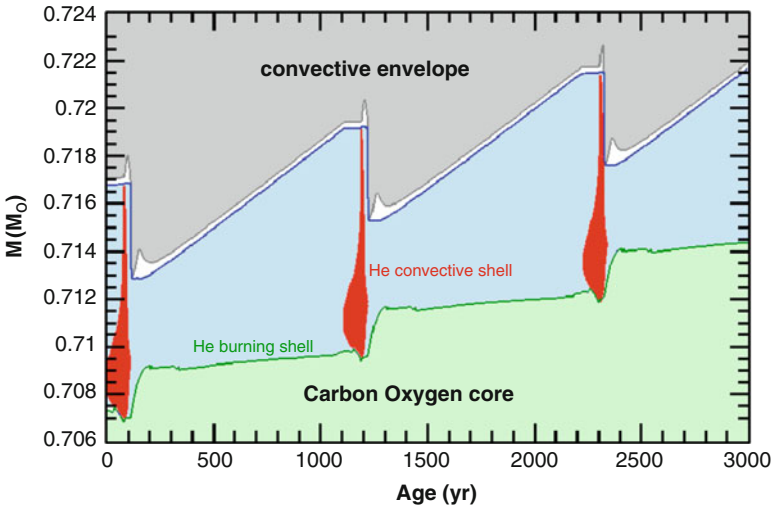

Fig. 3.8 Temporal evolution of the internal structure of a typical AGB star through three consecutive TPs. The He convective shell is shown in red while the convective envelope is grey. The H and He burning shells are shown in dark blue and dark green, respectively, while the intershell is light cyan. The timescale between the onset of the He convective shell and the maximum inward penetration of the convective envelope during the 3rd dredge-up has been increased by a factor of 100 to improve the readability of the figure

convective shell. Typical TP frequencies (determined after the first 20 TPs or so) range between 2 and 3 TPs per 10^5 years for a $3\,M_\odot$ star having $M_{CO} \sim 0.7\,M_\odot$ and more than 50 TPs per 10^5 years for a $6\,M_\odot$ star having $M_{CO} \sim 0.96\,M_\odot$, while the peak luminosity ranges between 1and10 $10^8 L_\odot$.

Since the two burning shells process about the same amount of matter per cycle, the average growth rate of the CO core per cycle roughly equates that of the He core. This, coupled to the fact that He burning produces (per unit mass) roughly 10% of the energy produced by H burning, and that the luminosity of these stars does not change appreciably between the two burning phases, allows us to estimate the relative burning lifetimes (t_{He}/t_H). The amount of energy produced by He burning per cycle must balance the surface losses, i.e., $\epsilon_{He} \times \Delta M_{He} = L_{surface} \times t_{He}$, where ϵ_{He} represents the amount of energy liberated by the He burning per unit mass, ΔM_{He} the amount of mass processed by the He burning, $L_{surface}$ the luminosity of the star and t_{He} the lifetime of the He burning phase. Similar for the H burning one may write that $\epsilon_H \times \Delta M_H = L_{surface} \times t_H$. If the amount of mass processed is similar in the two cases (i.e., $\Delta M_{He} \simeq \Delta M_H$), the relative lifetimes scale roughly as the two nuclear burning rates, i.e., $t_{He}/t_H \sim 1/10$. The amount of He burnt during each He-burning episode is only partial, corresponding to about 25–30% of the He present in the intershell. Of this, roughly 25% burns during the TP and the remainder during the quiescent He burning phase. The final nucleosynthetic result is that carbon is produced via the 3α reaction, but it is only marginally converted into oxygen. The

typical composition of the intershell after this partial He burning is represented by matter made by roughly 75% He and 23% ^{12}C, while the remaining few percent are made up of ^{22}Ne (from conversion of ^{14}N as detailed above) and of ^{16}O. The ^{22}Ne nuclei are of interest as they act as a neutron source in the TPs when the temperature reaches 300 MK. The lifetime of the He convective shell varies between 100 years and 10 years for the 3 $M_\odot$ and 6 $M_\odot$ stellar models, respectively. Typically, the He burning shell is located between 7×10^{-3} and $1.5 \times 10^{-2} R_\odot$ from the center of the star, while the H-burning shell is located between 1×10^{-2} and $2 \times 10^{-2} R_\odot$. The intershell mass ranges roughly between 10^{-3} and 10^{-2} $M_\odot$. The surface radii of AGB stars vary between hundreds to thousands times the solar radius.

The final fate of AGB stars is to lose all their H-rich mantle before the electron degenerate core may grow to its most massive stable configuration (i.e., the Chandrasekhar mass). Such a destiny is due to the strong dependence of the mass-loss rate on the luminosity of the star and on its surface chemical composition (see Sect. 3.4.3). The maximum mass size reached by the CO core, which equates the mass of the newborn white dwarf, is determined by the competition between the speed at which the burning shells advance in mass and the efficiency of the mass loss that erodes the H-rich mantle from the surface.

The occurrence of the 3rd dredge-up significantly affects the evolutionary properties of an AGB star. First, it reduces the size of the He core anticipating the quenching of the quiescent He burning phase and hence its lifetime. Second, it slows down the overall growth rate of the CO core and the He-rich shell. Third, it carries to the stellar surface a fraction of the material freshly synthesized by partial He burning, i.e., C, ^{22}Ne, and *slow*-neutron capture (*s*-process) elements heavier than iron (see Sect. 3.5), drastically modifying the chemical composition of the star. In some cases, the star even changes from the usual oxygen-rich (O>C) composition to carbon-rich (C>O), with important consequences on the types of molecules and dust that can form and the ensuing mass loss (see Sect. 3.4.4). Unfortunately, the question of the maximum depth reached by the convective envelope during the 3rd dredge-up has always been highly debated and different results have been obtained over the years by different authors for AGB stars over the whole mass interval from 1.5 $M_\odot$ up to the more massive thermally pulsing stars. The reason is that, once the convective envelope enters the He core, a discontinuity in the opacity (H is much more opaque than He) determines the formation of a positive difference between the effective and adiabatic temperature gradients just at the border of the convective envelope. This is an unstable situation because the possible mixing of matter located just below the base of the convective envelope with the H-rich convective mantle is an irreversible process in the sense that these *additional* mixed layers become intrinsically convective because of the drastic increase of the opacity due to the mixing. It is therefore clear that even small different numerical techniques adopted by different authors may lead to quite different results.

Furthermore, the occurrence of the 3rd dredge-up is important because it creates a sharp discontinuity between the convective envelope and the radiative intershell. Since a sharp discontinuity is not a realistic configuration in these conditions, the occurrence of the 3rd dredge-up allows the possibility that some kind of *diffusion* of

protons occurs below the formal border of the convective envelope when it reaches its maximum inward extension at the end of the 3rd dredge-up smoothing out the discontinuity (though this is not obtained by applying the standard stability criteria for mixing). However, the shape, extent, and timescale over which the diffusion of protons in the He/C intershell may occur is unknown, its modeling is still artificial and not based on self-consistent computations.

This diffusion allows the formation of regions where a small amount of protons come in contact with matter that is predominantly composed of He and C, so that the ratio $Y(H)/Y(C) \ll 1$, but does not contain any ^{14}N, since this nucleus has been fully converted into ^{22}Ne in the previous TP. When these proton-enriched layers begin to contract and to heat because of the quenching of the He burning, the CN cycle activates, but it can not go beyond the synthesis of ^{13}C due to the low proton concentration. As the temperature increases to roughly 90 MK, the $^{13}C(\alpha, \mathbf{n})\ ^{16}O$ reaction becomes efficient and a significant neutron flux is produced. Hence, this diffusion plays a pivotal role in the nucleosynthesis of species beyond the Fe peak via neutron captures. A detailed description of the properties of this neutron source and of its nucleosynthetic signature will be presented in Sect. 3.5.1. The lack of ^{14}N is crucial here, since this nucleus is a strong neutron poison and its presence would inhibit neutron captures by Fe and the elements heavier than Fe.

As already discussed in Sect. 3.3.2, typical temperatures at the base of the convective envelope do not exceed a few MK at most in the evolutionary phases prior to the AGB. Instead, another peculiarity of AGB stars is that during the H-burning phase the temperature at the base of the convective envelope may reach values in excess of several tens MK, and even exceed 100 MK, so that H-burning reactions activate within the convective envelope. In these conditions the coupling between burning and mixing may lead to conspicuous synthesis—and spread through the whole convective envelope up to the stellar surface—of nuclei like ^{14}N, ^{7}Li, and the long-lived radioactive nucleus ^{26}Al (discussed in detail in Sect. 3.6.1). The efficiency of this phenomenon, known as Hot Bottom Burning (HBB), scales directly with the temperature at the base of the envelope and hence with the CO-core mass, which in turn scales with the initial stellar mass. Hence, HBB is efficient in stars more massive than $4{:}5\,M_{\odot}$, depending on the metallicity. As the energy produced in the convective envelope sums to that produced by the H-burning shell, the core mass—luminosity relation changes (even strongly) in the presence of HBB. From a nucleosynthetic point of view the occurrence of an active H burning in a convective environment implies a redistribution of the processed material over all the convective zone, so the surface abundances turn towards the relative abundances typical of the H burning at high temperature. For example, an increase of the surface abundances of elements like ^{14}N and ^{26}Al, a temporaneous increase of ^{7}Li, a reduction of ^{12}C and of the $^{12}C/^{13}C$ ratio and the signature of the NeNa and the MgAl sequences.

We refer the reader to the review papers by Herwig (2005) and Karakas and Lattanzio (2014) and to the book on the evolution of AGB stars by Lattanzio and Wood (2004) for a thorough presentation of the evolution of these cool giant stars.

3.4.2 Super-AGB Stars

In the previous section we identified stars that go through the double shell burning of the TP-AGB phase as those that develop an electron degenerate CO core where carbon burning fails to occur. There is, however, another class of stars that experience the double shell burning phase: those with initial total mass between the maximum mass that forms an electron degenerate CO core where C does not ignite (M_{up}) and the minimum mass that does not form an electron degenerate CO core (M_{mas}). Stars more massive than M_{mas} evolve up to the final core collapse as described in Chap. 4. Depending on the initial chemical composition and the adopted physics, M_{up} ranges between 6–8 $M_\odot$, and M_{mas} ranges between 9–12 $M_\odot$. It is important at this point to recall that these limiting masses are somewhat uncertain because they depend on the size of the convective core, the carbon to oxygen ratio left by the He burning, the efficiency of the second dredge-up and the cross section of the ^{12}C plus ^{12}C nuclear reaction. Unfortunately, all these quantities are still subject to severe uncertainties.

Stars falling between these two limits form a partially electron degenerate core, but are massive enough to ignite C in the core, lift the degeneracy, and go through the C burning in the core. They are not massive enough, however, to avoid the electron degeneracy of the ONeMg core left by C burning. The evolution of stars in this relatively small mass interval, called Super-AGB stars, has not been studied extensively up to now because of the difficulty in computing the C-burning phase due to the complex removal of the degeneracy that occurs through a series of successive flashes, and the lack of massive computer power, which is needed to study this complex situation. This situation is rapidly changing and progress has been made on the computational modeling of Super-AGB stars (Doherty et al. 2017, see review by).

Since these stars form an electron degenerate core after core C burning, they also go through a double shell burning phase similar to the AGB phase experienced by their less massive counterparts. Because their degenerate cores are more massive, following the trend shown by AGB stars, the frequency of the thermal pulses is higher (up to 500 TP per 10^5 years), the He peak luminosity is lower than in the normal AGB stars (up to $\sim 4 \times 10^6 L_\odot$), while the base of the convective envelope may reach temperatures as high as 110 MK, hence, H burning occurs within the convective envelope (Hot Bottom Burning). Similar to what happens in the more massive AGB stars, but quantitatively more pronounced, the luminosity produced in the convective envelope adds to that produced by the radiative H burning significantly altering the core mass—luminosity relation and the surface composition is modified by the signature of H burning. The possible occurrence of the 3rd dredge-up would also shuffle the surface chemical composition with the typical products of the partial He burning, i.e. C, and *s*-process elements. The efficiency of the 3rd dredge-up is very uncertain also for these stars. In principle, one could expect a lower efficiency of the 3rd dredge-up because the amount of energy released by a TP is lower and the overall temperature is much higher than

in a standard AGB star, so that it could be more difficult to expand the base of the mantle and to steepen the temperature gradient up to a value that would allow the convective envelope to penetrate the He core. Quantitative estimates of the yields of the nuclei specifically produced by the TP Super-AGB stars are now available (Doherty et al. 2017).

The final fate of a Super-AGB star depends on the competition between the advancing burning shells, which increase the size of the ONeMg core, and the mass loss, which limits its growth. Also an efficient 3rd dredge-up would contribute to limiting the growth of the core. Stars more massive than a critical value reach the threshold electron degenerate core mass for the onset of electron captures on ^{24}Mg and ^{20}Ne after a certain number of TPs and eventually explode as *electron capture supernovae*. Stars less massive than the critical value, instead, end their life as ONeMg white dwarfs. An estimate of the electron degenerate core mass above which electron captures become efficient in an ONeMg environment can be determined by considering that the threshold energy for electron capture is 6 MeV for ^{24}Mg and 8 MeV for ^{20}Ne and that the mass of a fully electron degenerate core having a Fermi energy of the order of 6 MeV is $\simeq 1.35\,M_{\odot}$. Thus, if the electron degenerate core grows to the threshold value of $\simeq 1.35\,M_{\odot}$ or so, electron captures are activated on ^{20}Ne and ^{24}Mg.

This process removes electrons and hence pressure from the center of the star, starting a runaway process that leads to the core collapse and final explosion known as electron capture supernovae. The explosion of these electron capture supernovae is similar to that of core collapse supernovae (see Chap. 4), with a few distinct features. During the initial collapse of the degenerate core, electron captures increase significantly the degree of neutronization of the matter, i.e., raise the global neutron over proton ratio because of the capture of the electrons by the protons. The nuclear species produced by explosive burning depend significantly on the neutron over proton ratio so that the higher the degree of neutronization of the matter the higher the production of neutron-rich nuclei: in particular ^{58}Ni becomes favored with respect to ^{56}Ni. Since the luminosity peak of a supernova correlates with the amount of ^{56}Ni produced during the explosion, a natural feature of these electron captures supernovae is a lower luminosity with respect to typical core collapse supernovae. Also, the final kinetic energy of the ejecta is expected to be of the order of 0.1×10^{51} erg, roughly one order of magnitude lower than in typical core collapse supernovae (see, e.g., Hoffman et al. 2008; Wanajo et al. 2009).

3.4.3 Winds from AGB Stars

An observed peculiarity of AGB stars is that they show strong stellar winds, which carry material away from the surface of the star into its surroundings. Nuclei newly synthetized during the AGB phase and carried to the stellar surface by the 3rd dredge-up are shed into the interstellar medium so that AGB stars contribute to the chemical make-up of their environments and of new generations of stars. The

mass loss rate due to winds in AGB star increases as the star evolves along the AGB and can reach values as high as $10^{-4}\,M_{\odot}$/year (to be compared, for example, to the solar mass loss rate of $10^{-11}\,M_{\odot}$/year) at the end of the AGB, which is known as the *superwind* (Iben and Renzini 1983). This is a strong and dense but slow wind, with material leaving the star at relatively low speeds of 5–30 km/s.

The winds are caused by two main factors (see review by Höfner and Olofsson 2018). First, large quantity of dust form around AGB stars and radiation pressure acting on this dust contributes to driving the winds. The extended envelopes of red giant and AGB stars, where the temperature drops down to ∼1000 K, are an ideal location for the formation of a large variety of molecules like CO, TiO, VO, as well as ZrO, when the gas has been enriched in heavy elements such as Zr by the *s* process and the 3rd dredge-up, and C_2, CN, and CH, when the gas has been enriched in carbon by the 3rd dredge-up. In the case of refractory elements, which have the property of condensing at high temperatures directly from gas into the solid state, the gas condenses into tiny particles, which then can grow into dust grains. Because of the large quantity of dust around them, AGB stars become obscured toward the end of their life and can only be seen as mid-infrared sources, since the dust absorbs the energy of the visual light coming from the star and reemits it as infrared light. Second, AGB stars are variable stars, meaning that their luminosity varies with time with changes occurring over relatively long periods >100 days. These luminosity variations are due to stellar pulsations, in the sense that the whole star expands and contracts. Pulsations produce changes in the stellar radius and temperature, which cause the variations in the stellar luminosity. When the pulsations attain a large amplitude they lead to strong stellar winds and a large mass-loss rate. Pulsation levitates matter above the photosphere and increases the wind density by about two orders of magnitude (Wood 1979; Sedlmayr and Dominik 1995; Dorfi et al. 2001).

The strong stellar winds driven by the combined effects of radiation pressure acting on dust and pulsation eventually erode the whole stellar envelope (Dupree 1986; Willson 2000). Hence, the winds govern the lifetime of AGB stars because when the envelope is almost completely lost the star moves away from the AGB phase into the hotter post-AGB phase. Toward the end of the post-AGB phase, the shell of material ejected by the AGB star may become illuminated by the radiation coming from the central star, and produce a planetary nebula. The former AGB stars is now referred to as a *planetary nebula nucleus* and finally turns into a cooling CO white dwarf.

3.4.4 Dust from Giant Stars and the Origin of Stardust

The specific dust species that form in the atmosphere of AGB stars depends mainly on the C/O ratio. The difference in the type of dust that can form in a carbon-rich or oxygen-rich gas is due to the strong bond of the CO molecules: if O>C, all carbon atoms are locked into CO and only oxygen-rich dust can form, viceversa, if

Table 3.6 Types and populations of meteoritic stardust grains, and their inferred origins. See also Sect. 10.2

Type	Population	Origin
Oxide and silicate grains	I	AGB stars
	II	AGB stars
	III	?
	IV	Supernovae
Silicon carbide (SiC)	Mainstream	AGB stars
	Y	AGB stars
	Z	AGB stars
	X	Supernovae
	A+B	?
	Nova grains	Novae
Silicon nitride		Supernovae
Graphite	Low-density	Supernovae
	High-density	?
Diamond		?

C>O, all oxygen atoms are locked into CO and only carbon-rich dust can form.[4] In an oxygen-rich gas (O>C) dust species are, for example, Al_3O_2 (corundum), $CaAl_{12}O_{19}$ (hibonite), $MgAl_2O_4$ (spinel), as well as many different types of silicates (SiO, SiO_2, etc). In a carbon-rich gas (C>O), dust species are, for example, SiC (silicon carbide), TiC (titanium carbide), and C itself (graphite).

Formation of dust around AGB stars is well documented by spectroscopic observations in the infrared (e.g. Treffers and Cohen 1974; Speck et al. 2000, 2009) and predicted to occur by theoretical models (e.g. Fleischer et al. 1992; Lodders and Fegley 1993; Gail and Sedlmayr 1999; Ferrarotti and Gail 2002, 2006; Nanni et al. 2013; Dell'Agli et al. 2017). It is now widely accepted that AGB stars are the most prolific source of dust in the Galaxy. When summing up the contribution of the different families of late red giant and AGB stars: i.e., spectroscopically, the M stars, the OH/IR stars,[5] and the carbon stars, it results that ∼90% of all dust of stellar origin in the interstellar medium came from these sources (Whittet 2002).

Thus, it is not surprising that the vast majority of stardust grains extracted from meteorites (Chap. 2, Sects. 2.2.4 and 10.2) show the signature of an origin in AGB stars (Table 3.6). The main signatures of AGB nucleosynthesis imprinted in meteoritic stardust grains are: (1) the O isotopic composition of the majority of oxide and silicate grains showing excess in ^{17}O and deficits in ^{18}O, and known as Population I and II of stardust oxide grains (Nittler et al. 1997), which match the O isotopic ratios observed around AGB stars via spectroscopic observations of CO molecular lines (e.g. Harris et al. 1987; Hinkle et al. 2016; Abia et al. 2017), and (2) the distribution of the $^{12}C/^{13}C$ ratios of >90% of SiC grains showing a peak between

[4]This general rule is debated in the case of dust formation in supernova ejecta, see Chap. 2, Sect. 2.2.

[5]OH/IR stars are cool red giants with strong hydroxyl (OH) masers and infrared (IR) emissions.

50 and 60 (solar value is 89) and known as the *mainstream* SiC population, which match the distribution derived from spectroscopic observation of CO molecular lines in C-rich AGB stars (see Fig. 3 of Hoppe and Ott 1997). The Ne composition measured in stardust SiC grains—corresponding to the Ne-E(H) component rich in ^{22}Ne (see discussion in Chap. 2, Sect. 2.2.4) is also a clear signature of material from the intershell of AGB stars, where ^{22}Ne is abundant. Moreover, the elemental and isotopic abundances of the heavy elements Kr, Sr, Zr, Ru, Xe (the Xe-S component), Ba, Nd, Sm, W, and Pb present in trace amount and measured in SiC grains clearly show the imprint of the *s*-process, which make inevitable their connection to AGB stars. Smaller SiC Populations Y and Z ($\simeq$1% each of the total recovered stardust SiC grains) are also attributed to AGB stars, but of metallicity down to 1/3–1/5 of the solar value (Hoppe et al. 1997; Amari et al. 2001b; Zinner et al. 2006).

With regards to the remaining types and populations of stardust grains, supernovae of Type II have been invoked as the origin site of Population X of SiC grains ($\sim$1%) and the few recovered silicon nitride grains (Nittler et al. 1995), showing excesses in ^{28}Si and evidence of the early presence of ^{44}Ti, as well as low-density graphite grains and Population IV of oxide and silicate grains (with excess in ^{18}O and ^{18}Si Vollmer et al. 2008; Travaglio et al. 1999; Pignatari et al. 2013, see Chap. 4). Novae are invoked for a few SiC grains of unusual composition (excesses in ^{13}C and ^{15}N Amari et al. 2001a, see Chap. 5, Sect. 5.2), while the origin of SiC grains of Populations A+B ($\simeq$5% of all SiC grains, showing ^{13}C/^{12}C $<$10) is still unclear (Amari et al. 2001c). Oxide and silicate grains with deficits in both ^{17}O and ^{18}O, known as Population III, have been attributed to stars of metallicity lower than solar, however, the Si isotopic composition of the silicate grains belonging to this population is very close to solar, which does not support this interpretation. The origin of this population remains to be ascertained, together with the origin of high-density graphite grains and of the very abundant and extremely tiny (10^{-9} m) meteoritic diamond grains, the majority of which probably formed in the solar system. For more details in meteoritic stardust see, e.g., Clayton and Nittler (2004) and Lugaro (2005).

Given compelling evidence that most stardust came from AGB stars, the composition of these grains can be used as a stringent constraint for theoretical models of AGB stars and, viceversa, the models can be used to identify the mass and metallicity range of the parent stars of the grains. Data from the laboratory analysis of stardust are usually provided with high precision, down to a few percent errors, and for isotopic ratios. In comparison, data from spectroscopic observations of stellar atmospheres usually are provided with lower precision, errors typically $>$50%, and mostly for elemental abundances. Thus, the information from stardust grains represents a breakthrough in the study of AGB nucleosynthesis. Also, given that the abundances and isotopic compositions of elements heavier than Al and lighter than Fe, such as Si and Ti, are mostly unaltered by AGB nucleosynthesis, laboratory analysis of these elements in AGB stardust can be used to constrain in great detail the initial composition of the parent star of the grains, and in turn the chemical evolution of the Galaxy (e.g. Zinner et al. 2006).

Meteoritic stardust provides us with abundant and precise information on radioactive nuclei in stars because the initial abundance of radioactive nuclei at the time of the formation of the grains is recorded by the signature of their radioactive decay inside the grains, which is easily derived from measurements of the excesses in the abundances of their daughter nuclei. An important example is that of ^{26}Al, where the initial ^{26}Al abundance in a stardust grain is revealed by excesses in ^{26}Mg. This will be discussed in detail in Sect. 3.6.1. In general, radioactive signatures in stardust have the potential be used as clocks for the timescale of dust formation around stars and supernovae. Finally, stardust isotopic data provide a unique way to investigate the operation of the *s*-process in AGB stars, as will be discussed in Sect. 3.5.5.

3.5 Neutron Capture Nucleosynthesis in AGB Stars

In this section we show that:

- Free neutrons are produced in the TP-AGB phase by the ^{22}Ne$(\alpha, n)^{25}$Mg reaction, which activates at ∼300 MK and operates during He burning in the intershell convective region during thermal pulses, and the ^{13}C$(\alpha, n)^{16}$O reaction, which activates at ∼90 MK and operates in a radiative (and hence stable) region of the intershell during the H-burning phases. The free neutrons trigger the *s*-process, which produces half of the cosmic abundances of the elements heavier than iron via neutron captures mostly occurring on stable and long-lived radioactive nuclei.
- Unstable isotopes with half lives higher than a few days can also suffer neutron captures during the *s*-process, producing a wide variety of *branching points* on the *s*-process path, which define the details of the abundance distribution produced by the *s*-process as a function of neutron density and temperature.
- The overall *s*-process abundance distribution is defined by stable nuclei with a magic number of neutrons at the three *s*-process peaks at Sr, Ba, and Pb, and by the total amount of free neutrons available.
- Several long-lived unstable isotopes are produced by the *s*-process (details in Sect. 3.6.5). Among them are ^{93}Zr and ^{99}Tc. Observations of monoisotopic stable Nb (the daughter nucleus of ^{93}Zr) and of Tc itself can be used as discriminant between intrinsic (on the AGB) and extrinsic (with a former AGB binary companion) *s*-process-enhanced stars.

3.5.1 Neutron Sources in AGB Stars

In the double burning shell phase a nuclear reaction that may produce a copious neutron flux is ^{22}Ne$(\alpha$,n$)^{25}$Mg. ^{22}Ne is abundantly present in the intershell because

it directly derives from the initial abundance of O (the most abundant nucleus after H and He) as a consequence of the operation of the CNO cycle first and of a double α capture on ^{14}N later. This means that this neutron production channel is of *secondary* origin, i.e., its efficiency scales with the initial metallicity of the star. The relatively high Coulomb barrier of Ne (Z=10) pushes the threshold temperature for α capture above 300 MK so that this process can activate only within a hot He-burning region. Since the temperature at the base of the He convective shell during thermal pulses scales directly with the mass of the H-exhausted core, only stars initially more massive than $\simeq$3 $M_\odot$ (Iben 1975; Iben and Truran 1978) can efficiently activate this nuclear reaction. Panel b) in Fig. 3.9, shows a typical profile of the neutron density versus time associated with this neutron source. Its shape reflects the sharp rise of the temperature caused by the growth of the thermal instability and the following quite rapid decline due to the quenching of the instability. The high activation temperature and its very short duration (a few years) lead to a very high initial neutron density

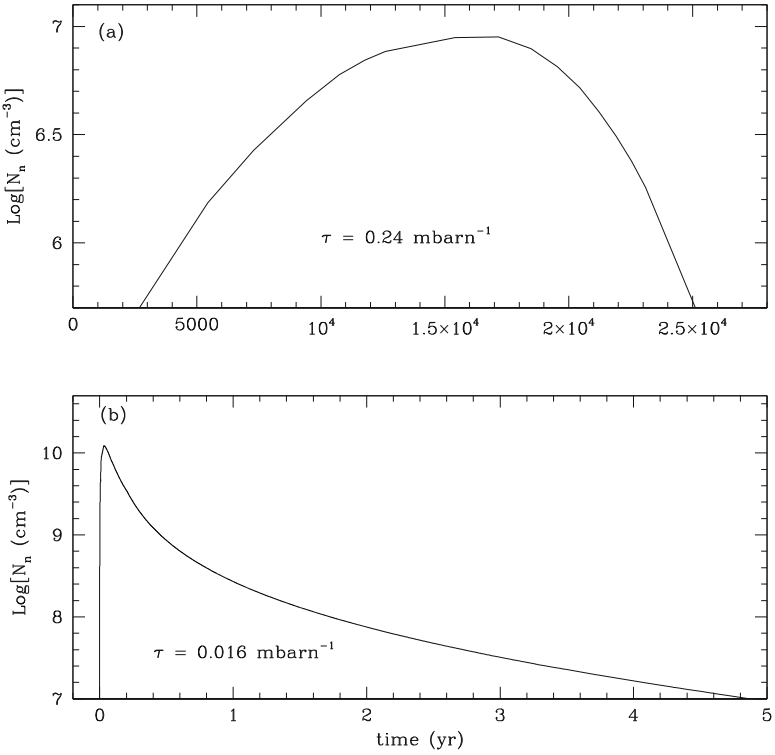

Fig. 3.9 Neutron densities as functions of time corresponding to the activation of the two neutron sources in a 3 $M_\odot$ AGB star model of solar metallicity during the last interpulse-pulse cycle: (**a**) the ^{13}C neutron source (the zero point in time represent the time from the start of the interpulse period, about 10,000 years, when the temperature reaches 79 MK); (**b**) the ^{22}Ne neutron source (the zero in time corresponds to the time when the temperature in the TP reaches 250 MK)

(reaching up to $N_n \simeq 10^{14}$ n/cm^3 in AGB stars of initial mass $\sim 6\,M_\odot$) but to a small total amount of ^{22}Ne burnt per cycle, so that the total number of neutrons released, i.e., the time-integrated neutron flux, or *neutron exposure* $\tau = \int_0^t N_n v_{th} dt$, remains quite small, of the order of a few hundredth of 1/mbarn[6] (see Sect. 3.5.2). The signature of such an impulsive neutron flux on neutron capture nucleosynthesis will be discussed in the next section. We only remark here an important difference between the neutron-capture nucleosynthesis occurring during AGB thermal pulses and that occurring in the He-convective shell of a massive star (other than the fact that in the AGB case the exposure to neutrons occurs recurrently): the mass of the He-convective shell in AGB stars is orders of magnitude smaller than that of a massive star so that the smaller dilution induced by the mixing allows, in the former case, many unstable nuclei to reach a higher equilibrium concentration. This occurrence favors the synthesis of stable nuclei on the neutron-rich side of the valley of β stability.

The problem with the ^{22}Ne neutron source is that AGB stars observed to be enriched in *s*-process elements have been identified as AGB stars of masses lower than $\sim 3\,M_\odot$ because (a) their relatively low luminosities (Frogel et al. 1990) match those of low-mass AGB models; (b) their surface is generally C enriched, an occurrence that rules out a significant HBB and hence an initial mass greater than $3\,M_\odot$; (c) excesses of ^{25}Mg, predicted to be produced by ^{22}Ne$(\alpha, n)^{25}$Mg, and of ^{26}Mg, predicted to be produced by the twin channel ^{22}Ne$(\alpha, \gamma)^{26}$Mg, with respect to ^{24}Mg are not observed (Smith and Lambert 1986; McWilliam and Lambert 1988); (d) the high neutron density produced by the ^{22}Ne channel, see Panel b) in Fig. 3.9, would favor the synthesis of neutron-rich nuclei like ^{96}Zr and elements as Rb, at odds with spectroscopic observations (Lambert et al. 1995; Abia et al. 2001) and the solar abundance distribution (Despain 1980). Thus, for the vast majority of *s*-enhanced AGB stars, another nuclear fuel for the production of neutrons has to be invoked.

Nuclei of ^{13}C are the best candidate for this role, given that the ^{13}C$(\alpha, n)^{16}$O reaction activates at temperatures from approximately 90 MK, which are easily reached in low-mass AGB stars. The achievement of the threshold temperature is, however, a necessary but not sufficient condition for a nuclear reaction to be effective: an additional requirement is the presence of a sufficient amount of reactants, in this case ^{13}C. We already pointed out in the previous section that models in which no mixing is allowed in the layers in radiative equilibrium do not naturally produce a significant concentration of ^{13}C in the intershell region. In fact, the ^{13}C available in the H-exhausted zone is that corresponding to the equilibrium value provided by the CNO cycle. As a neutron source for the *s*-process, this ^{13}C suffers two major problems: its abundance is too low to power a significant neutron flux and its ratio with respect to ^{14}N is too low (^{13}C/^{14}N$<<1$). The ^{14}N$(n, p)^{14}$C

[6] 1 mbarn = 10^{-27} cm^2.

reaction[7] has a relatively high neutron capture cross section of $\simeq$2 mbarn (Wallner et al. 2016), with respect to typical cross section of the order of 0.1–0.01 mbarn for the light nuclei. Hence, it is a formidable poison that can even completely inhibit the *s*-process. Hence, the ^{13}C neutron source represents a valid alternative to the ^{22}Ne neutron source only if additional ^{13}C is produced in an environment depleted in ^{14}N. A way out of this problem is to assume that at the end of each 3rd dredge-up episode a small amount of protons penetrates the intershell region. The amount of protons engulfed in the He/C rich intershell must be small ($Y_p/Y_{^{12}C} << 1$) because they must allow the conversion of ^{12}C into ^{13}C, but not the conversion of ^{13}C in ^{14}N. (Note that the intershell is essentially free of ^{14}N at the end of a thermal pulse because ^{14}N nuclei have all been destroyed by α captures.) Once a small amount of protons has penetrated the intershell, the progressive heating caused by the deposition of fresh He synthetized by the H-burning shell induces the conversion of ^{12}C in ^{13}C. We can estimate the concentration of protons that allows the build up of ^{13}C, but not of ^{14}N, by considering that the production rate of ^{14}N equates that of ^{13}C when the concentration of ^{13}C rises to a value of the order of 1/4 of that of ^{12}C (see Sect. 3.2.1). Since the mass fraction of ^{12}C in the intershell is about 0.2, the two rates equate each other for a ^{13}C concentration of $X_{^{13}C} \simeq 0.20\,(13/12)/4 = 5\,10^{-2}$. If one requires the ^{13}C production rate to dominate that of ^{14}N, the ^{13}C concentration must be reduced by at least a factor of 10, so that $X_{^{13}C} \simeq 5\,10^{-3}$. This abundance of ^{13}C corresponds to a proton concentration of the order of $X_p = X_{^{13}C}/13 = 4\,10^{-4}$.

A self-consistent scenario able to produce this small amount of protons penetrating below the base of the convective envelope has not been found yet: several mechanisms have been proposed (e.g. Iben and Renzini 1982; Herwig et al. 1997; Langer et al. 1999; Denissenkov and Tout 2003) but none of them can presently be considered as widely accepted. A discussion of these alternative scenarios goes well beyond the purposes of the present discussion. What matters, and what modelers often pragmatically assume, is that a small amount of protons definitely penetrates in the intershell at the end of 3rd dredge-up. The detailed features of the ^{13}C *pocket* obtained with such a procedure are subject to large uncertainties.

Nonetheless the basic properties of the neutron flux that is obtained in this way are considered relatively well understood (Gallino et al. 1998; Goriely and Mowlavi 2000; Lugaro et al. 2003b). The activation of the $^{13}C(\alpha, n)^{16}O$ occurs well before the onset of the next thermal pulse and the *s*-process nucleosynthesis triggered by this neutron source occurs at low temperature in a radiative environment (see Sect. 3.5.2). Panel a) in Fig. 3.9 shows the temporal evolution of this neutron flux. The rather long timescale over which this neutron flux remains active is determined by the speed at which the H-burning shell accretes matter on the He core, which means a typical timescale of the order of 10^4 years. Given such a long timescale, ^{13}C is totally consumed so that the total number of neutrons released is very large,

[7]This reaction produces ^{14}C, a radioactive nucleus with a half life of 5730 years. This nucleus is not carried to the stellar surface by the 3rd dredge-up because it is destroyed by $^{14}C(\alpha, n)^{18}O$ reactions during He-burning in the thermal pulse.

with neutron exposures of the order of a tenth to a few mbarn^{-1}. The neutron density, instead, keeps to low values, up to $N_n \simeq 10^8$ n/cm^3. Let us finally remark that the neutron flux produced by the ^{13}C neutron source is of *primary* origin, i.e., independent on the initial stellar metallicity, since the ^{13}C is made from ^{12}C synthetized starting from the initial H and He.

3.5.2 The s-Process in AGB Stars

A fraction of the free neutrons produced in AGB stars by the ^{13}C and ^{22}Ne neutron sources described above is captured by Fe seed nuclei, leading to production of elements with large atomic mass numbers up to Pb (A = 208) and Bi (A= 209) via the *s*-process. In general, a neutron flux that irradiates the surrounding matter reproduces a situation analogous to that occurring during H burning, where matter is irradiated by a flux of protons. While during a proton flux matter is pushed out of the valley of β stability toward the proton-rich side, during a neutron flux matter is pushed out of the valley of β stability valley toward the neutron-rich side. Thus, the presence of a neutron flux is inevitably associated to the synthesis of radioactive nuclei that, sooner or later, decay back towards the valley of β stability.

During the *s*-process, by definition, the timescale against β decay of an unstable isotope is shorter that its timescale against neutron captures. Thus, neutron captures occur only along the valley of β stability (Fig. 3.10). For this condition to hold neutron densities must be of the order of $N_n \sim 10^7$ n/cm^3. By comparison, during the *rapid* neutron-capture process (*r* process), instead, neutron densities reach values as high as 10^{20}–10^{25} n/cm^3 so that neutron captures occur on a time scale less than a second (typically much shorter than that of radioactive decays) pushing matter towards very neutron-rich material. When the neutron flux is extinguished, the neutron-rich radioactive nuclei quickly decays back towards their stable isobars

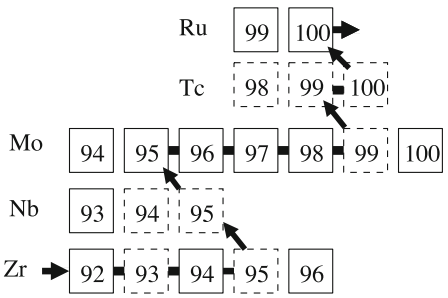

Fig. 3.10 The main *s*-process path along the valley of β stability from Zr to Ru is indicated by the thick solid line and arrows. Solid and dashed boxes represent stable and unstable nuclei, respectively. The radioactive nuclei ^{93}Zr and ^{99}Tc behave as stable during the *s* process as their half lifes (of the order of 10^5–10^6 years) are longer than the timescale of the *s*-process

on the valley of β stability. As presented in Chap. 4, the r-process is believed to occur in explosive conditions in supernovae.

In stellar conditions, though, neutron densities during the s-process can reach values orders of magnitude higher than 10^7 n/cm^3. Depending on the peak neutron density, as well as on the temperature and density, which can affect β-decay rates, conditions may occur for the neutron-capture reaction rate of an unstable isotope to compete with its decay rate. These unstable isotopes are known as *branching points* on the s-process path. To calculate the fraction of the s-process flux branching off the main s-process path at a given branching point a *branching factor* is defined as:

$$f_{branch} = \frac{p_{branch}}{p_{branch} + p_{main}},$$

where p_{branch} and p_{main} are the probabilities per unit time associated to the nuclear reactions suffered by the branching point nucleus and leading onto the branch or onto the main path of the s process, respectively.

There are several types of branching points: in the *classical* case p_{main} corresponds to λ, i.e., the probability per unit time of the unstable isotope to decay, and p_{branch} corresponds to p_n, i.e., the probability per unit time of the unstable isotope to capture a neutron $< \sigma v > N_n$, where N_n is the neutron density and $< \sigma v >$ is the Maxwellian averaged product of the velocity v and the neutron capture cross section σ.[8] A typical example of this case is the isotope ^{95}Zr in Fig. 3.10, which has a half life of 64 days, and can capture neutrons and produce the neutron-rich isotope ^{96}Zr, classically a product of the r-process, even during the s-process. When the branching point is a long-lived, or even stable isotope, but its β-decay rate increases with temperature, the opposite applies: $p_{branch} = \lambda$ and $p_{main} = p_n$. In even more complex situations, a radioactive isotope may suffer both β^+ and β^- decays, as well as neutron captures. In this case, three terms must be considered at denominators in the definition of the branching factor above: p_n, and λ for both β^+ and β^- decays.

Branching points have been fundamental in our understanding of the s-process conditions in AGB stars and will be discussed in more detail in Sect. 3.5.3. The low neutron density associated with the ^{13}C neutron source does not typically allow the opening of branching points. On the other hand, the high neutron density associated with the ^{22}Ne neutron source activate the operation of branching points on the s-process path, defining the details of the final abundance distribution.

It is possible to identify nuclei that can be produced only by the s process (*s-only* nuclei), which are shielded from r-process production by a stable isobar, or only by

[8]Note that σ is usually given in mbarn, corresponding to 10^{-27} cm^2, and that $< \sigma v >$ can be approximated to $\sigma \times v_{thermal}$, where $v_{thermal}$ is the thermal velocity. Neutron capture cross sections for (n, γ) reactions throughout this chapter are given at a temperature of 350 million degrees, corresponding to an energy of 30 keV, at which these rates are traditionally given. Values reported are from the Kadonis database (Karlsruhe Astrophysical Database of Nucleosynthesis in Stars, http://www.kadonis.org/) and the JINA reaclib database (http://groups.nscl.msu.edu/jina/reaclib/db/index.php), unless stated otherwise.

the r-process (r-*only* nuclei), which are not reached by neutron captures during the s-process as isotopes of the same element and same atomic mass number A-1 are unstable. Examples of s-only nuclei are ^{96}Mo and ^{100}Ru shown in Fig. 3.10, which are shielded by the r-only nuclei ^{96}Zr and ^{100}Mo, respectively. These, in turn, are not typically produced by the s-process as ^{95}Zr and ^{99}Mo are unstable. Proton-rich nuclei which cannot be reached by either the s- or the r-process must be produced via the *p-process*, i.e., proton captures or photodisintegration of heavier nuclei, and are labelled as *p-only* nuclei (e.g., ^{94}Mo in Fig. 3.10).

Models for the s-process have historically been tested against the solar system abundances of the s-only isotopes, as these were the first precise available constraints. Once a satisfactory fit is found to these abundances, the selected theoretical distribution can be used to determine the contribution from the s-process to each element and isotope. By subtracting this contribution to the total solar system abundance, an r-process contribution to each element can be obtained[9] (e.g. Kaeppeler et al. 1982; Arlandini et al. 1999), which has been widely used to test r-process models, and to compare to spectroscopic observations of stars showing the signature of the r-process (Sneden et al. 2008). For example, $\simeq$80% of the solar abundance of Ba is due to the s process, which is then classified as a typical s-process element, while $\simeq$5% of the solar abundance of Eu is due to the s process, which is then classified as a typical r-process element.

Already B^{2}FH had attributed to the operation of the s-process the three peaks in the solar abundance distribution at magic numbers of neutrons N=50, the Sr, Y, and Zr peak, N=82, the Ba and La peak, and N=126, the Pb peak. This is because nuclei with a magic number of neutrons behave with respect to neutron capture reactions in a similar way as atoms of noble gases do with respect to chemical reactions. Their energy levels, or shells, are fully populated by neutrons, in the case of magic nuclei, or by electrons, in the case of noble gases, and hence they are very stable and have a very low probability of capturing another neutron, in the case of magic nuclei, or of sharing electrons with another atom, in the case of noble gases. Nuclei with magic numbers of neutrons have small neutron-capture cross sections (of the order of a few to a few tens mbarn) with respect to other heavy nuclei, and they act as bottlenecks along the s-process path, leading to the observed abundance peaks. Nuclei located between the peaks, instead, have much higher neutron capture cross sections (of the order of a few hundred to a few thousand mbarn). The neutron-capture chain in these local regions in-between magic nuclei quickly reaches equilibrium during the s-process. During a neutron-capture process the abundance N_A of a stable isotope with atomic mass A varies with time as:

$$\frac{dN_A}{dt} = production\ term\ -\ destruction\ term$$

$$= N_{A-1} N_n \sigma_{A-1} \times v_{thermal} - N_A N_n \sigma_A \times v_{thermal}.$$

[9]The p-process contribution to elemental abundances is comparatively very small, $\simeq$1%, except in the case of Mo and Ru, which have magic and close-to-magic p-only isotopes, where it is up to $\simeq$25% and $\simeq$7%, respectively.

When replacing time with the neutron exposure τ one has:

$$\frac{dN_A}{d\tau} = N_{A-1}\sigma_{A-1} - N_A\sigma_A,$$

which, in steady-state conditions $\frac{dN_A}{d\tau} \rightarrow 0$ reached in between neutron magic nuclei, yields the simple rule to derive relative *s*-process abundances away from neutron magic numbers[10]:

$$N_A\sigma_A \simeq constant.$$

It follows that the relative abundances of nuclei in-between the peaks are only constrained by their neutron-capture cross sections and do not provide information on the *s*-process neutron exposure. On the other hand, the relative abundances of the elements belonging to the three different peaks almost uniquely constrain the *s*-process neutron exposure. This is the reason behind the introduction and wide usage, both theoretically and observationally, of the *s*-process labels *light s* (*ls*) and *heavy s* (*hs*), corresponding to the average abundances of the *s*-process elements belonging to the first and second peak, respectively, as well as behind the importance of the determination of the abundance of Pb, representing the third *s*-process peak. In AGB stars, the high neutron exposure associated with the ^{13}C neutron source drive the production of *s*-process elements even reaching up to the third *s*-process peak at Pb in low-metallicity AGB stars. On the other hand, the lower neutron exposure associated with the ^{22}Ne neutron source typically produces *s*-elements only up to the first *s*-process peak at Sr.

It is now ascertained that the *s*-process is responsible for the production of about half the abundances of the elements between Sr and Bi in the Universe (see, e.g., Kaeppeler et al. 1982) and that it occurs in AGB stars.[11] The first direct evidence that the *s*-process occurs in AGB stars—and, more generally, that nucleosynthesis is happening inside stars—was the identification in the 1950s of the absorption lines of atoms of the radioactive element Tc in the atmospheres of some cool giant stars. The longest-living isotopes of Tc are ^{97}Tc and ^{98}Tc, with a half life of 4.0 and 4.2 million years, respectively. Since these stars would have taken billions of years to evolve to the giant phase, the observed Tc could have not been present in the star initially. It follows that the Tc must have been produced by the *s*-process inside the stars (see also Neyskens et al. 2015). Actually, neutron captures do not produce ^{97,98}Tc, but the third longest-living isotope of this element: ^{99}Tc, with a terrestrial half life of 0.21 million years (Fig. 3.10). The presence of ^{99}Tc in AGB stars has

[10]For a detailed analytical description of the *s* process refer to Chapter 7 of Clayton (1968).

[11]Cosmic abundances of nuclei between Fe and Sr are also contributed by the *s*-process, but in this case by neutron captures occurring in massive stars during core He burning and shell C burning (Chapter 4 and, e.g., Raiteri et al. 1992; Pignatari et al. 2010).

been confirmed by measurements of the Ru isotopic composition in stardust SiC grains, as will be discussed in Sect. 3.6.5.

The presence of Tc in giant stars has also been used to classify different types of *s*-process enhanced stars. If a given observed *s*-process enriched giant star shows the lines of Tc, then it must be on the AGB and have enriched itself of *s*-process elements. In this case it is classified as *intrinsic s*-process enhanced star and typically belongs to one of the reddest and coolest subclasses of the spectroscopic class M: MS, S, SC, and C(N), where the different labels indicate specific spectral properties—S stars show zirconium oxide lines on top of the titanium oxide lines present in some M stars and C(N) stars have more carbon than oxygen in their atmospheres—or the transition cases between those properties—MS is the transition case between M stars and S stars and SC is the transition case between S and C(N) stars. On the other hand, if an *s*-process enriched giant star does not show the lines of Tc, it is classified as *extrinsic s*-process enhanced star. In this case its *s*-process enhancements have resulted from mass transfer from a binary companion, which was more massive and hence evolved first on the AGB phase. Stars belonging to the class of *extrinsic s*-process enhanced stars range from Ba stars in the Galactic disk, to the older halo populations of carbon-rich CH and Carbon-Enhanced Metal-Poor (CEMP) stars (e.g. Jorissen et al. 1998; Bond et al. 2000; Lucatello et al. 2005). Observations of Nb can also be used to discriminate intrinsic from extrinsic *s*-process enhanced stars as Nb is destroyed during the *s*-process, but receives a radiogenic contribution over time due to the β^- decay of ^{93}Zr, with half life 1.5 million years, which is on the *s*-process path (see Fig. 3.10).

The field of modelling the *s* process in AGB stars has boomed since 2010, with several groups presenting large sets of yields to be employed for a variety of applications, from the study of the chemical evolution of the Galaxy to the comparison to observational constraints from both stars and stardust grains. One of the most complete set of models can be found in the FRUITY database (http://fruity.oa-teramo.inaf.it/), which also includes models with stellar rotation and is based on the series of papers by Cristallo et al. (2016). Another set of models has been provided by Karakas and Lugaro (2016, and references therein). Finally, the NuGrid collaboration (http://www.nugridstars.org/) has also started to provide *s*-process AGB models (see, e.g., Pignatari et al. 2016). These sets of models are based on different computational tools and different choices for the implementation of the physical mechanisms behind the various features of the AGB phase, from the mass loss to the formation of the ^{13}C pocket. While comparison and analysis of these models, also in relation to the observational constraints, is still ongoing, first basic comparisons between the different model sets can be found, for example, in Karakas and Lugaro (2016). The main observation is that models of AGB stars of relatively low mass ($<4\,M_\odot$) produce results that are quite similar to each other, while for higher masses predictions diverge. A detailed analysis of the production in the different sets of new models of the long-lived radionuclei heavier than Fe discussed in Sect. 3.6.5 is the topic of future research.

3.5.3 Branchings and the s-Process in AGB Stars

Branching points at radioactive nuclei have provided for the past 50 years important tools to learn about conditions during the *s*-process in AGB stars. This is because branching factors depend on the neutron density and can also depend on the temperature and density of the stellar material. This happens in those cases when the decay rate of the branching nucleus is temperature and/or density dependent. These branching points are referred to as *thermometers* for the *s*-process. Traditionally, the solar abundances of isotopes affected by branching points were used to predict the neutron density and temperature at the *s*-process site using parametric models where parameters representing, e.g., the temperature and the neutron density were varied freely in order to match the observed abundances (e.g. Kaeppeler et al. 1982). Later, detailed information on branching points became available from spectroscopic observations of stellar atmospheres and from laboratory analyses of meteoritic stellar grains. At the same time, models for the *s*-process in AGB stars have evolved from parametric into stellar models, where the temperature and neutron density parameters governing the *s*-process are taken from detailed computation of the evolution of stellar structure (Gallino et al. 1998; Goriely and Mowlavi 2000; Cristallo et al. 2009; Karakas and Lugaro 2016). For these models branching points are particularly useful to constrain neutron-capture nucleosynthesis and conditions inside the thermal pulse because, typically, they open at high neutron densities during the high-temperature conditions that allow the activation of the ^{22}Ne neutron source in the convective intershell region.

As the temperature, density, and neutron density vary with time in the convective intershell region, branching factors also change over time. For example, a classical branching point, where the branching path corresponds to neutron capture, progressively opens while the neutron density reaches its maximum, and then closes again while the neutron density decreases and the main *s*-process path is restored. Of special interest is that toward the end of the thermal pulse the neutron density always decreases monotonically with the temperature and thus with time (Fig. 3.9) so that a *freeze out* time can be determined for a given nucleus, which represents the time after which the probability that the nucleus captures a neutron is smaller than unity and thus the abundances are *frozen* (Cosner et al. 1980). This can be calculated as the time when the neutron exposure τ left before the end of the neutron flux is $1/\sigma$, where σ is the neutron capture cross section of the nucleus.

As a general rule of thumb, branching points that have the chance of being activated at the neutron densities reached in AGB stars are those corresponding to radioactive nuclei with half lives longer than at least a couple days. These correspond to similar half lives against capturing a neutron for neutron densities $\simeq 10^9 - 10^{11}$ n/cm^3, at AGB *s*-process temperatures. Isotopes with half lives longer than approximately 10,000 years can be considered stable in this context as the *s*-process flux in AGB stars typically lasts less than this time. We refer to these isotopes as long-lived isotopes and we discuss their production in AGB stars in

detail in Sect. 3.6.5. Very long-lived isotopes—half lives longer than ∼10 Myr—include for example ^{87}Rb, and are considered stable in our context.

A list of unstable isotopes at which branching points that become relevant in the *s*-process reaction chain in AGB stars is presented in Appendix B of this book as a complete reference to be compared against observational information and as a tool for the building of *s*-process networks. Worth special mention are the branching points at ^{79}Se, ^{85}Kr, and ^{176}Lu for the involvement of isomeric states of these nuclei, at ^{151}Sm, one among a limited number of branching points for which an experimental estimate of the neutron-capture cross section is available, at ^{86}Rb, responsible for the production of the very long-living ^{87}Rb, and at ^{163}Dy and ^{179}Hf, which are stable nuclei in terrestrial conditions that become unstable in AGB stellar interiors.

Taken as a whole, the list of branching points that may be operating during the *s*-process in AGB stars sets a powerful group of constraints on our theoretical *s*-process scenarios. They are particularly effective when each of them is matched to the most detailed available observations of its effects. For example, some elemental abundance ratios and isotopic ratios that are affected by branching points can be measured from a stellar spectrum via identification and analysis of different emission or absorption lines. In these cases, model predictions can be compared directly to stellar observations of *s*-process-enhanced stars (Sect. 3.5.4). Isotopic ratios affected by branching points involving isotopes of refractory elements, but also of noble gases, have been or have the potential to be measured in meteoritic stardust SiC grains from AGB stars and provide unique constraints due to the large and expanding high-precision dataset available on the composition of stardust (Sect. 3.5.5). The values of the solar abundance ratios of *s*-only isotopes affected by branching points (e.g., ^{134}Ba/^{136}Ba, ^{128}Xe/^{130}Xe, and ^{176}Hf/^{176}Lu) must be matched by any *s*-process model. When these involve nuclei with peculiar structure, such as ^{176}Lu, combined investigation of nuclear properties and *s*-process models drives progress in our understanding of both.

One advantage of the computation of branching points in AGB stars is that the activation of one branching point is almost completely independent from the activation of all the other branching points because the overall neutron flux is only very marginally affected by the details of the *s*-process path. Thus, it is possible to include in a *s*-process nuclear network only the branching points of interest for a specific problem, or a specific element, hence keeping it simple and saving computational time.

One overall drawback of using branching points to understand the *s*-process is that for the vast majority of the radioactive nuclei involved there exist only theoretical or phenomenological determinations of their neutron-capture cross sections and of the temperature and density dependence of their decay rates. This is due to the difficulty of producing experimental data for radioactive targets (see Chap. 9) and means that there are always some uncertainties associated to model predictions of the effect of branching points. These errors and their effect need to be carefully evaluated in every single case.

3.5.4 Signatures of s-Process Branching Points: Rb, Zr, Eu

The abundance of ^{87}Rb, which can be produced in AGB stars via activation of the branching point at ^{86}Rb, is a famous example of how detailed comparison of theoretical *s*-process abundances to the abundances observed in *s*-process-enhanced stars provide a stringent test to our understanding of the *s* process and AGB stars. The abundance of ^{87}Rb is particularly interesting because the element Rb can be spectroscopically identified and its abundance determined in AGB stars. Overall, Rb is an *r*-process element—only 22% of its solar abundance can be ascribed to the *s*-process (Arlandini et al. 1999)—made up of two isotopes: ^{85}Rb and the very long-lived ^{87}Rb, which is treated as a stable isotope in this context. Specifically, 92% of solar ^{85}Rb is made by the *r*-process because this nucleus has a relatively large neutron capture cross section of 234 mbarn and thus it does not accumulate to high abundances during the *s*-process. On the other hand, ^{87}Rb, as described in Appendix B, has a magic number of neutrons N=50, and thus a relatively small neutron capture cross section of 15.7 mbarn. Hence, if it is reached by the *s*-process reaction chain via the activation of the branching points at ^{85}Kr and ^{86}Rb, it accumulates and is significantly produced. It follows that when these branching points are activated during the *s*-process, the abundance ^{87}Rb represents a fraction of the total abundance of *s*-process Rb larger than the initial solar fraction. This is illustrated in the top panel of Fig. 3.11. In the case of the massive AGB model, where the ^{22}Ne neutron source is activated, the *s*-process occurs at high neutron density, and branching points are open, almost half of the final total abundance of Rb is made by ^{87}Rb. In the case of the low-mass AGB model, instead, where the ^{13}C neutron source is activated, the *s*-process occurs at low neutron density, and branching points are closed, only a quarter of the final total abundance of Rb is made by ^{87}Rb.

The ratio of the abundance of Rb to that of a neighbouring *s*-process element, such as Sr, or Zr, whose overall abundance is instead not affected by the activation of branching points, can be determined in AGB stars and has been widely used as an indicator of the neutron density at which the *s*-process occurs. Observations of Rb/Zr ratios lower than solar in MS, S, and C stars have strongly supported the theoretical scenario where the main neutron source in these low-mass AGB stars is the ^{13}C$(\alpha, n)^{16}$O reaction. This is because this neutron source produces neutron densities too low to increase the Rb/Zr ratio above the solar value (see lower panel of Fig. 3.11 and Lambert et al. 1995; Abia et al. 2001).

Massive AGB stars ($> 4{:}5\,M_{\odot}$) have only recently been identified in our Galaxy (García-Hernández et al. 2006, 2007; Pérez-Mesa et al. 2017). They belong to the group of OH/IR stars and they have been singled out as massive AGB stars on the basis of their location closer to the galactic plane, which indicates that they belong to a more massive stellar population, and their longer pulsation periods ($\simeq$400 days). Rb/Zr ratios in these stars are observed to be well above the solar value, which has given ground to the theoretical scenario where the main neutron source in these massive AGB stars must be the ^{22}Ne$(\alpha, n)^{25}$Mg reaction, which produces neutron

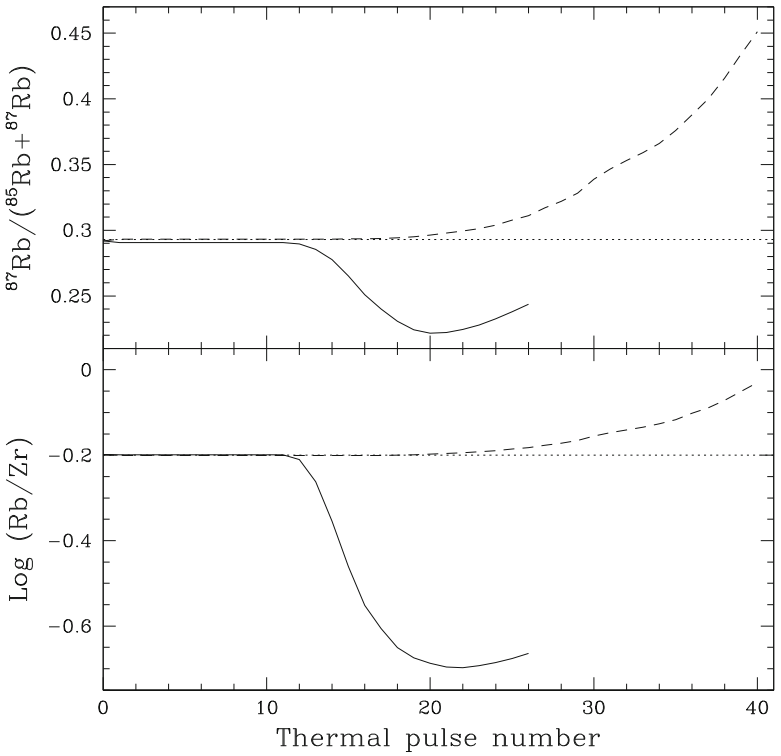

Fig. 3.11 Ratio of ^{87}Rb to the total abundance of Rb (top panel) and the Rb/Zr ratio (lower panel) computed in two solar metallicity AGB models (from van Raai et al. 2012). The dotted lines represent the initial solar ratios. The solid lines represent a massive (6.5 $M_{\odot}$) AGB model experiencing the activation of the ^{22}Ne neutron source only, and a low-mass (3 $M_{\odot}$) model experiencing the activation of the ^{13}C neutron source only (except for a marginal activation of the ^{22}Ne neutron source in the latest thermal pulses leading to the small final increase in the ^{87}Rb and Rb abundances)

densities high enough to increase the Rb/Zr ratio above the solar value (see lower panel of Fig. 3.11).

Another indicator of the neutron density measured in AGB stars is the isotopic abundance of ^{96}Zr, which is produced if the branching point at ^{95}Zr is activated. Zr isotopic ratios were determined via observations of molecular lines of ZrO in a sample of S stars (Lambert et al. 1995). No evidence was found for the presence of ^{96}Zr in these stars. This result provides further evidence that the neutron density in low-mass AGB stars must be low. A low ^{96}Zr abundance has been confirmed by high-precision data of the Zr isotopic ratios in stardust SiC grains, which are discussed in the following Sect. 3.5.5.

Isotopic information from stellar spectra has also been derived for the typical *r*-process element Eu in old Main Sequence stars belonging to the halo of our Galaxy and enhanced in heavy neutron-capture elements (Sneden et al. 2008). This has

been possible because the atomic lines of Eu differ significantly if the Eu atoms are made of ^{151}Eu instead of ^{153}Eu, the two stable isotopes of Eu. In old stars showing overall enhancements of *r*-process elements, the total Eu abundance is roughly equally divided between ^{151}Eu and ^{153}Eu. This fraction is consistent with the solar fraction, and it is expected by Eu production due to the *r*-process (Sneden et al. 2002; Aoki et al. 2003a). On the other hand, in two old stars showing overall enhancements in *s*- and *r*-process elements, roughly 60% of Eu is in the form of ^{151}Eu (Aoki et al. 2003b). How these stars gained enhancements in the abundances of both *r*- and *s*-process elements has been an unsolved puzzle of the study of the origin of the elements heavier than iron in the Galaxy (Jonsell et al. 2006). This is because according to our current knowledge, the *r*- and the *s*-process are completely independent of each other, and occur in very different types of stars, neutron star mergers and possibly peculiar environments within core-collapse supernovae (Thielemann et al. 2011; Côté et al. 2017) and AGB stars, respectively. As will be discussed in Sect. 3.5.6, recently an *intermediate*-process origin for these peculiar abundance patterns has been proposed (Hampel et al. 2016). During the *s*- and the *i*-processes, the Eu isotopic fraction is determined mostly by the activation of the branching point at ^{151}Sm. Hence, the determination of the Eu isotopic ratios is a fundamental clue, which may help in solving the origin of these old stars. As more observations become available, the role of branching points during the *s*-process in AGB stars becomes more and more crucial to answering the questions on the origin of the heavy elements.

3.5.5 SiC Grains from AGB Stars and Branching Points

Stardust SiC grains from AGB stars represent a unique opportunity to study *s*-process conditions in the parent stars of the grains through the effect of the operation of branching points because SiC grains contain trace amounts of atoms of elements heavier than iron, which allow high-precision measurements of their isotopic ratios. Refractory heavy elements, such as Sr, Ba, Nd, and Sm, condensed from the stellar gas directly into the SiC grains while the grains were forming. Their isotopic composition have been determined from samples of meteoritic residual materials containing a large number of SiC grains using TIMS and SIMS (see Chap. 10, Sect 10.2 and Ott and Begemann 1990; Zinner et al. 1991; Prombo et al. 1993; Podosek et al. 2004). High-resolution SIMS has also been applied to derive data in single stardust SiC grains for Ba with the NanoSIMS (see Sect. 10.2 and Marhas et al. 2007) and Ba, Eu, and W with the SHRIMP (Sensitive High Resolution Ion Microprobe, e.g. Ávila et al. 2012). Isotopic ratios in a sample containing a large number of SiC grains for many elements in the mass range from Ba to Hf were also measured by ICPMS (Sect 10.2 and Yin et al. 2006).

A general drawback of these experimental methods is that they do not allow to separate ions of same mass but different elements. Hence, interferences by isotopes of the same mass (isobars) are present, which is especially problematic

for the elements heavier than iron where a large number of stable isobars can be found. Branching points, in particular, by definition affect the relative abundances of isobars, thus, with the methods above it is difficult to derive precise constraints on the effect of branching points on isotopic ratios. For example, the isobars ^{96}Mo and ^{96}Zr cannot be distinguished in these measurements, and thus it is not possible to derive information on the operation of the branching point at ^{95}Zr.

Exceptions to this problem are the stable Eu isotopes, ^{151}Eu and ^{153}Eu, which do not have stable isobars and thus their ratio can be measured and used to constrain the neutron density and the temperature during the *s* process in the parent stars of the grains via the branching points at ^{151}Sm and ^{152}Eu (Ávila et al. 2013), and the Ba isotopes, which are not affected by isobaric interferences because their isobars, the isotopes of the noble gas Xe isotopes, are present in very low amounts in the grains and are difficult to ionize and extract from the stardust (see specific discussion below in this section.) The Ba isotopic ratios, in particular the ^{134}Ba/^{136}Ba and the ^{137}Ba/^{136}Ba ratios, can be affected by branching points at the Cs isotopes (see below and Prombo et al. 1993; Marhas et al. 2007; Liu et al. 2014b).

The application of RIMS (Sect. 10.2) to the analysis of heavy elements in SiC grains has allowed to overcome the problem of isobaric interferences, at the same time providing an experimental method of very high sensitivity, which allows the measurements of trace elements in single stardust grains (Savina et al. 2003b). Since RIMS can select which element is ionized and extracted form the grains, mass interferences are automatically avoided. The Chicago-Argonne RIMS for Mass Analysis CHARISMA has been applied to date to the measurement of Zr (Nicolussi et al. 1997; Liu et al. 2014a), Mo (Nicolussi et al. 1998a), Sr (Nicolussi et al. 1998b; Liu et al. 2015), Ba (Savina et al. 2003a; Liu et al. 2014b, 2015) and Ru (Savina et al. 2004) in large single SiC grains (average size 3 μm), providing high-precision constraints on the operation of the *s*-process branching points that may affect the isotopic composition of these elements. Recently, a new improved instrument has come on-line: the Chicago Instrument for Laser Ionization (CHILI) (Stephan et al. 2016), which is expected to drive an enormous improvement in the amount and quality of the data in coming years. Analysis of SiC from AGB stars with CHILI has been performed so far for Fe and Ni (Trappitsch et al. 2018). A detailed comparison between data and models (Lugaro et al. 2003a, 2014b, 2018; Liu et al. 2015; Palmerini et al. 2018) shows that AGB stellar models of low mass and roughly-solar metallicity, where the ^{13}C$(\alpha, n)^{16}$O reaction is the main neutron source and the ^{22}Ne$(\alpha, n)^{25}$Mg is only marginally activated, provide the best match to all measured isotopic ratios affected by branching points.

For example, the ^{96}Zr/^{94}Zr ratio is observed in all measured single SiC to be lower than solar by at least 50%. Low-mass AGB models can reproduce this constraint due to the low neutron density associated with the main ^{13}C neutron source, in which conditions ^{96}Zr behaves like a typical *r*-only nucleus and is destroyed during the neutron flux. Massive AGB stars ($>4{:}5\,M_{\odot}$), on the other hand, experience high neutron densities and produce ^{96}Zr/^{94}Zr ratios higher than solar. In more detail, the ^{96}Zr/^{94}Zr ratio at the stellar surface of low-mass AGB stellar models reaches a minimum of $\simeq$90% lower than solar after roughly ten 3rd

dredge-up episodes, and then may increase again, due to the marginal activation of the ^{22}Ne neutron source in the latest thermal pulses. This predicted range allows to cover most of the ^{96}Zr/^{94}Zr of single SiC grains (see Fig. 5 of Lugaro et al. 2003a).

Another interesting example is the ^{134}Ba/^{136}Ba ratio, where both isotopes are *s*-only nuclei. During the low-neutron density flux provided by the ^{13}C neutron source the branching point at ^{134}Cs is closed and the ^{134}Ba/^{136}Ba ratio at the stellar surface reaches up to $\simeq$ 20% higher than the solar ratio after roughly ten 3rd dredge-up episodes. This value is too high to match the composition of single SiC grains. However, during the marginal activation of the ^{22}Ne in the later thermal pulses, the branching point at ^{134}Cs is activated, ^{134}Ba is skipped during the *s*-process flux and the ^{134}Ba/^{136}Ba ratio at the stellar surface is lowered down to the observed values roughly 10% higher than the solar value (see Fig. 14 of Lugaro et al. 2003a).

The ^{137}Ba/^{136}Ba ratio is another indicator of the neutron density because the activation of the chain of branching points along the Cs isotopes can produce ^{137}Cs, which decays into ^{137}Ba with a half life of 30 years. Grain data do not show any contribution of ^{137}Cs to ^{137}Ba, indicating that the Cs branching points beyond ^{134}Cs are not activated in the parent stars of the grains (see Fig. 14 of Lugaro et al. 2003a). This, again, excludes massive AGB stars, with an important neutron contribution from the ^{22}Ne neutron source, as the parent stars of the grains.

Another example of the signature of the *s*-process in meteorites is represented by very small variations, of the order of parts per ten thousand, observed in various elements in different types of meteoritic samples (Dauphas and Schauble 2016, see review by). For example, osmium isotopic ratios of primitive chondritic meteorites present a fascinating anomaly that looks like a *mirror s*-process signature, meaning that they show exactly the opposite behaviour expected if the meteorite had a component carrying an *s*-process signature. They are thus interpreted as a sign of incomplete assimilation of stardust SiC grains within the meteorite (Brandon et al. 2005). The branching points at ^{185}W and ^{186}Re make the ^{186}Os/^{188}Os ratio a indicator of the neutron density for the *s* process and the value for this ratio observed in chondrites suggest a low neutron density of $N_n = 3 \times 10^8$ n/cm^3 (Humayun and Brandon 2007), in agreement with other evidence discussed above.

Differently from refractory elements, the noble gases He, Ne, Ar, Kr, and Xe are not chemically reactive. Still, they are found in SiC, even if in extremely low quantities. Their atoms could have been *implanted* into dust grains that already had formed earlier (Heck et al. 2007, 2009; Verchovsky et al. 2004).

It has been possible to extract noble gases from meteoritic samples by RIMS (see Chap. 11), laser gas extraction (Nichols et al. 1991) and stepped-heating combustion of the sample to high temperatures, up to 2000° (Lewis et al. 1994). In particular, for the heavy nobler gases Kr and Xe, since their abundances are very low in stardust and the stepped-heating experimental method does not provide high extraction efficiency, it has been possible to extract their ions only from a large amount of meteoritic residual material. The derived Kr and Xe isotopic data is thus the average over a large number—millions—of grains. Differential information as function of the grain sizes can still be obtained by preparing the meteoritical residual in a way that selects the size of the grains to be found in it.

The composition of Xe in SiC corresponds to the famous Xe-S component, one of the first signature of the presence of pure stellar material in primitives meteorites (see Chap. 2, section), thus named because of its obvious *s*-process signature: excesses in the *s*-only isotopes ^{128,130}Xe and deficits in the *r*-only and *p*-only isotopes ^{124,126,136}Xe (all with respect to the solar composition). The ^{134}Xe/^{130}Xe ratio may be affected by the operation of the branching point at ^{133}Xe during the *s*-process. This isotopic ratio in stardust SiC is very close to zero, indicating that the Xe trapped in SiC grains did not experience *s*-process with high neutron density (Pignatari et al. 2004). This again allows the mass and metallicity of the parent stars of the grains to be constrained to low-mass AGB stars of roughly solar metallicity, in agreement with the conclusions drawn from the composition of the refractory elements.

The situation regarding the Kr isotopic ratios measured in SiC grains is much more complex. There are two branching points affecting the Kr isotopic composition: ^{79}Se and ^{85}Kr, changing the abundances of ^{80}Kr and ^{86}Kr, respectively, and both of them are tricky to model (see description in Appendix B). Moreover, the Kr atoms in stardust SiC appear to be consistent with implantation models of this gas into the grains only if these models consider two different components of implanted Kr (Verchovsky et al. 2004). One component was ionized and implanted in SiC at low energy, corresponding to a velocity of 5–30 km s^{-1}, typical of AGB stellar winds, the other component was ionized and implanted at high energy, corresponding to a velocity of a few thousands km/s, typical of the winds driven from the central star during the planetary nebular phase. In the second situation, which is the case also for all the He, Ar, and Ne atoms found in SiC, the isotopic composition of the noble gases indicate that they must have come directly from the deep He-rich and *s*-process-rich layers of the star, with very small dilution with the envelope material of initial solar composition. This is consistent with the fact that at this point in time the initial envelope material would have almost completely been peeled away by the stellar winds.

While the Kr AGB component is observed to be prominent in the small grains (of average size 0.4 μm) and shows low ^{86}Kr/^{82}Kr and high ^{80}Kr/^{82}Kr ratios, in agreement again with low neutron density *s*-process AGB models, the Kr planetary-nebula component is observed to be prominent in the largest grains (average size 3 μm) and shows high ^{86}Kr/^{82}Kr and low ^{80}Kr/^{82}Kr ratios, as expected instead in pure He-rich intershell material due to the higher neutron density *s*-process occurring in the final AGB thermal pulses (Pignatari et al. 2006; Raut et al. 2013). Actually, it is difficult to reproduce the ^{86}Kr/^{82}Kr up to twice the solar value observed in the largest grains even using the final pure *s*-process intershell composition of low-mass and solar metallicity AGB stellar models. This high ^{86}Kr/^{82}Kr ratios may be the signature of high-neutron density *s*-process nucleosynthesis occurring in *late* and *very late* thermal pulses during the post-AGB phase (see, e.g., Herwig et al. 1999), rather than during the AGB phase. Detailed *s*-process models are currently missing for this phase of stellar evolution.

In summary, the detailed information provided by stardust data on the isotopic ratios affected by branching points at radioactive nuclei on the *s*-process path has

allowed us to pinpoint the characteristics of the neutron flux that the parent stars of stardust SiC grains must have experienced. The vast amount of information on the composition of light and heavy elements in SiC grains has allowed us to infer with a high degree of confidence that the vast majority of these grains came from C-rich AGB stars, i.e., C(N) stars, which have C>O in their envelope, the condition for SiC grain formation, of low mass and metallicity close to solar. In turn, the stardust data has been used to refine our theoretical ideas of the *s*-process in these stars confirming that ^{13}C nuclei must be the main neutron source, while the ^{22}Ne neutron source is only marginally active.

3.5.6 The Intermediate Neutron-Capture Process

The traditional view of a clear separation between the main two cosmic neutron-capture processes originally proposed by B^{2}FH, the *slow* (*s*) and the *rapid* (*r*) neutron-capture processes, has been modified from the beginning of the 2010 decade by the need to introduce a new *intermediate* (*i*) neutron-capture process. As the name reflects, the *i* process is expected to occur for neutron densities intermediate between the typical *s*-process ($\sim 10^{7-12}$ n/cm^3) and the typical *r*-process neutron densities ($>10^{20}$ n/cm^3), in a regime of $N_n \sim 10^{13} - 10^{15}$ n/cm^3. In this situation the neutron-capture flux proceeds somewhat further away to the right of the valley of β stability than in the case of the *s* process: all the branching points listed in Appendix B are expected to work very efficiently, as well as further branching points not listed there but with significant probability to capture a neutron at the typical *i*-process neutron densities. One important example is the case of the branching point at ^{135}Xe. This isotope has a half life of approximately 9 h, hence, it is not activated in *s*-process conditions. However, during the *i*-process it captures neutrons producing the stable ^{136}Xe, which has a magic number of neutrons, a very low neutron capture cross section (less than 1 mbarn), and accumulates during the production flux. The result is that Xe is a main product of the *i*-process, contrarily to the *s* process. A similar case can be described for Kr, due to accumulation of ^{86}Kr, and Rb, due to accumulation of ^{87}Rb.

While the possibility of an *i* process was originally proposed by Cowan and Rose (1977), the idea of it has been revived only recently when its existence in nature has become evident from several observational constraints. The first was the observed pattern of the abundances of the elements heavier than iron in Sakurai's object (Herwig et al. 2011), a post-AGB star that appears to have experienced a H-ingestion event in 1994. An H-ingestion means that some protons are mixed into a He-burning TP. This results in a "flash", i.e., a sudden release of energy due to H-burning at high temperature, and the production of the neutron source ^{13}C releasing a neutron burst at relatively short timescale, hence, high density. Another clear indication of the existence of the *i*-process has come from the CEMP stars originally named CEMP-*s*/*r* because of being enriched both in Ba (an *s*-process element) and Eu (an *r*-process element). The current best model to explain such

pattern can be found using the *i* process (Dardelet et al. 2014; Hampel et al. 2016). In fact, Hampel et al. (2016) suggested to rename these stars CEMP-*i*.

There are several main problems currently related to our understanding of the *i* process. First, modelling H ingestion episodes is far from trivial, and most of the current simulations of the *i* process rely on some level of parametrisation. For example, the amount of ingested protons is treated as a free parameter, as well as the timescale of the process. While the former mainly determines the neutron density, to be adjusted such as it reaches the values required by the *i* process, the latter influences the total time-integrated number of neutrons (i.e., the neutron exposure τ). Similarly to the *s* process, low neutron exposures result in an *i* process that favours the production of the elements at the first magic neutron number beyond Fe of 50 (Kr and Rb, in this case). This is required by Sakurai's object and possibly other peculiar low-metallicity stars (Roederer et al. 2016). High neutron exposures, instead, result in an *i* process that favours the production of the elements at the second neutron number beyond Fe of 82 (Xe and Ba), as required by CEMP-*i*.

The other main problem currently related to the *i* process is the identification of its stellar site. For example, for CEMP-*i*, H-ingestion episodes similar to those reported for Sakurai's object have been found to be present in low-metallicity low-mass AGB stellar models, which presumably are the binary companions of CEMP-*i* stars (see, e.g., Campbell and Lattanzio 2008, and references therein). These ingestions, however, can also potentially occur in a variety of other environments including Super-AGB stars (Jones et al. 2016) and massive star, both during the pre-supernova and supernova phases. They are also seen to occur in models of rapidly accreting white dwarves (Denissenkov et al. 2017). While research is ongoing to establish more accurate scenarios for the operation, the occurrence, and the astrophysical site of the *i* process, its potential impact on galactic cosmic abundances will also need to be considered.

The impact of the *i* process on the production of long-lived isotopes affected by branching points discussed in the next section (e.g., ^{60}Fe and ^{182}Hf) remains to be investigated, although, it can be predicted that the high neutron density characteristic of the *i* process will results in enhanced production of such isotopes. If this effect will be important in relation to observational constraints remains to be seen.

3.6 Nucleosynthesis of Long-Lived Isotopes in AGB Stars

3.6.1 ^{26}*Al*

The famous long-lived radioactive nucleus ^{26}Al (with half life of 0.7 Myr), of interest from the point of view of γ-ray observations, meteoritic stellar grains, and the composition of the early solar system, can be produced in AGB stars via proton captures on ^{25}Mg, i.e., the ^{25}Mg$(p, \gamma)^{26}$Al reaction, when the temperature is above $\simeq$60 MK (Mowlavi and Meynet 2000; van Raai et al. 2008; Straniero et al. 2013). As

detailed in Sect. 3.4.1, proton captures occur in AGB stars between thermal pulses in two different locations: (1) in the H-burning shell on top of the He-rich intershell, and (2) at the base of the convective envelope in massive AGB stars, above $\simeq 4\,M_\odot$ (in the process known as Hot Bottom Burning, HBB, Sect. 3.4.1).

In setting (1), the intershell material is progressively enriched in ^{26}Al as proton captures in the H-burning shell convert 80% of ^{25}Mg into ^{26}Al. The efficiency of this conversion is determined by the fraction of 20% of ^{25}Mg+p reactions producing the isomeric, rather than the ground, state of ^{26}Al, which quickly decays into ^{26}Mg with a half life of $\simeq$6 s. Most intershell ^{26}Al abundance, however, is destroyed by neutron captures before having the chance of being dredged-up to the stellar surface via the 3rd dredge-up. This is because the neutron capture cross sections of ^{26}Al, in particular the $(n,\ p)$ and (n, α) channels, are very efficient: $\sigma \simeq 250$ and 180 mbarn, respectively.

Already during the interpulse period some ^{26}Al is destroyed by neutron captures. This is because in the bottom layers of the ashes of H burning the temperature reaches 90 MK, high enough for the ^{13}C(α,n)^{16}O reaction to occur using as fuel the ^{13}C nuclei in ashes of H burning produced by CNO cycling. The neutrons released in this region are of no interest to the *s* process because they are captured by the abundant light elements ^{14}N, and ^{26}Al itself, with relatively high neutron capture cross sections (see also Sect. 3.5.1). Then, neutron captures in the following thermal pulse destroy most of the ^{26}Al that was left over in the H-burning ashes. First, the ^{13}C nuclei that had survived in the top layers of the H-burning ashes are engulfed in the convective pulse, where the temperature quickly reaches 200 MK and the ^{13}C(α,n)^{16}O reaction is very efficiently activated. Again, these neutrons do not contribute to any *s*-process nucleosynthesis as they get mostly captured by ^{14}N and ^{26}Al. Second, the neutrons that may be released by the ^{22}Ne(α,n)^{25}Mg reaction later on in the convective pulse, when the temperature is higher than roughly 250 MK, contribute to further destruction of ^{26}Al. In this phase ^{26}Al can be completely destroyed, depending on the temperature reached at the base of the convective pulse, which controls the efficiency of the ^{22}Ne(α,n)^{25}Mg reaction. If the temperature reaches up to 300 MK, the ^{26}Al abundance is decreased by two orders of magnitude in the He-rich intershell at the end of the thermal pulse.

When the 3rd dredge-up occurs after the thermal pulse is extinguished, only a small mass of ^{26}Al is carried from the intershell to the stellar surface, of the order of $10^{-8}\,M_\odot$, mostly coming from a tiny region (roughly $10^{-4}\,M_\odot$) at the top of the intershell, which was not ingested in the convective pulse and thus did not experience the availability of free neutrons. This small abundance of ^{26}Al carried into the envelope translates into a small total contribution of the AGB winds to the abundance of ^{26}Al in the interstellar medium (also defined as *yield*) of $10^{-7}\,M_\odot$, for AGB stars of masses between $1\,M_\odot$ and $4\,M_\odot$, depending on the metallicity (upper panel of Fig. 3.12), though allowing a noticeable increase in the ^{26}Al/^{27}Al ratio at the stellar surface, up to a typical value of 2×10^{-3} (lower panel of Fig. 3.12).

The situation is very different for AGB stars of masses higher than approximately $4\,M_\odot$. Proton-captures occurring in setting (2), i.e., HBB at the base of the convective envelope, combined with the 3rd dredged-up of ^{25}Mg produced from

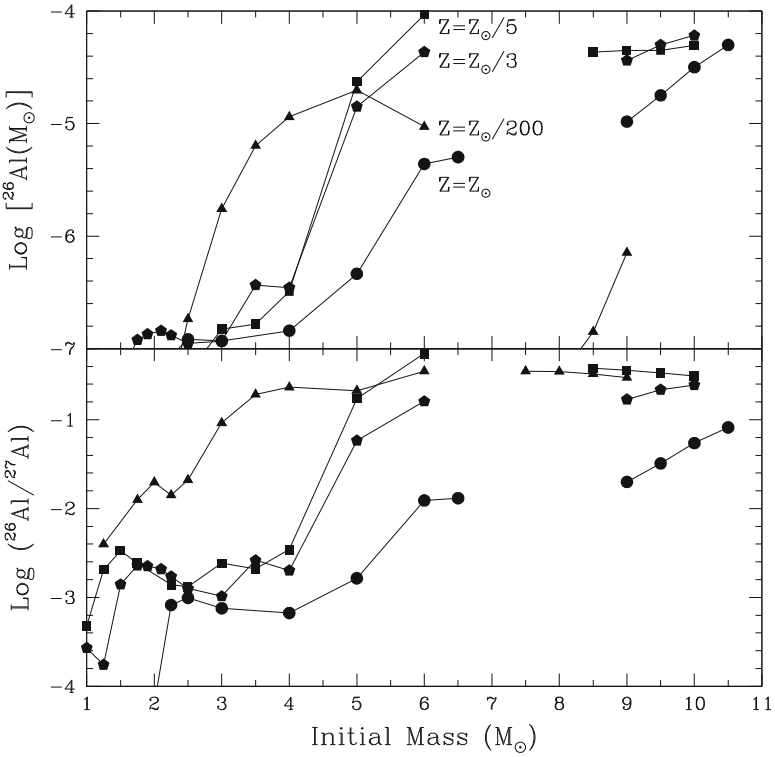

Fig. 3.12 The yields of ^{26}Al (top panel) for stellar models of different masses and metallicities (Z) from Karakas and Lattanzio (2007) for AGB stars of masses up to 6 $M_\odot$, and from Siess and Arnould (2008) for the more massive Super-AGB stars. Yields are defined as the total mass of ^{26}Al (in $M_\odot$) lost in the wind during the whole evolution of the star (calculated as the average of the time-dependent envelope composition weighed on the mass lost at each time). The ratios of the yield of ^{26}Al to the yield of ^{27}Al are also shown in the bottom panel

efficient activation of the ^{22}Ne(α,n)^{25}Mg reaction in the thermal pulse, produces large amounts of ^{26}Al. These are directly mixed to the stellar surface via the envelope convection resulting in yields up to 10^{-4} $M_\odot$, and ^{26}Al/^{27}Al ratios up to 0.5 (Fig. 3.12). During HBB the main channel for ^{26}Al destruction is proton captures on ^{26}Al itself, i.e., ^{26}Al(p, γ)^{27}Si reactions. Also in Super-AGB stars HBB produces large quantities of ^{26}Al (Siess and Arnould 2008; Lugaro et al. 2012).

Figure 3.12 shows the yields of ^{26}Al and their ratio with the yield of ^{27}Al for a variety of AGB stars and Super-AGB of different masses and metallicities. The plot shows how the efficiency of ^{26}Al production increases with stellar mass and with decreasing metallicity of the stars. This is because the efficiency of the HBB depends on the temperature at the base of the convective envelope, which is higher for higher masses and lower metallicities. For example, a 3.5 $M_\odot$ star of metallicity 200 times lower than solar ejects the same amount of ^{26}Al than a 6.5 $M_\odot$ star at solar

metallicity. The reason is that the overall temperature is controlled by the mass of the CO core, which scales directly with the initial mass and inversely with the initial metallicity (see Sect. 3.4.1). In addition, the lower opacity in lower metallicity stars keeps the structure more compact and hence hotter.

In the models of Super-AGB presented in Fig. 3.12 the 3rd dredge-up is found to be negligible and HBB produces ^{26}Al via proton captures on the ^{25}Mg initially present in the envelope, without the contribution of ^{25}Mg from the intershell. Still, these stars produce a large amount of ^{26}Al since there is a large initial amount of ^{25}Mg in the envelope due to the large envelope mass. The lower Super-AGB ^{26}Al yield at metallicity solar/200 is due to very high HBB temperatures, at which the rate of the ^{26}Al destruction reaction $^{26}\mathrm{Al}(p,\gamma)^{27}\mathrm{Si}$ is significantly enhanced.

The yields predicted for the ^{26}Al from AGB stars presented in Fig. 3.12 are quite uncertain since there are several stellar and nuclear uncertainties. First, there are uncertainties related to the modelling of HBB. In fact, the temperature reached at the base of the convective envelope, which governs the efficiency of the $^{25}\mathrm{Mg}(p,\gamma)^{26}\mathrm{Al}$ reaction, depends on the modeling of the temperature gradient within the convectively unstable region. Hence, different treatments of the convective layers may lead to significantly different efficiencies of the HBB. Second, the uncertainty in the efficiency of the 3rd dredge-up already discussed in Sect. 3.4.1 also affects the ^{26}Al yields: in the low-mass models it affects the dredge-up of ^{26}Al itself, in the massive models it affects the dredge-up of ^{25}Mg, which is then converted into ^{26}Al via HBB. Third, the mass-loss rate is another major uncertain parameter in the modelling of AGB stars. The mass-loss rate determines the stellar lifetime and thus the time available to produce ^{26}Al and the final ^{26}Al yield.

Another model uncertainty is related to the possible occurrence of extra mixing at the base of the convective envelope in the low-mass AGB models that do not experience HBB. Such extra mixing in AGB stars would be qualitatively similar to the extra mixing in red giant stars described in Sect. 3.3.2. In the hypothesis of extra mixing, material travels from the base of the convective envelope inside the radiative region close to the H-burning shell, suffers proton captures, and is taken back up into the convective envelope. If the mixed material dips into the H-burning shell, down to temperatures higher than $\simeq$50 MK, then this mechanism could produce ^{26}Al and contribute to some amount of this nucleus in the low-mass models (Nollett et al. 2003; Palmerini et al. 2011). Unfortunately, from a theoretical point of view, there is no agreement on which mechanism drives the extra mixing and on the features of the mixing. Some constraints on it, however, can be derived from the composition of MS, S, SC, and C stars as well as meteoritic stellar grains, as will be discussed in detail in Sect. 3.6.2.

As for nuclear uncertainties, the rate of the $^{26}\mathrm{Al}(p,\gamma)^{27}\mathrm{Si}$ reaction may be uncertain by three orders of magnitude in the temperature range of interest for AGB stars (Iliadis et al. 2001), with the consequence that ^{26}Al yields from AGB stars suffer from uncertainties of up to two orders of magnitude (Izzard et al. 2007; van Raai et al. 2008). New experiments and approaches to estimate this rate are needed to get a more precise determination of the production of ^{26}Al in AGB stars (see, e.g. Iliadis et al. 2010). The rate of the production reaction $^{26}\mathrm{Mg(p,}\gamma)^{26}\mathrm{Al}$ has been

recently measured underground by LUNA (Laboratory for Underground Nuclear Astrophysics) at the LNGS laboratories in Italy, where the km-thick rock of the Gran Sasso mountain allows for orders-of-magnitude reduction of the background signals with respect to laboratories on the Earth surface. The rate was determined with high accuracy (Straniero et al. 2013). However, the feeding factor to the long-lived ground state of ^{26}Al is still poorly constrained, with different experiments providing a range of values and with relatively large uncertainties.

In spite of all these important uncertainties, current models do indicate that at least some AGB models produce a significant amount of ^{26}Al. These models cover a small range of stellar masses, only those suffering HBB on the AGB phase. When the yields presented in Fig. 3.12 are averaged over a Salpeter initial stellar mass function, the result is that AGB stars globally do not provide an important contribution to the present abundance of ^{26}Al in the Galaxy. This contribution sums up to only 0.24% of the contribution from massive star winds and core-collapse supernovae (Limongi and Chieffi 2006; Lugaro and Karakas 2008). Adding up the contribution of Super-AGB stars only marginally increases the contribution of AGB stars to Galactic ^{26}Al to 0.85% of the contribution coming from the more massive stars (see also Siess and Arnould 2008).

3.6.2 Evidence of ^{26}Al in AGB Stars

It may be possible to determine the abundance of ^{26}Al in AGB stars using molecular lines of Al-bearing molecules. This was carried out by Guelin et al. (1995) for the nearest carbon star, CW Leo, using rotational lines of AlF and AlCl molecules with different Al isotopic composition. One observed line was tentatively attributed to ^{26}AlF, and from its observed strength an upper limit of 0.04 for the ^{26}Al/^{27}Al ratio was inferred. No ^{26}AlCl lines were detected, which led to an upper limit of 0.1. These values cannot be reached by solar metallicity AGB models (Fig. 3.12), however, this detection has not been confirmed so it is doubtful if it can represent a valid model constraint.

The main observational evidence of ^{26}Al in AGB stars comes, instead, from stardust (see Fig. 3.13). Aluminium is one of the main component of most oxide stardust grains recovered to date and the initial amount of ^{26}Al present in each grain can be derived from excesses in its daughter nucleus ^{26}Mg. Magnesium is not a main component in corundum (Al_3O_2) and hibonite ($CaAl_{12}O_{19}$) grains, hence, in this cases, ^{26}Mg excesses are all attributed to ^{26}Al decay. In the case of spinel ($MgAl_2O_4$) grains, instead, Mg is a main component of the mineral and thus the contribution of ^{26}Al to ^{26}Mg needs to be more carefully evaluated by weighing the contribution of the two components. Specifically, there are two atoms of Al per each atom of Mg in spinel, which corresponds to a roughly 25 times higher ratio than in the average solar system material.

The ^{26}Al/^{27}Al ratios are observed to be different in the different populations of oxide and silicate grains (see, e.g., Fig. 8 of Nittler et al. 1997). Population I

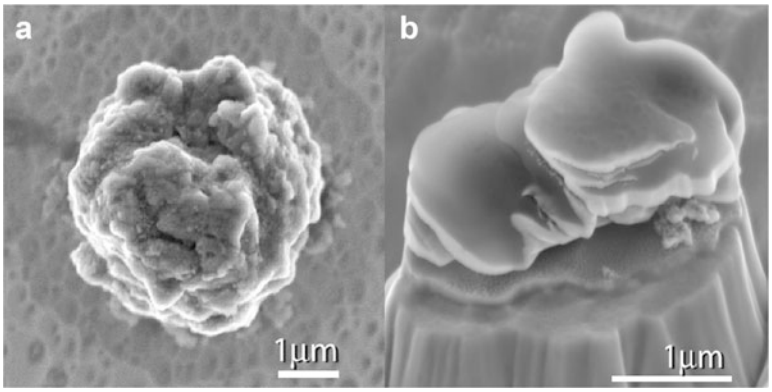

Fig. 3.13 Scanning electron microscope images of dust grains from AGB stars. (**a**) 4-μm-sized silicon carbide (SiC) grain; ubiquitous excesses in ^{26}Mg in such grains indicate prior presence of ^{26}Al. (**b**) 2-μm-sized hibonite ($CaAl_{12}O_{19}$) grain KH15 (Nittler et al. 2008). The grain is sitting on a gold pedestal created by ion-probe sputtering during isotopic analysis. Excesses of ^{26}Mg and ^{41}K indicate that the grain originally condensed with live ^{26}Al and ^{41}Ca

grains cover a wide range of ^{26}Al initial abundance, from no detection to ^{26}Al/^{27}Al $\simeq$0.02. The presence of ^{26}Al might be used to discriminate Population I oxide grains coming from red giant or from AGB stars, since ^{26}Al is expected to be present only in the winds of AGB stars. However, models of the evolution of AGB dust in the Galaxy show that most of these grains originated from AGB stars (Gail et al. 2009). The ^{26}Al/^{27}Al ratios of Population II grains lie at the upper end of the range covered by Population I grains, and reach up to $\simeq$0.1 (see also Fig. 6 of Zinner et al. 2007). This is qualitatively consistent with the strong ^{18}O deficits observed in the Population II grains, since both signatures are produced by H burning. The mysterious Population III show low or no ^{26}Al, which may indicate that these grains did not come from AGB stars. Finally, Population IV grains from supernovae show ^{26}Al/^{27}Al ratios between 0.001 and 0.01 (see Chap. 4).

The ^{26}Al/^{27}Al ratios together with the ^{18}O/^{16}O ratios in Population I and II oxide and silicate grains have provided an interesting puzzle to AGB modellers. Low-mass AGB models do not produce ^{26}Al/^{27}Al ratios high enough and ^{18}O/^{16}O ratios low enough to match the observations. Massive AGB models can produce ^{26}Al/^{27}Al ratios high enough via HBB, however, in this case the ^{18}O/^{16}O ratio is too low ($\sim 10^{-6}$) to match the observations (see Sect. 3.2.1). Grains with ^{18}O/^{16}O $< 10^{-4}$ may have been polluted by solar material during the laboratory analysis, which would have shifted the ^{18}O/^{16}O ratio to higher values with respect to the true ratio of the grain. This argument was invoked to attribute a massive AGB stars origin to a peculiar Population II spinel grain, named OC2 (Lugaro et al. 2007). However, also the ^{17}O/^{16}O ratio presents a problem for this and similar grains because at the temperature of HBB this ratio is always much higher than observed (Boothroyd et al. 1995; Lugaro et al. 2007; Iliadis et al. 2008).

The extra-mixing phenomena mentioned in Sects. 3.3.2 and 3.6.1 have been hypothesized to operate in low-mass AGB stars below the base of the formal convective envelope to explain the composition of Population I and II grains with ^{26}Al/^{27}Al ratios greater than $\simeq 10^{-3}$. This idea has been investigated in detail by Nollett et al. (2003) using a parametric model where the temperature (T_p), determined by the depth at which material is carried, and the mass circulation rate (M_{circ}) in the radiative region between the base of the convective envelope and the H-burning shell are taken as two free and independent parameters. This model was originally proposed to explain observations of AGB stars and grains showing deficits in ^{18}O (Wasserburg et al. 1995). It should be noted, however, that while AGB stars show deficits in their ^{18}O/^{16}O ratios down to roughly 10 times lower than solar, Population II oxide grains show deficits in their ^{18}O/^{16}O ratios down to roughly 100 times lower than solar (see Figs. 5 and 9 of Nittler et al. 1997).

One related problem is the fact that massive AGB stars of mass in the range suffering HBB are predicted to have produced a large fraction of the AGB stardust originally present at the formation of the Sun (Gail et al. 2009). However, if Population II oxide grains originated from low-mass AGB stars instead of massive AGB stars, no stardust grains have ever been recovered with the signature of an origin in massive AGB stars. This conundrum was solved by the recent underground measurement of the ^{17}Op,α)^{14}N reaction rate, which controls the ^{17}O/^{16}O ratio produced by H burning. The experiment was performed by LUNA (the Laboratory for Underground Nuclear Astrophysics) taking advantage of a 15-fold reduction of the experimental background with respect to laboratories overground. The rate was found to be 2 to 2.5 higher (Bruno et al. 2016) than previously reported, which allowed Lugaro et al. (2017) to finally invoke a massive AGB stars origin for at least some of the Population II grains.

In the case of SiC grains, Al is present in the grains as a trace element in relatively large abundance, while Mg is almost absent. Again, this means that ^{26}Mg excesses represent the abundance of ^{26}Al at the time when the grains formed. Mainstream SiC grains from AGB stars were reported to show ^{26}Al/^{27}Al ratios between 10^{-4} and $\simeq\ 2 \times 10^{-3}$. Models of C-rich AGB stars, i.e., the low-mass models in the lower panel of Fig. 3.12, which do not suffer HBB and hence reach C/O>1 in their envelopes, match the observed upper value but did not cover the observed range down to the lower values (Zinner et al. 2007; van Raai et al. 2008). More recent analysis by Groopman et al. (2015) has produced however a more restricted range of ^{26}Al/^{27}Al ratios in mainstream SiC grains roughly between 10^{-2} and 10^{-3}, in better agreement with the models and potentially useful to constraint the reaction rates for the production and destruction of ^{26}Al.

In conclusion, observational constraints of ^{26}Al in AGB stars provide the potential to investigate some of the most uncertain input physics in the modelling of AGB nucleosynthesis: mixing phenomena and reaction rates.

3.6.3 ^{60}Fe

The other famous long-lived radioactive nucleus ^{60}Fe (with a recently revised half life of 2.6 My, Rugel et al. 2009), of interest from the point of view of γ-ray observations, meteoritic stellar grains, and the composition of the early solar system, can be produced in AGB stars (Wasserburg et al. 2006; Lugaro and Karakas 2008) via the neutron-capture chain ^{58}Fe$(n,\gamma)^{59}$Fe$(n,\gamma)^{60}$Fe, where ^{59}Fe is a branching point, and destroyed via the ^{60}Fe$(n,\gamma)^{61}$Fe reaction, whose rate has been measured experimentally by Uberseder et al. (2009). This is the same chain of reactions responsible for the production of this nucleus in massive stars (see Chap. 4). Given that ^{59}Fe is an unstable nucleus with a relatively short half life of 44 days and with a neutron capture cross section $\sigma \simeq 23$ mbarn (Rauscher and Thielemann 2000), neutron densities of at least 10^{10} n/cm^3 are needed for this branching point to open at a level of 20%, allowing production of the long-living ^{60}Fe. If the neutron density is higher than 10^{12} n/cm^3, then 100% of the neutron-capture flux goes through ^{60}Fe.

From the description of the neutron sources in AGB stars (Sect. 3.5.2), it is clear that ^{60}Fe can only be produced in the convective thermal pulses, where the neutron burst released by the ^{22}Ne neutron source can reach the high neutron density required to open the branching point at ^{59}Fe. Hence, the production of ^{60}Fe in AGB stars is almost completely determined by the activation of the ^{22}Ne neutron source. The ^{13}C neutron source may instead destroy some ^{60}Fe in the intershell (Wasserburg et al. 2006).

The AGB yields of ^{60}Fe, and their ratios with the yields of ^{56}Fe, are shown in Fig. 3.14. As the temperature at the base of the convective thermal pulses increases with increasing the stellar mass and decreasing the metallicity, the amount of ^{60}Fe delivered to the interstellar medium increases, reaching up to 10^{-5} M$_\odot$, a value comparable to that delivered by a supernova of $\simeq$20 M$_\odot$ (Limongi and Chieffi 2006). Ratios of the ^{60}Fe and ^{56}Fe abundances at the end of the AGB phase from the AGB neutron-capture models of Wasserburg et al. (2006) also plotted in Fig. 3.14.[12]

As for ^{26}Al, also in the case of ^{60}Fe stellar and nuclear uncertainties affect the results presented in Fig. 3.14 (and different choice in the model inputs are responsible for variations in the results obtained by different authors). First, the overall mass carried to the envelope via the 3rd dredged-up is essential to the determination of the envelope ^{60}Fe abundance in AGB stars. This is because ^{60}Fe is made only via neutron captures in the He-rich intershell and needs to be mixed into the envelope in order to show up at the stellar surface and to be carried to the interstellar medium by the winds. Hence, the ^{60}Fe yield is directly related to the efficiency of the 3rd dredge-up. For example, models experiencing little or no 3rd dredge-up produce a null ^{60}Fe yield. This important point applies to all long-living radioactive nuclei produced in AGB stars, except for the case of ^{26}Al, which is made

[12]Final *abundance* ratios are equivalent to *yield* ratios because the yields reflect the composition at the end of the evolution, since more than half of the mass lost during the entire life of the star leaves the star at the end of the AGB phase in the superwind.

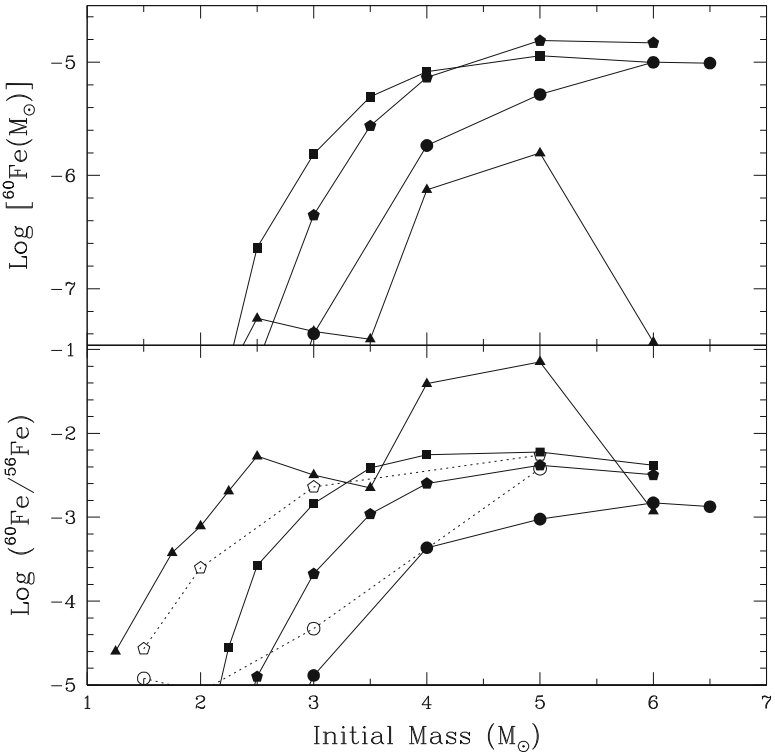

Fig. 3.14 The yields of ^{60}Fe (top panel) from Karakas and Lattanzio (2007) (see caption of Fig. 3.12 for definition of a yield) and the ratio of the yield of ^{60}Fe to the yield of ^{56}Fe (bottom panel) for stellar models of different masses and metallicities (full symbols from Karakas and Lattanzio 2007). The symbols representing the different metallicities are the same as in Fig. 3.12. For comparison, the ratios of the abundances of ^{60}Fe and ^{56}Fe at the end of the AGB evolution computed by Wasserburg et al. (2006) are also shown as open symbols

via HBB directly within the envelope. Second, the mass-loss rate affects the result as it determines the stellar lifetime and thus the number of thermal pulses and 3rd dredge-up episodes.

Nuclear physics inputs that contribute important uncertainties to the production of ^{60}Fe are the rate of the neutron source reaction ^{22}Ne(α,n)^{25}Mg, which determines how many neutrons are produced in the thermal pulses, and the neutron capture cross section of ^{60}Fe itself, which has been experimentally determined directly (Uberseder et al. 2009), and of the branching point isotope ^{59}Fe, which is estimated theoretically (Rauscher and Thielemann 2000) and via indirect measurements (Uberseder et al. 2014), as the short half life of this nucleus hampers direct experimental determinations.

3.6.4 ^{36}Cl and ^{41}Ca

Two more long-lived radioactive nuclei lighter than iron are of special interest because they are observed to be present in the early solar system and can be made by neutron captures in the intershell of AGB stars: ^{36}Cl (with half life of 0.3 Myr) and ^{41}Ca (with half life of 0.1 Myr). Differently from ^{60}Fe, production of these nuclei does not require the activation of branching points, since ^{36}Cl and ^{41}Ca are made by neutron captures on ^{35}Cl and ^{40}Ca, respectively, which are stable nuclei with relatively high solar abundances. Neutron captures also destroy ^{36}Cl and ^{41}Ca via different channels, the predominants being ^{41}Ca$(n, \alpha)^{38}$Ar, with $\sigma \simeq 360$ mbarn and ^{36}Cl$(n, p)^{36}$S, with $\sigma \simeq 118$ mbarn.

Neutrons coming from the ^{22}Ne neutron source are responsible for the production of ^{36}Cl and ^{41}Ca. As there are no branching points involved, this is not due to the high neutron density of this neutron flux, as it is for the production of ^{60}Fe, but to the fact that neutrons released by the ^{22}Ne in the thermal pulse affect the composition of the whole He-rich intershell material, where large initial quantities of the seed nuclei ^{35}Cl and ^{40}Ca are available. On the contrary, neutrons released by the ^{13}C neutron source affect a small fraction of the intershell material, being the ^{13}C-^{14}N pocket roughly 1/10th to 1/20th of the intershell (by mass) in the current models.

In general, to produce neutron-rich isotopes of elements lighter than iron by the *s*-process a small number of neutrons captured by seed nucleus are needed: only one in the cases of ^{36}Cl and ^{41}Ca. Hence, final abundances are determined to a higher level by the availability of seed nuclei, rather than that of free neutrons. For the light nuclei a production flux from the lighter to the heaviest elements does not occur (strictly speaking it is not correct to apply the *s*-process terminology in this case), instead, the nucleosynthetic process is very localized: neutron captures on the sulphur isotopes, for example, do not affect the abundances of the chlorine isotopes and so on. This is because neutron-capture cross section of nuclei lighter than iron are much smaller (by as much as 3 orders of magnitude) than those of typical nuclei heavier than iron. Hence, to produce nuclei heavier than iron by the *s*-process, instead, including the relatively large number of long-living radioactive nuclei lying on the *s*-process path discussed in Sect. 3.6.5, a production flux from the lighter to the heavier elements occurs, where many neutrons are captured by the iron seeds and it is possible to reach up to the heaviest elements. Hence, the number of free neutrons plays a dominant role in this case.

The ^{36}Cl/^{35}Cl and ^{41}Ca/^{40}Ca abundance ratios at the end of the AGB evolution computed by Wasserburg et al. (2006) and by van Raai et al. (2012) (which are based on the same codes and stellar models of Karakas and Lattanzio 2007) are plotted in Fig. 3.15. As in the case of ^{60}Fe, the main model uncertainties affecting these results is the efficiency of the 3rd dredge-up, the mass-loss rate, and the rate of the ^{22}Ne$(\alpha$,n$)^{25}$Mg reaction.

Moreover, while experimental estimates for the neutron-capture cross section of ^{36}Cl and ^{41}Ca are available (e.g. de Smet et al. 2006), a difficult problem is to provide a reliable set of values for the electron-capture rate of ^{41}Ca, in particular as

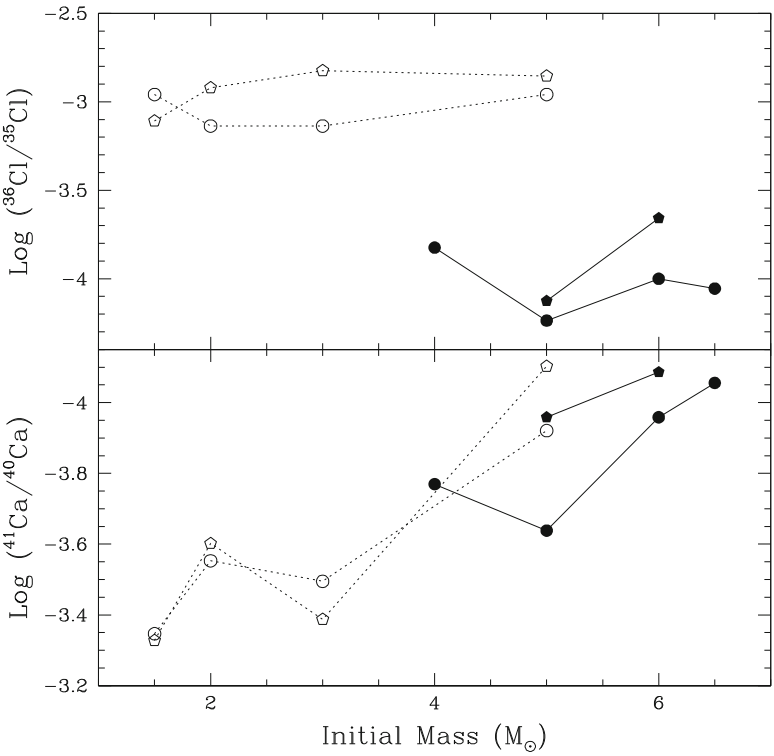

Fig. 3.15 ^{36}Cl/^{35}Cl and ^{41}Ca/^{40}Ca abundance ratios at the end of the AGB evolution computed by Wasserburg et al. (2006) (open symbols) and by van Raai et al. (2012) (full symbols). The symbols representing the different metallicities are the same as in Fig. 3.12

it is expected to vary significantly for different temperatures and densities relevant to stellar conditions (Chap. 9). As most electron captures in the ^{41}Ca atom occurs on electrons belonging to the electron shell closest to the nucleus (the K shell), when the temperature increases to 100 MK and all electrons have escaped the atom leaving the nucleus bare, the half life of ^{41}Ca increases by almost three orders of magnitude. However, if, still at a temperature of 100 MK, the density increases to 10^4 g/cm^3, electrons are forced nearby ^{41}Ca nuclei and the half life decreases back to its terrestrial value. The only set of theoretical data for this reaction are those provided by Fuller et al. (1982). Moreover, the temperature and density dependence of the electron-capture rate of ^{41}Ca has never been properly implemented in AGB stellar models, in particular it has not yet been solved coupled to convective motions, both in the thermal pulses and in the stellar envelope, where material is constantly carried from hotter denser regions to cooler less dense regions and viceversa. Given these considerations, we are far from an accurate determination of the abundance of ^{41}Ca made by AGB stars.

In summary, and in relevance to the early solar system composition of long-lived radioactive nuclei discussed in Chap. 6, AGB stars can produce some of the radioactive nuclei found to be present in the early solar system: ^{26}Al via hot bottom burning and ^{41}Ca and ^{60}Fe via neutron captures in the thermal pulse and the 3rd dredge-up. In certain mixing conditions the abundances of these nuclei can be produced by AGB stars in the same proportions observed in the early solar system (Wasserburg et al. 2006; Trigo-Rodriguez et al. 2009). On the other hand, ^{36}Cl cannot be produced in the observed amount. Uncertainties in the neutron capture cross sections of ^{35}Cl and ^{36}Cl may play a role in this context.

Finally, a characteristic signature of the AGB stars inventory of long-living radioactive nuclei, is that, unlike supernovae (Chap. 4 and Sect. 5.3), AGB stars cannot possibly produce ^{55}Mn, another nucleus of relevance to early solar system composition. This is because ^{55}Mn is a proton-rich nucleus, lying on the proton-rich side of the valley of β-stability, and thus it cannot be made by neutron captures.

3.6.5 Long-Lived Radioactive Isotopes Heavier than Fe

The *s* process in AGB stars produces significant abundances of six long-lived radioactive nuclei heavier than iron: ^{81}Kr, ^{93}Zr, ^{99}Tc, ^{107}Pd, ^{135}Cs, and ^{205}Pb. The survival of ^{135}Cs and ^{205}Pb in stellar environments is however very uncertain and can even be prevented because of the strong and uncertain temperature and density dependence of their half lives, decreasing by orders of magnitudes in stellar conditions and determined only theoretically (as in the case of ^{41}Ca. See detailed discussion by Mowlavi et al. 1998; Wasserburg et al. 2006, and also Appendix B). While ^{93}Zr, ^{99}Tc, ^{107}Pd, and ^{205}Pb are on the main *s*-process path and are produced by neutron captures on the stable isotopes ^{92}Zr, ^{98}Mo,[13] ^{106}Pd, and ^{204}Pb, respectively, ^{81}Kr, ^{181}Hf, and ^{135}Cs are not on the main *s*-process path, but can be reached via the activation of branching points at ^{79}Se and ^{80}Br, ^{134}Cs, and ^{182}Hf, respectively (as described in Appendix B).

Figure 3.16 presents the abundance ratios of long-living radioactive isotopes heavier than iron produced during the *s*-process in AGB stars to one of their nearest stable isotopes calculated by Wasserburg et al. (2006) and by van Raai et al. (2012). For all ratios, except ^{81}Kr/^{82}Kr, the inclusion of the ^{13}C neutron source for models of masses lower than $\simeq$3–4 $M_\odot$, completely changes the results, since the ^{22}Ne source is not significantly activated in these low-mass stellar models. It also makes an important difference in the absolute abundance of the all isotopes involved, with very low production factors with respect to the initial value if the ^{13}C neutron source is not included (see Table 4 of Wasserburg et al. 2006). The case of ^{81}Kr/^{82}Kr is different in that it does not feel the inclusion of the ^{13}C neutron source as much as the other ratios because, even for the low-mass stars, the marginal activation of

[13] Followed by fast decay of ^{99}Mo, with a half life of 66 h.

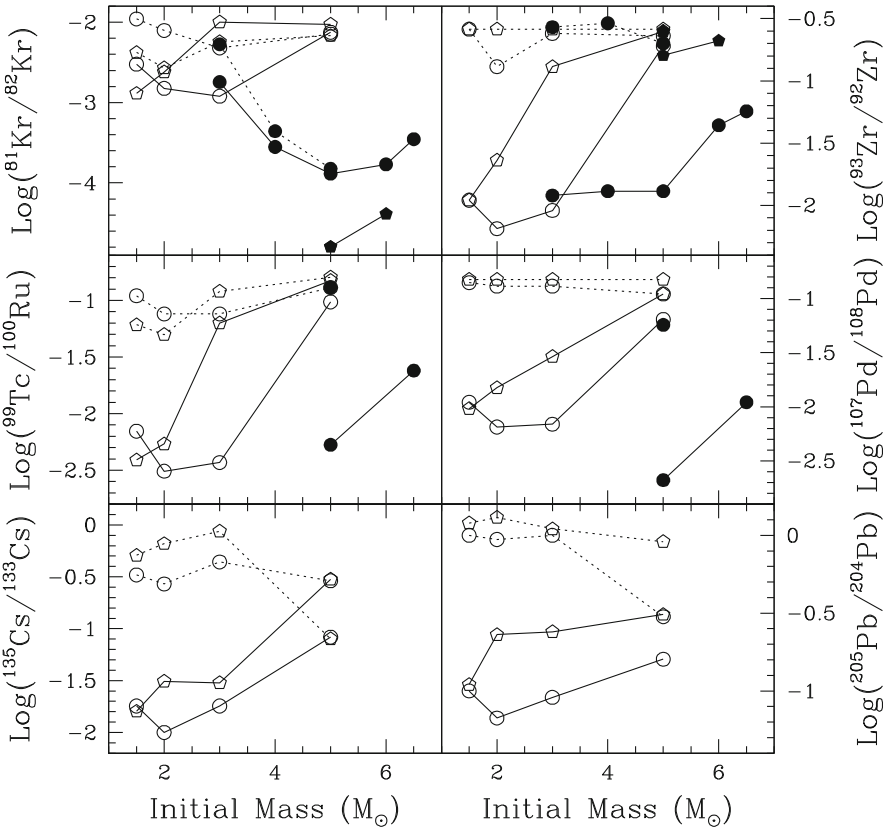

Fig. 3.16 Abundance ratios of long-lived radioactive nuclei heavier than iron, with respect to one of their nearest stable isotope, at the end of the AGB evolution computed by Wasserburg et al. (2006) (open symbols) and by van Raai et al. (2012) (full symbols). The symbols representing the different metallicities are the same as in Fig. 3.12. Symbols connected by the solid line represent models computed without the inclusion of the ^{13}C neutron source, symbols connected by the dotted lines represent models computed with the inclusion of the ^{13}C neutron source

the ^{22}Ne reaction in the latest thermal pulses affects the production of the *s*-process elements up to the first *s*-process peak, including Kr, and of ^{81}Kr in particular via the branching point at ^{79}Se.

For stellar models with initial masses higher than $\simeq$3-4 M$_\odot$, depending on the metallicity, the ^{22}Ne neutron source is mainly responsible for the activation of the *s*-process and thus the production of the heavy long-lived isotopes. Hence, in these models, the inclusion of a ^{13}C neutron source typically does not make a significant difference in the final ratios, except in the case of ^{205}Pb/^{204}Pb. This ratio is different in that it always feels the effect of the inclusion of the ^{13}C neutron source because production of the element Pb, corresponding to the third and last *s*-process peak, is

possible only if very large neutron exposures are available ($\sim$ mbarn^{-1}), which can only be produced by the ^{13}C neutron source.

It is interesting to discuss in detail the results for the 3 $M_\odot$ stellar model of 1/3 solar metallicity, because this model represents an example of the transition between the two regimes of the *s* process in AGB stars: when neutrons are provided by the ^{13}C or by the ^{22}Ne source. In this model the number of free neutrons produced by the ^{22}Ne source is higher than in the solar metallicity model of the same mass partly because the temperature in the thermal pulses is slightly higher, but mostly because there is a smaller number of nuclei present to capture neutrons. Hence, the neutron flux coming from the ^{22}Ne neutron source affects the production of the long-living isotopes up to ^{99}Tc, but not that of the long-living isotopes of higher masses: for ^{107}Pd, ^{133}Cs, and ^{205}Pb, ^{13}C is still the main neutron source.

In addition to the main effect due to the shift from the ^{13}C to the ^{22}N regime with changing the initial mass and metallicity of the star, smaller variations due to the marginal effect of the ^{22}Ne neutron source in the models of low-mass are always visible in the details of the production of the heavy long-living nuclei affected by the operation of the branching points activated in thermal pulses: ^{81}Kr, ^{99}Tc, and ^{135}Cs. For example, restricting our view to the solar metallicity models of mass lower than 4 $M_\odot$ and computed with the inclusion of the ^{13}C neutron source, the ^{81}Kr/^{82}Kr ratio decreases with the stellar mass as ^{81}Kr is progressively skipped by the branching point at ^{79}Se at the higher neutron densities experienced by the higher mass models. The opposite happens for the ^{135}Cs/^{133}Cs ratio, which increases with the stellar mass as the branching point at ^{134}Cs becomes progressively more active.

When considering the effect of branching points on the production of heavy long-living radioactive nuclei by the *s*-process in AGB stars it is worth noting that ^{129}I and ^{182}Hf—two long-lived radioactive isotopes of special interest for the composition of the early solar system—were believed to not be significantly produced in AGB stars. Production of ^{129}I is not possible because the half life of ^{128}I is only 25 min (see Appendix B). Until 2014, only a marginal production of ^{182}Hf, up to ^{182}Hf/^{180}Hf$\simeq$ 10^{-6} (Wasserburg et al. 1994), was believed to be possible via activation of the branching point at ^{181}Hf (see Appendix B). This stemmed from the fact that the half life of ^{181}Hf, the branching point leading to the production of ^{182}Hf, was believed to strongly decrease from the terrestrial value of 42 days to roughly a couple of days in stellar conditions, mostly via population of an excited state at 68 keV (Takahashi and Yokoi 1987). However, the more recent, detailed experiments of Bondarenko et al. (2002) on the nuclear structure of ^{181}Hf demonstrated that this energy level does not exist. This allowed (Lugaro et al. 2014a) to attribute a large production of ^{182}Hf to the *s*-process in AGB stars, with a ^{182}Hf/^{180}Hf of the order of 0.15. This resolved the discrepancy between the abundances of ^{129}I and ^{182}Hf in the early solar system and allowed to time the latest *r*- and *s*-process events that contributed to the build-up of solar system matter to roughly 100 Myr and 10–30 Myr, respectively, before the formation of the Sun.

The main uncertainties affecting both sets of predictions shown in Fig. 3.16 are the detailed features of the proton diffusion leading to the production of the ^{13}C

neutron source. Ratios that depend on the activation of the ^{22}Ne neutron source are also sensitive to the choice of the mass loss rate and of the ^{22}Ne(α,n)^{25}Mg reaction rate. The treatment of branching points is also of importance in the determination of ^{81}Kr and ^{135}Cs. For example, in the case of ^{81}Kr/^{82}Kr, the treatment of the temperature dependence of the decay rate of the branching point nucleus ^{79}Se is fundamental to the final result, as demonstrated by the fact that including the temperature dependence of these decay rate (as carried out by Wasserburg et al. 2006) produce a ^{81}Kr/^{82}Kr ratio two orders of magnitude larger than using the terrestrial value as constant (van Raai et al. 2012).

In summary, due to the *s*-process, AGB stars are a rich source of radioactive elements heavier than Fe.

In fact, the historical observation of Tc in late type giants (Sect. 3.5.2) was confirmed by the presence of ^{99}Tc in single stardust SiC grains at the time of their formation discovered via laboratory analysis of the Ru isotopic composition of these grains (Savina et al. 2004). Since both Tc and Ru are refractory elements, they were included in SiC grains as trace elements during grain formation. To match the observational stardust data both the contribution of ^{99}Ru and ^{99}Tc predicted by AGB stellar models to the total nuclear abundance at mass 99 must be considered. Radiogenic decay of ^{99}Tc occurs in the intershell in the absence of neutron fluxes, in the stellar envelope, and inside the grains. On the other hand, there is no evidence for a contribution of ^{135}Cs to ^{135}Ba when comparing AGB model predictions to laboratory data of the ^{135}Ba/^{136}Ba ratio in single SiC grains (see Fig. 16 of Lugaro et al. 2003a). This is probably because Cs is not as refractory as Ba and thus was not included in the grains at the time of their formation.

3.7 Conclusions

In summary, radioactive nuclei are both the crucial ingredient necessary to understand the physics of low- to intermediate-mass stars, and the product of the nuclear reactions that occur in their interiors. Neutrinos produced by nuclear energy generation in the Sun and observed on the Earth have allowed us both to peek in the internal layers of the Sun and validate the process of H burning in its core, and to realise the complex nature of the neutrinos themselves. During the late phases of the evolution of low- to intermediate-mass stars, off the Main Sequence and into the red giant and asymptotic giant branches, He burning together with H burning dominate the energy generation. The alternating of these two different types of burning, at different times and in different location within the star, results in a complex evolution and the production of a large variety of chemical elements, together with their radioactive isotopes. Mixing between the deep layers of the star where the nuclear reactions take place, and the surface of the star, where we can see these chemical products, is still one of the fundamental modelling uncertainty. The timescale and strength of the mass loss that carries the chemical elements away from

the star, thus enriching the interstellar medium, is another long-standing uncertainty in our modelling of these stars.

In terms of observable radioactivities, H burning at the base of the envelope in relatively massive AGB stars and Super-AGB stars is responsible for the production of the long-lived ^{26}Al. Although the contribution from these stars to the Galactic enrichment of ^{26}Al is relatively small compared to that of massive stars, observational signatures of this nucleosynthesis are recorded in meteoritic stardust grains. The other crucial nucleosynthetic process proven to occur in AGB stars are neutron captures, in the form of the *s* process, producing roughly half of the cosmic abundances of the elements beyond iron. During the *s* process, radioactive nuclei act as branching points on the path of neutron captures, generating a huge diversity of possibilities in the production of the isotopes up to Bi. Implementation of the nuclear properties of these radionuclei (decay rates and neutron-capture cross sections) in nuclear reaction networks, together with stellar modelling, allow us to produce theoretical predictions. These can be compared to observational constraints coming from both spectroscopic observations (for example of Rb) and from laboratory analysis of meteoritic stardust grains (for example of the ^{96}Zr/^{94}Zr ratio) to pinpoint the features of the *s*-process in AGB stars. For example, the Rb/Sr ratios allowed us to realise that the ^{13}C(α,n)^{16}O is the main neutron source, and the ^{96}Zr/^{94}Zr ratio has shed light on the activation of the secondary neutron source ^{22}Ne(α,n)^{25}Mg. Since much of the information on the nuclear properties of radioactive nuclei is available only theoretically, this procedure allows us also to better constrain our understanding of the nuclei themselves. Finally, neutron captures in AGB stars produce many radioactive isotopes with half lives between 0.1 and 20 Myr. These are interesting as the tracer of fresh nucleosynthesis (as in the case of Tc), as well as in relation of their abundances in the early Solar System (see Chap. 6). Most likely AGB stars contributed the ^{107}Pd and ^{182}Hf that we observe to have been present in the early solar system from analysis meteoritic rocks and inclusions and that are used for dating events in the early Solar System related to the formation and evolution of planetesimals and planets.

References

Abdurashitov JN, Bowles TJ, Cherry ML, Cleveland BT, Davis R, Elliott SR, Gavrin VN, Girin SV, Gorbachev VV, Ibragimova TV, Kalikhov AV, Khairnasov NG, Knodel TV, Lande K, Mirmov IN, Nico JS, Shikhin AA, Teasdale WA, Veretenkin EP, Vermul VM, Wark DL, Wildenhain PS, Wilkerson JF, Yants VE, Zatsepin GT (1999) Measurement of the solar neutrino capture rate by SAGE and implications for neutrino oscillations in vacuum. Phys Rev Lett 83:4686–4689. https://doi.org/10.1103/PhysRevLett.83.4686, arXiv:astro-ph/9907131

Abia C, Busso M, Gallino R, Domínguez I, Straniero O, Isern J (2001) The ^{85}Kr s-Process branching and the mass of carbon stars. Astrophys J 559:1117–1134. https://doi.org/10.1086/322383, arXiv:astro-ph/0105486

Abia C, Hedrosa RP, Domínguez I, Straniero O (2017) The puzzle of the CNO isotope ratios in asymptotic giant branch carbon stars. Astron Astrophys 599:A39. https://doi.org/10.1051/0004-6361/201629969, 1611.06400

Amari S, Gao X, Nittler LR, Zinner E, José J, Hernanz M, Lewis RS (2001a) Presolar grains from novae. Astrophys J 551:1065–1072. https://doi.org/10.1086/320235, arXiv:astro-ph/0012465

Amari S, Nittler LR, Zinner E, Gallino R, Lugaro M, Lewis RS (2001b) Presolar SIC grains of type Y: origin from low-metallicity asymptotic giant branch stars. Astrophys J 546:248–266. https://doi.org/10.1086/318230

Amari S, Nittler LR, Zinner E, Lodders K, Lewis RS (2001c) Presolar SiC grains of type A and B: their isotopic compositions and stellar origins. Astrophys J 559:463–483. https://doi.org/10.1086/322397

Aoki W, Honda S, Beers TC, Sneden C (2003a) Measurement of the europium isotope ratio for the extremely metal poor, r-Process-enhanced star CS 31082-001. Astrophys J 586:506–511. https://doi.org/10.1086/367540, arXiv:astro-ph/0211617

Aoki W, Ryan SG, Iwamoto N, Beers TC, Norris JE, Ando H, Kajino T, Mathews GJ, Fujimoto MY (2003b) Europium Isotope Ratios in s-Process Element-enhanced Metal-poor Stars: A New Probe of the ^{151}Sm Branching. Astrophys J 592:L67–L70. https://doi.org/10.1086/377681, arXiv:astro-ph/0306544

Arlandini C, Käppeler F, Wisshak K, Gallino R, Lugaro M, Busso M, Straniero O (1999) Neutron capture in low-mass asymptotic giant branch stars: cross sections and abundance signatures. Astrophys J 525:886–900. https://doi.org/10.1086/307938, arXiv:astro-ph/9906266

Arpesella C, Back HO, Balata M, Bellini G, Benziger J, Bonetti S, Brigatti A, Caccianiga B, Cadonati L, Calaprice F, Carraro C, Cecchet G, Chavarria A, Chen M, Dalnoki-Veress F, D'Angelo D, de Bari A, de Bellefon A, de Kerret H, Derbin A, Deutsch M, di Credico A, di Pietro G, Eisenstein R, Elisei F, Etenko A, Fernholz R, Fomenko K, Ford R, Franco D, Freudiger B, Galbiati C, Gatti F, Gazzana S, Giammarchi M, Giugni D, Goeger-Neff M, Goldbrunner T, Goretti A, Grieb C, Hagner C, Hampel W, Harding E, Hardy S, Hartman FX, Hertrich T, Heusser G, Ianni A, Ianni A, Joyce M, Kiko J, Kirsten T, Kobychev V, Korga G, Korschinek G, Kryn D, Lagomarsino V, Lamarche P, Laubenstein M, Lendvai C, Leung M, Lewke T, Litvinovich E, Loer B, Lombardi P, Ludhova L, Machulin I, Malvezzi S, Manecki S, Maneira J, Maneschg W, Manno I, Manuzio D, Manuzio G, Martemianov A, Masetti F, Mazzucato U, McCarty K, McKinsey D, Meindl Q, Meroni E, Miramonti L, Misiaszek M, Montanari D, Monzani ME, Muratova V, Musico P, Neder H, Nelson A, Niedermeier L, Oberauer L, Obolensky M, Orsini M, Ortica F, Pallavicini M, Papp L, Parmeggiano S, Perasso L, Pocar A, Raghavan RS, Ranucci G, Rau W, Razeto A, Resconi E, Risso P, Romani A, Rountree D, Sabelnikov A, Saldanha R, Salvo C, Schimizzi D, Schönert S, Shutt T, Simgen H, Skorokhvatov M, Smirnov O, Sonnenschein A, Sotnikov A, Sukhotin S, Suvorov Y, Tartaglia R, Testera G, Vignaud D, Vitale S, Vogelaar RB, von Feilitzsch F, von Hentig R, von Hentig T, Wojcik M, Wurm M, Zaimidoroga O, Zavatarelli S, Zuzel G (2008) Direct measurement of the Be7 solar neutrino flux with 192 days of borexino data. Phys Rev Lett 101(9):091302. https://doi.org/10.1103/PhysRevLett.101.091302, 0805.3843

Aschwanden MJ (2008) Solar flare physics enlivened by TRACE and RHESSI. J Astrophys Astron 29:115–124. https://doi.org/10.1007/s12036-008-0015-0

Asplund M, Grevesse N, Sauval AJ, Scott P (2009) The chemical composition of the sun. Annu Rev Astron Astrophys 47:481–522. https://doi.org/10.1146/annurev.astro.46.060407.145222, 0909.0948

Ávila JN, Lugaro M, Ireland TR, Gyngard F, Zinner E, Cristallo S, Holden P, Buntain J, Amari S, Karakas A (2012) Tungsten isotopic compositions in stardust SiC grains from the murchison meteorite: constraints on the s-process in the Hf-Ta-W-Re-Os Region. Astrophys J 744:49. https://doi.org/10.1088/0004-637X/744/1/49, 1110.4763

Ávila JN, Ireland TR, Lugaro M, Gyngard F, Zinner E, Cristallo S, Holden P, Rauscher T (2013) Europium s-process signature at close-to-solar Metallicity in stardust SiC grains from asymptotic giant branch stars. Astrophys J 768:L18. https://doi.org/10.1088/2041-8205/768/1/L18, 1303.5932

Bahcall JN, Cleveland BT, Davis R Jr, Rowley JK (1985) Chlorine and gallium solar neutrino experiments. Astrophys J 292:L79–L82. https://doi.org/10.1086/184477

Balachandran SC (2005) Anomalous abundances in red giants: the Li-Rich stars. In: Barnes TG III, Bash FN (eds) Cosmic abundances as records of stellar evolution and nucleosynthesis, Astronomical society of the pacific conference series, vol 336, p 113

Bellini G, Benziger J, Bonetti S, Buizza Avanzini M, Caccianiga B, Cadonati L, Calaprice F, Carraro C, Chavarria A, Chepurnov A, Dalnoki-Veress F, D'Angelo D, Davini S, de Kerret H, Derbin A, Etenko A, Fomenko K, Franco D, Galbiati C, Gazzana S, Ghiano C, Giammarchi M, Goeger-Neff M, Goretti A, Guardincerri E, Hardy S, Ianni A, Ianni A, Joyce M, Korga G, Kryn D, Laubenstein M, Leung M, Lewke T, Litvinovich E, Loer B, Lombardi P, Ludhova L, Machulin I, Manecki S, Maneschg W, Manuzio G, Meindl Q, Meroni E, Miramonti L, Misiaszek M, Montanari D, Muratova V, Oberauer L, Obolensky M, Ortica F, Pallavicini M, Papp L, Perasso L, Perasso S, Pocar A, Raghavan RS, Ranucci G, Razeto A, Re A, Risso P, Romani A, Rountree D, Sabelnikov A, Saldanha R, Salvo C, Schönert S, Simgen H, Skorokhvatov M, Smirnov O, Sotnikov A, Sukhotin S, Suvorov Y, Tartaglia R, Testera G, Vignaud D, Vogelaar RB, von Feilitzsch F, Winter J, Wojcik M, Wright A, Wurm M, Xu J, Zaimidoroga O, Zavatarelli S, Zuzel G, Borexino Collaboration (2010) Measurement of the solar B8 neutrino rate with a liquid scintillator target and 3 MeV energy threshold in the Borexino detector. Phys Rev D 82(3):033006. https://doi.org/10.1103/PhysRevD.82.033006, 0808.2868

Bond H, Sion E, Murdin P (2000) CH stars and barium stars. https://doi.org/10.1888/0333750888/5413

Bondarenko V, Berzins J, Prokofjevs P, Simonova L, von Egidy T, Honzátko J, Tomandl I, Alexa P, Wirth HF, Köster U, Eisermann Y, Metz A, Graw G, Hertenberger R, Rubacek L (2002) Interplay of quasiparticle and phonon excitations in ^{181}Hf. Nucl Phys A 709:3–59. https://doi.org/10.1016/S0375-9474(02)00646-2

Boothroyd AI, Sackmann IJ, Wasserburg GJ (1995) Hot bottom burning in asymptotic giant branch stars and its effect on oxygen isotopic abundances. Astrophys J 442:L21–L24. https://doi.org/10.1086/187806

BOREXINO Collaboration, Bellini G, Benziger J, Bick D, Bonfini G, Bravo D, Caccianiga B, Cadonati L, Calaprice F, Caminata A, Cavalcante P, Chavarria A, Chepurnov A, D'Angelo D, Davini S, Derbin A, Empl A, Etenko A, Fomenko K, Franco D, Gabriele F, Galbiati C, Gazzana S, Ghiano C, Giammarchi M, Göger-Neff M, Goretti A, Gromov M, Hagner C, Hungerford E, Ianni A, Ianni A, Kobychev V, Korablev D, Korga G, Kryn D, Laubenstein M, Lehnert B, Lewke T, Litvinovich E, Lombardi F, Lombardi P, Ludhova L, Lukyanchenko G, Machulin I, Manecki S, Maneschg W, Marcocci S, Meindl Q, Meroni E, Meyer M, Miramonti L, Misiaszek M, Montuschi M, Mosteiro P, Muratova V, Oberauer L, Obolensky M, Ortica F, Otis K, Pallavicini M, Papp L, Perasso L, Pocar A, Ranucci G, Razeto A, Re A, Romani A, Rossi N, Saldanha R, Salvo C, Schönert S, Simgen H, Skorokhvatov M, Smirnov O, Sotnikov A, Sukhotin S, Suvorov Y, Tartaglia R, Testera G, Vignaud D, Vogelaar RB, von Feilitzsch F, Wang H, Winter J, Wojcik M, Wright A, Wurm M, Zaimidoroga O, Zavatarelli S, Zuber K, Zuzel G (2014) Neutrinos from the primary proton-proton fusion process in the Sun. Nature 512:383–386. https://doi.org/10.1038/nature13702

Brandon AD, Humayun M, Puchtel IS, Leya I, Zolensky M (2005) Osmium isotope evidence for an s-Process carrier in primitive chondrites. Science 309:1233–1236. https://doi.org/10.1126/science.1115053

Bruno CG, Scott DA, Aliotta M, Formicola A, Best A, Boeltzig A, Bemmerer D, Broggini C, Caciolli A, Cavanna F, Ciani GF, Corvisiero P, Davinson T, Depalo R, Di Leva A, Elekes Z, Ferraro F, Fülöp Z, Gervino G, Guglielmetti A, Gustavino C, Gyürky G, Imbriani G, Junker M, Menegazzo R, Mossa V, Pantaleo FR, Piatti D, Prati P, Somorjai E, Straniero O, Strieder F, Szücs T, Takács MP, Trezzi D, LUNA Collaboration (2016) Improved direct measurement of the 64.5 keV resonance strength in the ^{17}O (p,α)^{14}N reaction at LUNA. Phys Rev Lett 117(14):142502. https://doi.org/10.1103/PhysRevLett.117.142502, 1610.00483

Cameron AGW, Fowler WA (1971) Lithium and the s-PROCESS in red-giant stars. Astrophys J 164:111. https://doi.org/10.1086/150821

Campbell SW, Lattanzio JC (2008) Evolution and nucleosynthesis of extremely metal-poor and metal-free low- and intermediate-mass stars. I. Stellar yield tables and the CEMPs. Astron Astrophys 490:769–776. https://doi.org/10.1051/0004-6361:200809597, 0901.0799

Castilho BV, Gregorio-Hetem J, Spite F, Barbuy B, Spite M (2000) Detailed analysis of a sample of Li-rich giants. Astron Astrophys 364:674–682

Chupp EL (1971) Gamma ray and neutron emissions from the sun. Space Sci Rev 12:486–525. https://doi.org/10.1007/BF00171976

Clayton DD (1968) Principles of stellar evolution and nucleosynthesis

Clayton DD, Nittler LR (2004) Astrophysics with presolar stardust. Annu Rev Astron Astrophys 42:39–78. https://doi.org/10.1146/annurev.astro.42.053102.134022

Cleveland BT, Daily T, Davis RJ, Distel JR, Lande K, Lee CK, Wildenhain PS, Ullman J (1998) Measurement of the solar electron neutrino flux with the homestake chlorine detector. Astrophys J 496:505. https://doi.org/10.1086/305343

Cosner K, Iben I Jr, Truran JW (1980) The effects of unthermalized isomeric states and of a time-varying neutron flux on s-process branching ratios. Astrophys J 238:L91–L96. https://doi.org/10.1086/183265

Côté B, Fryer CL, Belczynski K, Korobkin O, Chruślińska M, Vassh N, Mumpower MR, Lippuner J, Sprouse TM, Surman R, Wollaeger R (2017) The origin of r-Process elements in the Milky Way. ArXiv e-prints 1710.05875

Cowan JJ, Rose WK (1977) Production of C-14 and neutrons in red giants. Astrophys J 212:149–158. https://doi.org/10.1086/155030

Cox JP, Giuli RT (1968) Principles of stellar structure. Gordon and Breach Science Publishers, New York

Cristallo S, Straniero O, Gallino R, Piersanti L, Domínguez I, Lederer MT (2009) Evolution, nucleosynthesis, and yields of low-mass asymptotic giant branch stars at different metallicities. Astrophys J 696:797–820. https://doi.org/10.1088/0004-637X/696/1/797

Cristallo S, Piersanti L, Straniero O (2016) The FRUITY database on AGB stars: past, present and future. J Phys Conf Ser 665:012019. https://doi.org/10.1088/1742-6596/665/1/012019, 1405.3392

Dardelet L, Ritter C, Prado P, Heringer E, Higgs C, Jones S, Denissenkov P, Venn K, Bertolli M, Pignatari M, Woodward P, Herwig F (2014) *i* process and CEMP-*s*/*r* stars. In: Nuclei in the Cosmos (NIC XIII), p PoS(NIC XIII)145, 1505.05500

Dauphas N, Schauble EA (2016) Mass fractionation laws, mass-independent effects, and isotopic anomalies. Annu Rev Earth Planet Sci 44:709–783. https://doi.org/10.1146/annurev-earth-060115-012157

de Smet L, Wagemans C, Heyse J, Vermote S, Van Gils J (2006) Experimental determination of the ^{41}Ca$(n,\alpha)^{38}$Ar reaction cross section. In: Ninth international symposium on nuclei in the Cosmos, Proceedings of science, PoS(NIC-IX)085

Dell'Agli F, García-Hernández DA, Schneider R, Ventura P, La Franca F, Valiante R, Marini E, Di Criscienzo M (2017) Asymptotic giant branch and super-asymptotic giant branch stars: modelling dust production at solar metallicity. Mon Not R Astron Soc 467:4431–4440. https://doi.org/10.1093/mnras/stx387, 1702.03904

Denissenkov PA, Tout CA (2003) Partial mixing and formation of the ^{13}C pocket by internal gravity waves in asymptotic giant branch stars. Mon Not R Astron Soc 340:722–732. https://doi.org/10.1046/j.1365-8711.2003.06284.x

Denissenkov PA, Herwig F, Battino U, Ritter C, Pignatari M, Jones S, Paxton B (2017) I-process nucleosynthesis and mass retention efficiency in he-shell flash evolution of rapidly accreting white dwarfs. Astrophys J 834:L10. https://doi.org/10.3847/2041-8213/834/2/L10, 1610.08541

Dennis BR, Hudson HS, Krucker S (2007) Review of selected RHESSI solar results. In: Klein KL, MacKinnon AL (eds) Lecture Notes in Physics, vol 725. Springer, Berlin, p 33

Despain KH (1980) A difficulty with Ne-22 as the neutron source for the solar system s-process. Astrophys J 236:L165–L168. https://doi.org/10.1086/183219

Doherty CL, Gil-Pons P, Siess L, Lattanzio JC (2017) Super-AGB stars and their role as electron capture supernova progenitors. Publ Astron Soc Aust 34:e056. https://doi.org/10.1017/pasa.2017.52, 1703.06895

Dorfi EA, Höfner S, Feuchtinger MU (2001) Pulsation and mass loss. Kluwer Academic Publisher, Dordrecht, pp 137–154

Dupree AK (1986) Mass loss from cool stars. Annu Rev Astron Astrophys 24:377–420. https://doi.org/10.1146/annurev.aa.24.090186.002113

Ferrarotti AS, Gail HP (2002) Mineral formation in stellar winds. III. Dust formation in S stars. Astron Astrophys 382:256–281. https://doi.org/10.1051/0004-6361:20011580

Ferrarotti AS, Gail HP (2006) Composition and quantities of dust produced by AGB-stars and returned to the interstellar medium. Astron Astrophys 447:553–576. https://doi.org/10.1051/0004-6361:20041198

Fleischer AJ, Gauger A, Sedlmayr E (1992) Circumstellar dust shells around long-period variables. I - Dynamical models of C-stars including dust formation, growth and evaporation. Astron Astrophys 266:321–339

Frogel JA, Mould J, Blanco VM (1990) The asymptotic giant branch of magellanic cloud clusters. Astrophys J 352:96–122. https://doi.org/10.1086/168518

Fuller GM, Fowler WA, Newman MJ (1982) Stellar weak interaction rates for intermediate mass nuclei. III - Rate tables for the free nucleons and nuclei with A= 21 to A = 60. Astrophys J Suppl 48:279–319. https://doi.org/10.1086/190779

Gail HP, Sedlmayr E (1999) Mineral formation in stellar winds. I. Condensation sequence of silicate and iron grains in stationary oxygen rich outflows. Astron Astrophys 347:594–616

Gail HP, Zhukovska SV, Hoppe P, Trieloff M (2009) Stardust from asymptotic giant branch stars. Astrophys J 698:1136–1154. https://doi.org/10.1088/0004-637X/698/2/1136

Gallino R, Arlandini C, Busso M, Lugaro M, Travaglio C, Straniero O, Chieffi A, Limongi M (1998) Evolution and nucleosynthesis in low-mass asymptotic giant branch stars. II. Neutron capture and the s-Process. Astrophys J 497:388. https://doi.org/10.1086/305437

García-Hernández DA, García-Lario P, Plez B, D'Antona F, Manchado A, Trigo-Rodríguez JM (2006) Rubidium-rich asymptotic giant branch stars. Science 314:1751. https://doi.org/10.1126/science.1133706, arXiv:astro-ph/0611319

García-Hernández DA, García-Lario P, Plez B, Manchado A, D'Antona F, Lub J, Habing H (2007) Lithium and zirconium abundances in massive Galactic O-rich AGB stars. Astron Astrophys 462:711–730. https://doi.org/10.1051/0004-6361:20065785, arXiv:astro-ph/0609106

Goriely S, Mowlavi N (2000) Neutron-capture nucleosynthesis in AGB stars. Astron Astrophys 362:599–614

Grevesse N, Sauval AJ (1998) Standard solar composition. Space Sci Rev 85:161–174. https://doi.org/10.1023/A:1005161325181

Gribov V, Pontecorvo B (1969) Neutrino astronomy and lepton charge. Physics Letters B 28:493–496. https://doi.org/10.1016/0370-2693(69)90525-5

Groopman E, Zinner E, Amari S, Gyngard F, Hoppe P, Jadhav M, Lin Y, Xu Y, Marhas K, Nittler LR (2015) Inferred initial $^{26}Al/^{27}Al$ ratios in presolar stardust grains from supernovae are higher than previously estimated. Astrophys J 809:31. https://doi.org/10.1088/0004-637X/809/1/31

Guelin M, Forestini M, Valiron P, Ziurys LM, Anderson MA, Cernicharo J, Kahane C (1995) Nucleosynthesis in AGB stars: observation of Mg-25 and Mg-26 in IRC+10216 and possible detection of Al-26. Astron Astrophys 297:183–196

Hampel W, Heusser G, Kiko J, Kirsten T, Laubenstein M, Pernicka E, Rau W, Roenn U, Schlosser C, Wojcik M, von Ammon R, Ebert KH, Fritsch T, Heidt D, Henrich E, Stieglitz L, Weirich F, Balata M, Hartmann FX, Sann M, Bellotti E, Cattadori C, Cremonesi O, Ferrari N, Fiorini E, Zanotti L, Altmann M, von Feilitzsch F, Moessbauer R, Berthomieu G, Schatzman E, Carmi I, Dostrovsky I, Bacci C, Belli P, Bernabei R, D'Angelo S, Paoluzi L, Bevilacqua A, Cribier M, Gosset L, Rich J, Spiro M, Tao C, Vignaud D, Boger J, Hahn RL, Rowley JK, Stoenner RW, Weneser J (1998) Final results of the ^{51}Cr neutrino source experiments in GALLEX. Phys Lett B 420:114–126

Hampel M, Stancliffe RJ, Lugaro M, Meyer BS (2016) The intermediate neutron-capture process and carbon-enhanced metal-poor stars. Astrophys J 831:171. https://doi.org/10.3847/0004-637X/831/2/171, 1608.08634

Harris MJ, Lambert DL, Hinkle KH, Gustafsson B, Eriksson K (1987) Oxygen isotopic abundances in evolved stars. III - 26 carbon stars. Astrophys J 316:294–304. https://doi.org/10.1086/165201

Heck PR, Marhas KK, Hoppe P, Gallino R, Baur H, Wieler R (2007) Presolar He and Ne isotopes in single circumstellar SiC grains. Astrophys J 656:1208–1222. https://doi.org/10.1086/510478

Heck PR, Amari S, Hoppe P, Baur H, Lewis RS, Wieler R (2009) Ne isotopes in individual presolar graphite grains from the murchison meteorite together with He, C, O, Mg-Al isotopic analyses as tracers of their origins. Astrophys J 701:1415–1425. https://doi.org/10.1088/0004-637X/701/2/1415

Herwig F (2005) Evolution of asymptotic giant branch stars. Annu Rev Astron Astrophys 43:435–479. https://doi.org/10.1146/annurev.astro.43.072103.150600

Herwig F, Bloecker T, Schoenberner D, El Eid M (1997) Stellar evolution of low and intermediate-mass stars. IV. Hydrodynamically-based overshoot and nucleosynthesis in AGB stars. Astron Astrophys 324:L81–L84. arXiv:astro-ph/9706122

Herwig F, Blöcker T, Langer N, Driebe T (1999) On the formation of hydrogen-deficient post-AGB stars. Astron Astrophys 349:L5–L8. arXiv:astro-ph/9908108

Herwig F, Pignatari M, Woodward PR, Porter DH, Rockefeller G, Fryer CL, Bennett M, Hirschi R (2011) Convective-reactive proton-^{12}C combustion in Sakurai's object (V4334 Sagittarii) and implications for the evolution and yields from the first generations of stars. Astrophys J 727:89. https://doi.org/10.1088/0004-637X/727/2/89, 1002.2241

Hinkle KH, Lebzelter T, Straniero O (2016) Carbon and oxygen isotopic ratios for nearby miras. Astrophys J 825:38. https://doi.org/10.3847/0004-637X/825/1/38, 1606.08478

Hoffman RD, Müller B, Janka H (2008) Nucleosynthesis in O-Ne-Mg supernovae. Astrophys J 676:L127–L130. https://doi.org/10.1086/587621, 0712.4257

Höfner S, Olofsson H (2018) Mass loss of stars on the asymptotic giant branch. Mechanisms, models and measurements. Astron Astrophys Rev 26:1. https://doi.org/10.1007/s00159-017-0106-5

Hoppe P, Ott U (1997) Mainstream silicon carbide grains from meteorites. In: Bernatowicz TJ, Zinner E (eds) American Institute of Physics conference series, vol 402, pp 27–58. https://doi.org/10.1063/1.53314

Hoppe P, Annen P, Strebel R, Eberhardt P, Gallino R, Lugaro M, Amari S, Lewis RS (1997) Meteoritic silicon carbide grains with unusual Si isotopic compositions: evidence for an origin in low-mass, Low-metallicity asymptotic giant branch stars. Astrophys J 487:L101. https://doi.org/10.1086/310869

Humayun M, Brandon AD (2007) s-Process implications from osmium isotope anomalies in chondrites. Astrophys J 664:L59–L62. https://doi.org/10.1086/520636

Iben I Jr (1975) Thermal pulses; p-capture, alpha-capture, s-process nucleosynthesis; and convective mixing in a star of intermediate mass. Astrophys J 196:525–547. https://doi.org/10.1086/153433

Iben I Jr, Renzini A (1982) On the formation of carbon star characteristics and the production of neutron-rich isotopes in asymptotic giant branch stars of small core mass. Astrophys J 263:L23–L27. https://doi.org/10.1086/183916

Iben I Jr, Renzini A (1983) Asymptotic giant branch evolution and beyond. Annu Rev Astron Astrophys 21:271–342. https://doi.org/10.1146/annurev.aa.21.090183.001415

Iben I Jr, Truran JW (1978) On the surface composition of thermally pulsing stars of high luminosity and on the contribution of such stars to the element enrichment of the interstellar medium. Astrophys J 220:980–995. https://doi.org/10.1086/155986

Iliadis C, D'Auria JM, Starrfield S, Thompson WJ, Wiescher M (2001) Proton-induced thermonuclear reaction rates for A=20-40 nuclei. Astrophys J Suppl 134:151–171. https://doi.org/10.1086/320364

Iliadis C, Angulo C, Descouvemont P, Lugaro M, Mohr P (2008) New reaction rate for O16(p,γ)F17 and its influence on the oxygen isotopic ratios in massive AGB stars. Phys Rev C 77(4):045802. https://doi.org/10.1103/PhysRevC.77.045802, 0803.2757

Iliadis C, Longland R, Champagne AE, Coc A, Fitzgerald R (2010) Charged-particle thermonuclear reaction rates: II. Tables and graphs of reaction rates and probability density functions. Nucl Phys A 841:31–250. https://doi.org/10.1016/j.nuclphysa.2010.04.009, 1004.4517

Itoh N, Adachi T, Nakagawa M, Kohyama Y, Munakata H (1989) Neutrino energy loss in stellar interiors. III - Pair, photo-, plasma, and bremsstrahlung processes. Astrophys J 339:354–364. https://doi.org/10.1086/167301

Izzard RG, Lugaro M, Karakas AI, Iliadis C, van Raai M (2007) Reaction rate uncertainties and the operation of the NeNa and MgAl chains during HBB in intermediate-mass AGB stars. Astron Astrophys 466:641–648. https://doi.org/10.1051/0004-6361:20066903, arXiv:astro-ph/0703078

Jones S, Ritter C, Herwig F, Fryer C, Pignatari M, Bertolli MG, Paxton B (2016) H ingestion into He-burning convection zones in super-AGB stellar models as a potential site for intermediate neutron-density nucleosynthesis. Mon Not R Astron Soc 455:3848–3863. https://doi.org/10.1093/mnras/stv2488, 1510.07417

Jonsell K, Barklem PS, Gustafsson B, Christlieb N, Hill V, Beers TC, Holmberg J (2006) The Hamburg/ESO R-process enhanced star survey (HERES). III. HE 0338-3945 and the formation of the r + s stars. Astron Astrophys 451:651–670. https://doi.org/10.1051/0004-6361:20054470. arXiv:astro-ph/0601476

Jorissen A, Van Eck S, Mayor M, Udry S (1998) Insights into the formation of barium and Tc-poor S stars from an extended sample of orbital elements. Astron Astrophys 332:877–903. arXiv:astro-ph/9801272

Kaeppeler F, Beer H, Wisshak K, Clayton DD, Macklin RL, Ward RA (1982) S-process studies in the light of new experimental cross sections - distribution of neutron fluences and r-process residuals. Astrophys J 257:821–846. https://doi.org/10.1086/160033

Karakas A, Lattanzio JC (2007) Stellar models and yields of asymptotic giant branch stars. Publ Astron Soc Aust 24:103–117. https://doi.org/10.1071/AS07021, 0708.4385

Karakas AI, Lattanzio JC (2014) The dawes review 2: nucleosynthesis and stellar yields of low- and intermediate-mass single stars. Publ Astron Soc Aust 31:e030. https://doi.org/10.1017/pasa.2014.21, 1405.0062

Karakas AI, Lugaro M (2016) Stellar yields from metal-rich asymptotic giant branch models. Astrophys J 825:26. https://doi.org/10.3847/0004-637X/825/1/26, 1604.02178

Kozlovsky B, Murphy RJ, Ramaty R (2002) Nuclear deexcitation gamma-ray lines from accelerated particle interactions. Astrophys J Suppl 141:523–541. https://doi.org/10.1086/340545

Lambert DL, Smith VV, Busso M, Gallino R, Straniero O (1995) The chemical composition of red giants. IV. The neutron density at the s-Process site. Astrophys J 450:302. https://doi.org/10.1086/176141

Langer N, Heger A, Wellstein S, Herwig F (1999) Mixing and nucleosynthesis in rotating TP-AGB stars. Astron Astrophys 346:L37–L40. arXiv:astro-ph/9904257

Lattanzio JC, Wood PR (2004) Evolution, Nucleosynthesis and pulsation of AGB stars. In: Habing HJ, Olofsson H (eds) Asymptotic giant branch stars, astronomy and astrophysics library, vol 145. Springer, Berlin, p 23

Lewis RS, Amari S, Anders E (1994) Interstellar grains in meteorites: II. SiC and its noble gases. Geochim Cosmochim Acta 58:471–494. https://doi.org/10.1016/0016-7037(94)90478-2

Limongi M, Chieffi A (2006) The nucleosynthesis of ^{26}Al and ^{60}Fe in solar metallicity stars extending in mass from 11 to 120 solar masses: the hydrostatic and explosive contributions. Astrophys J 647:483–500. https://doi.org/10.1086/505164

Liu N, Gallino R, Bisterzo S, Davis AM, Savina MR, Pellin MJ (2014a) The ^{13}C-pocket structure in AGB models: constraints from zirconium isotope abundances in single mainstream SiC grains. Astrophys J 788:163. https://doi.org/10.1088/0004-637X/788/2/163, 1405.1441

Liu N, Savina MR, Davis AM, Gallino R, Straniero O, Gyngard F, Pellin MJ, Willingham DG, Dauphas N, Pignatari M, Bisterzo S, Cristallo S, Herwig F (2014b) Barium isotopic composition of mainstream silicon carbides from murchison: constraints for s-process nucleosynthesis in asymptotic giant branch stars. Astrophys J 786:66. https://doi.org/10.1088/0004-637X/786/1/66, 1403.4336

Liu N, Savina MR, Gallino R, Davis AM, Bisterzo S, Gyngard F, Käppeler F, Cristallo S, Dauphas N, Pellin MJ, Dillmann I (2015) Correlated strontium and barium isotopic compositions of acid-cleaned single mainstream silicon carbides from murchison. Astrophys J 803:12. https://doi.org/10.1088/0004-637X/803/1/12, 1501.05883

Lodders K, Fegley B Jr (1993) Chemistry in circumstellar envelopes of carbon stars: the influence of P, T, and elemental abundances. Meteoritics 28:387

Lucatello S, Tsangarides S, Beers TC, Carretta E, Gratton RG, Ryan SG (2005) The binary frequency among carbon-enhanced, s-Process-rich, metal-poor stars. Astrophys J 625:825–832. https://doi.org/10.1086/428104, arXiv:astro-ph/0412422

Lugaro M (2005) Stardust from meteorites. An introduction to presolar grains. World Scientific Publishing, Singapore

Lugaro M, Karakas AI (2008) ^{26}Al and ^{60}Fe yields from AGB stars. New Astron Rev 52:416–418. https://doi.org/10.1016/j.newar.2008.05.005

Lugaro M, Davis AM, Gallino R, Pellin MJ, Straniero O, Käppeler F (2003a) Isotopic compositions of strontium, zirconium, molybdenum, and barium in single presolar SiC grains and asymptotic giant branch stars. Astrophys J 593:486–508. https://doi.org/10.1086/376442

Lugaro M, Herwig F, Lattanzio JC, Gallino R, Straniero O (2003b) s-Process nucleosynthesis in asymptotic giant branch stars: a test for stellar evolution. Astrophys J 586:1305–1319. https://doi.org/10.1086/367887, arXiv:astro-ph/0212364

Lugaro M, Karakas AI, Nittler LR, Alexander CMO, Hoppe P, Iliadis C, Lattanzio JC (2007) On the asymptotic giant branch star origin of peculiar spinel grain OC2. Astron Astrophys 461:657–664. https://doi.org/10.1051/0004-6361:20065768, arXiv:astro-ph/0610464

Lugaro M, Doherty CL, Karakas AI, Maddison ST, Liffman K, García-Hernández DA, Siess L, Lattanzio JC (2012) Short-lived radioactivity in the early solar system: the Super-AGB star hypothesis. Meteorit Planet Sci 47:1998–2012. https://doi.org/10.1111/j.1945-5100.2012.01411.x, 1208.5816

Lugaro M, Heger A, Osrin D, Goriely S, Zuber K, Karakas AI, Gibson BK, Doherty CL, Lattanzio JC, Ott U (2014a) Stellar origin of the ^{182}Hf cosmochronometer and the presolar history of solar system matter. Science 345:650–653. https://doi.org/10.1126/science.1253338, 1408.2050

Lugaro M, Tagliente G, Karakas AI, Milazzo PM, Käppeler F, Davis AM, Savina MR (2014b) The impact of updated Zr neutron-capture cross sections and new asymptotic giant branch models on our understanding of the S process and the origin of stardust. Astrophys J 780:95. https://doi.org/10.1088/0004-637X/780/1/95, 1311.2660

Lugaro M, Karakas AI, Bruno CG, Aliotta M, Nittler LR, Bemmerer D, Best A, Boeltzig A, Broggini C, Caciolli A, Cavanna F, Ciani GF, Corvisiero P, Davinson T, Depalo R, di Leva A, Elekes Z, Ferraro F, Formicola A, Fülöp Z, Gervino G, Guglielmetti A, Gustavino C, Gyürky G, Imbriani G, Junker M, Menegazzo R, Mossa V, Pantaleo FR, Piatti D, Prati P, Scott DA, Straniero O, Strieder F, Szücs T, Takács MP, Trezzi D (2017) Origin of meteoritic stardust unveiled by a revised proton-capture rate of ^{17}O. Nat Astron 1:0027. https://doi.org/10.1038/s41550-016-0027, 1703.00276

Lugaro M, Karakas AI, Pető M, Plachy E (2018) Do meteoritic silicon carbide grains originate from asymptotic giant branch stars of super-solar metallicity? Geochim Cosmochim Acta 221:6–20. https://doi.org/10.1016/j.gca.2017.06.006

Marhas KK, Hoppe P, Ott U (2007) NanoSIMS studies of Ba isotopic compositions in single presolar silicon carbide grains from AGB stars and supernovae. Meteorit Planet Sci 42:1077–1101

McDonald AB, Ahmad QR, Allen RC, Andersen TC, Anglin JD, Barton JC, Beier EW, Bercovitch M, Bigu J, Biller SD, Black RA, Blevis I, Boardman RJ, Boger J, Bonvin E, Boulay MG, Bowler MG, Bowles TJ, Brice SJ, Browne MC, Bullard TV, Bühler G, Cameron J, Chan YD,

Chen HH, Chen M, Chen X, Cleveland BT, Clifford ETH, Cowan JHM, Cowen DF, Cox GA, Dai X, Dalnoki-Veress F, Davidson WF, Doe PJ, Doucas G, Dragowsky MR, Duba CA, Duncan FA, Dunford M, Dunmore JA, Earle ED, Elliott SR, Evans HC, Ewan GT, Farine J, Fergani H, Ferraris AP, Ford RJ, Formaggio JA, Fowler MM, Frame K, Frank ED, Frati W, Gagnon N, Germani JV, Gil S, Graham K, Grant DR, Hahn RL, Hallin AL, Hallman ED, Hamer AS, Hamian AA, Handler WB, Haq RU, Hargrove CK, Harvey PJ, Hazama R, Heeger KM, Heintzelman WJ, Heise J, Helmer RL, Hepburn JD, Heron H, Hewett J, Hime A, Howe M, Hykawy JG, Isaac MCP, Jagam P, Jelley NA, Jillings C, Jonkmans G, Kazkaz K, Keener PT, Klein JR, Knox AB, Komar RJ, Kouzes R, Kutter T, Kyba CCM, Law J, Lawson IT, Lay M, Lee HW, Lesko KT, Leslie JR, Levine I, Locke W, Luoma S, Lyon J, Majerus S, Mak HB, Maneira J, Manor J, Marino AD, McCauley N, McDonald DS, McFarlane K, McGregor G, Drees RM, Mifflin C, Miller GG, Milton G, Moffat BA, Moorhead M, Nally CW, Neubauer MS, Newcomer FM, Ng HS, Noble AJ, Norman EB, Novikov VM, O'Neill M, Okada CE, Ollerhead RW, Omori M, Orrell JL, Oser SM, Poon AWP, Radcliffe TJ, Roberge A, Robertson BC, Robertson RGH, Rosendahl SSE, Rowley JK, Rusu VL, Saettler E, Schaffer KK, Schwendener MH, Schülke A, Seifert H, Shatkay M, Simpson JJ, Sims CJ, Sinclair D, Skensved P, Smith AR, Smith MWE, Spreitzer T, Starinsky N, Steiger TD, Stokstad RG, Stonehill LC, Storey RS, Sur B, Tafirout R, Tagg N, Tanner NW, Taplin RK, Thorman M, Thornewell PM, Trent PT, Tserkovnyak YI, van Berg R, van de Water RG, Virtue CJ, Waltham CE, Wang J, Wark DL, West N, Wilhelmy JB, Wilkerson JF, Wilson JR, Wittich P, Wouters JM, Yeh M (2002) Direct evidence for neutrino flavor transformation from neutral-current interactions in SNO. In: Elias V, Epp R, Myers RC (eds) Theoretical physics: MRST 2002, American Institute of Physics conference series, vol 646. pp 43–58. https://doi.org/10.1063/1.1524553

McWilliam A, Lambert DL (1988) Isotopic magnesium abundances in stars. Mon Not R Astron Soc 230:573–585

Mikheyev SP, Smirnov AY (1985) Resonance enhancement of oscillations in matter and solar neutrino spectroscopy. Yadernaya Fizika 42:1441–1448

Mowlavi N, Meynet G (2000) Aluminum 26 production in asymptotic giant branch stars. Astron Astrophys 361:959–976

Mowlavi N, Goriely S, Arnould M (1998) The survival of ^{205}Pb in intermediate-mass AGB stars. Astron Astrophys 330:206–214. arXiv:astro-ph/9711025

Murphy RJ, Share GH (2005) What gamma-ray deexcitation lines reveal about solar-flares. Adv Space Res 35:1825–1832. https://doi.org/10.1016/j.asr.2005.03.004

Murphy RJ, Share GH, Skibo JG, Kozlovsky B (2005) The physics of positron annihilation in the solar atmosphere. Astrophys J Suppl 161:495–519. https://doi.org/10.1086/452634

Nanni A, Bressan A, Marigo P, Girardi L (2013) Evolution of thermally pulsing asymptotic giant branch stars - II. Dust production at varying metallicity. Mon Not R Astron Soc 434:2390–2417. https://doi.org/10.1093/mnras/stt1175, 1306.6183

Neyskens P, van Eck S, Jorissen A, Goriely S, Siess L, Plez B (2015) The temperature and chronology of heavy-element synthesis in low-mass stars. Nature 517:174–176. https://doi.org/10.1038/nature14050, 1601.05640

Nichols RH Jr, Hohenberg CM, Amari S, Lewis RS (1991) ^{22}Ne-E(H) and ^{4}He Measured in individual SiC grains using laser gas extraction. Meteoritics 26:377

Nicolussi GK, Davis AM, Pellin MJ, Lewis RS, Clayton RN, Amari S (1997) s-process zirconium in presolar silicon carbide grains. Science 277:1281–1283. https://doi.org/10.1126/science.277.5330.1281

Nicolussi GK, Pellin MJ, Lewis RS, Davis AM, Amari S, Clayton RN (1998a) Molybdenum isotopic composition of individual presolar silicon carbide grains from the murchison meteorite. Geochim Cosmochim Acta 62:1093–1104. https://doi.org/10.1016/S0016-7037(98)00038-6

Nicolussi GK, Pellin MJ, Lewis RS, Davis AM, Clayton RN, Amari S (1998b) Strontium isotopic composition in individual circumstellar silicon carbide grains: a record of s-Process nucleosynthesis. Phys Rev Lett 81:3583–3586. https://doi.org/10.1103/PhysRevLett.81.3583

Nittler LR, Hoppe P, Alexander CMO, Amari S, Eberhardt P, Gao X, Lewis RS, Strebel R, Walker RM, Zinner E (1995) Silicon Nitride from Supernovae. Astrophys J 453:L25. https://doi.org/10.1086/309743

Nittler LR, Alexander CMO, Gao X, Walker RM, Zinner E (1997) Stellar sapphires: the properties and origins of presolar AL 2O 3 in meteorites. Astrophys J 483:475. https://doi.org/10.1086/304234

Nittler LR, Alexander CMO, Gallino R, Hoppe P, Nguyen AN, Stadermann FJ, Zinner EK (2008) Aluminum-, calcium- and titanium-rich oxide stardust in ordinary chondrite meteorites. Astrophys J 682:1450–1478. https://doi.org/10.1086/589430, 0804.2866

Nollett KM, Busso M, Wasserburg GJ (2003) Cool bottom processes on the thermally pulsing asymptotic giant branch and the isotopic composition of circumstellar dust grains. Astrophys J 582:1036–1058. https://doi.org/10.1086/344817, arXiv:astro-ph/0211271

Ott U, Begemann F (1990) Discovery of s-process barium in the Murchison meteorite. Astrophys J 353:L57–L60. https://doi.org/10.1086/185707

Palmerini S, La Cognata M, Cristallo S, Busso M (2011) Deep mixing in evolved stars. I. The effect of reaction rate revisions from C to Al. Astrophys J 729:3. https://doi.org/10.1088/0004-637X/729/1/3, 1011.3948

Palmerini S, Trippella O, Busso M, Vescovi D, Petrelli M, Zucchini A, Frondini F (2018) s-Processing from MHD-induced mixing and isotopic abundances in presolar SiC grains. Geochim Cosmochim Acta 221:21–36. https://doi.org/10.1016/j.gca.2017.05.030, 1711.03039

Pérez-Mesa V, Zamora O, García-Hernández DA, Plez B, Manchado A, Karakas AI, Lugaro M (2017) Rubidium and zirconium abundances in massive Galactic asymptotic giant branch stars revisited. Astron Astrophys 606:A20. https://doi.org/10.1051/0004-6361/201731245, 1706.02268

Pignatari M, Gallino R, Straniero O, Reifarth R, Käppeler F, Davis AM (2004) Stellar origin of the meteoritic Xe-S anomalous component. Memorie della Societa Astronomica Italiana 75:182

Pignatari M, Gallino R, Amari S, Davis AM (2006) Krypton in presolar mainstream SiC grains from AGB stars. Memorie della Societa Astronomica Italiana 77:897

Pignatari M, Gallino R, Heil M, Wiescher M, Käppeler F, Herwig F, Bisterzo S (2010) The weak s-Process in massive stars and its dependence on the neutron capture cross sections. Astrophys J 710:1557–1577. https://doi.org/10.1088/0004-637X/710/2/1557

Pignatari M, Wiescher M, Timmes FX, de Boer RJ, Thielemann FK, Fryer C, Heger A, Herwig F, Hirschi R (2013) Production of carbon-rich presolar grains from massive stars. Astrophys J 767:L22 https://doi.org/10.1088/2041-8205/767/2/L22, 1303.3374

Pignatari M, Herwig F, Hirschi R, Bennett M, Rockefeller G, Fryer C, Timmes FX, Ritter C, Heger A, Jones S, Battino U, Dotter A, Trappitsch R, Diehl S, Frischknecht U, Hungerford A, Magkotsios G, Travaglio C, Young P (2016) NuGrid stellar data set. I. Stellar yields from H to Bi for stars with Metallicities Z = 0.02 and Z = 0.01. Astrophys J Suppl 225:24. https://doi.org/10.3847/0067-0049/225/2/24, 1307.6961

Podosek FA, Prombo CA, Amari S, Lewis RS (2004) s-Process Sr isotopic compositions in Presolar SiC from the murchison meteorite. Astrophys J 605:960–965. https://doi.org/10.1086/382650

Prombo CA, Podosek FA, Amari S, Lewis RS (1993) S-process BA isotopic compositions in presolar SiC from the Murchison meteorite. Astrophys J 410:393–399. https://doi.org/10.1086/172756

Raiteri CM, Gallino R, Busso M (1992) S-processing in massive stars as a function of metallicity and interpretation of observational trends. Astrophys J 387:263–275. https://doi.org/10.1086/171078

Ramaty R, Mandzhavidze N, Kozlovsky B, Murphy RJ (1995) Solar atmopheric abundances and energy content in flare accelerated ions from gamma-ray spectroscopy. Astrophys J 455:L193. https://doi.org/10.1086/309841

Rauscher T, Thielemann FK (2000) Astrophysical reaction rates from statistical model calculations. At Data Nucl Data Tables 75:1–351. https://doi.org/10.1006/adnd.2000.0834, arXiv:astro-ph/0004059

Raut R, Tonchev AP, Rusev G, Tornow W, Iliadis C, Lugaro M, Buntain J, Goriely S, Kelley JH, Schwengner R, Banu A, Tsoneva N (2013) Cross-section measurements of the Kr86(γ,n) reaction to probe the s-Process branching at Kr85. Phys Rev Lett 111(11):112501. https://doi.org/10.1103/PhysRevLett.111.112501, 1309.4159

Roederer IU, Karakas AI, Pignatari M, Herwig F (2016) The diverse origins of neutron-capture elements in the metal-poor star HD 94028: possible detection of products of I-Process nucleosynthesis. Astrophys J 821:37. https://doi.org/10.3847/0004-637X/821/1/37, 1603.00036

Rugel G, Faestermann T, Knie K, Korschinek G, Poutivtsev M, Schumann D, Kivel N, Günther-Leopold I, Weinreich R, Wohlmuther M (2009) New measurement of the Fe60 half-life. Phys Rev Lett 103(7):072502. https://doi.org/10.1103/PhysRevLett.103.072502

Savina MR, Davis AM, Tripa CE, Pellin MJ, Clayton RN, Lewis RS, Amari S, Gallino R, Lugaro M (2003a) Barium isotopes in individual presolar silicon carbide grains from the Murchison meteorite. Geochim Cosmochim Acta 67:3201–3214. https://doi.org/10.1016/S0016-7037(03)00083-8

Savina MR, Pellin MJ, Tripa CE, Veryovkin IV, Calaway WF, Davis AM (2003b) Analyzing individual presolar grains with CHARISMA. Geochim Cosmochim Acta 67:3215–3225. https://doi.org/10.1016/S0016-7037(03)00082-6

Savina MR, Davis AM, Tripa CE, Pellin MJ, Gallino R, Lewis RS, Amari S (2004) Extinct technetium in silicon carbide stardust grains: implications for stellar nucleosynthesis. Science 303:649–652. https://doi.org/10.1126/science.3030649

Sedlmayr E, Dominik C (1995) Dust driven winds. Space Sci Rev 73:211–272. https://doi.org/10.1007/BF00751238

Serenelli AM, Haxton WC, Peña-Garay C (2011) Solar models with accretion. I. Application to the solar abundance problem. Astrophys J 743:24. https://doi.org/10.1088/0004-637X/743/1/24, 1104.1639

Siess L, Arnould M (2008) Production of ^{26}Al by super-AGB stars. Astron Astrophys 489:395–402. https://doi.org/10.1051/0004-6361:200810147

Smith VV, Lambert DL (1986) The chemical composition of red giants. II - helium burning and the s-process in the MS and S stars. Astrophys J 311:843–863. https://doi.org/10.1086/164823

Sneden C, Cowan JJ, Lawler JE, Burles S, Beers TC, Fuller GM (2002) Europium isotopic abundances in very metal poor stars. Astrophys J 566:L25–L28. https://doi.org/10.1086/339471, arXiv:astro-ph/0201456

Sneden C, Cowan JJ, Gallino R (2008) Neutron-capture elements in the early galaxy. Annu Rev Astron Astrophys 46:241–288. https://doi.org/10.1146/annurev.astro.46.060407.145207

Speck AK, Barlow MJ, Sylvester RJ, Hofmeister AM (2000) Dust features in the 10-mu m infrared spectra of oxygen-rich evolved stars. Astron Astrophys Suppl 146:437–464. https://doi.org/10.1051/aas:2000274

Speck AK, Corman AB, Wakeman K, Wheeler CH, Thompson G (2009) Silicon carbide absorption features: dust formation in the outflows of extreme carbon stars. Astrophys J 691:1202–1221. https://doi.org/10.1088/0004-637X/691/2/1202, 0810.2599

Stancliffe RJ, Chieffi A, Lattanzio JC, Church RP (2009) Why do low-mass stars become red giants? Publications of the Astronomical Society of Australia 26:203–208. https://doi.org/10.1071/AS08060, 0902.0406

Stephan T, Trappitsch R, Davis AM, Pellin MJ, Rost D, Savina MR, Yokochi R, Liu N (2016) CHILI - the chicago instrument for laser ionization - a new tool for isotope measurements in cosmochemistry. Int J Mass Spectrom 407:1–15. https://doi.org/10.1016/j.ijms.2016.06.001

Straniero O, Imbriani G, Strieder F, Bemmerer D, Broggini C, Caciolli A, Corvisiero P, Costantini H, Cristallo S, DiLeva A, Formicola A, Elekes Z, Fülöp Z, Gervino G, Guglielmetti A, Gustavino C, Gyürky G, Junker M, Lemut A, Limata B, Marta M, Mazzocchi C, Menegazzo R, Piersanti L, Prati P, Roca V, Rolfs C, Rossi Alvarez C, Somorjai E, Terrasi F, Trautvetter HP (2013) Impact of a revised ^{25}Mg(p, γ)^{26}Al reaction rate on the operation of the Mg-Al cycle. Astrophys J 763:100. https://doi.org/10.1088/0004-637X/763/2/100, 1211.6661

Takahashi K, Yokoi K (1987) Beta-decay rates of highly ionized heavy atoms in stellar interiors. At Data Nucl Data Tables 36:375. https://doi.org/10.1016/0092-640X(87)90010-6

Tatischeff V, Kozlovsky B, Kiener J, Murphy RJ (2006) Delayed X- and gamma-ray line emission from solar flare radioactivity. Astrophys J Suppl 165:606–617. https://doi.org/10.1086/505112, arXiv:astro-ph/0604325

Thielemann FK, Arcones A, Käppeli R, Liebendörfer M, Rauscher T, Winteler C, Fröhlich C, Dillmann I, Fischer T, Martinez-Pinedo G, Langanke K, Farouqi K, Kratz KL, Panov I, Korneev IK (2011) What are the astrophysical sites for the r-process and the production of heavy elements? Prog Part Nucl Phys 66:346–353. https://doi.org/10.1016/j.ppnp.2011.01.032

Trappitsch R, Stephan T, Savina MR, Davis AM, Pellin MJ, Rost D, Gyngard F, Gallino R, Bisterzo S, Cristallo S, Dauphas N (2018) Simultaneous iron and nickel isotopic analyses of presolar silicon carbide grains. Geochim Cosmochim Acta 221:87–108. https://doi.org/10.1016/j.gca.2017.05.031

Travaglio C, Gallino R, Amari S, Zinner E, Woosley S, Lewis RS (1999) Low-density graphite grains and mixing in type II supernovae. Astrophys J 510:325–354. https://doi.org/10.1086/306551

Treffers R, Cohen M (1974) High-resolution spectra of cool stars in the 10- and 20-micron regions. Astrophys J 188:545–552. https://doi.org/10.1086/152746

Trigo-Rodriguez JM, Anibal Garcia-Hernandez D, Lugaro M, Karakas AI, van Raai M, Garcia Lario P, Manchado A (2009) The role of massive Agb stars in the early solar system composition. Meteorit Planet Sci 44:627–641

Uberseder E, Reifarth R, Schumann D, Dillmann I, Pardo CD, Görres J, Heil M, Käppeler F, Marganiec J, Neuhausen J, Pignatari M, Voss F, Walter S, Wiescher M (2009) Measurement of the Fe60(n,γ)^{61}Fe cross section at stellar temperatures. Phys Rev Lett 102(15):151101. https://doi.org/10.1103/PhysRevLett.102.151101

Uberseder E, Adachi T, Aumann T, Beceiro-Novo S, Boretzky K, Caesar C, Dillmann I, Ershova O, Estrade A, Farinon F, Hagdahl J, Heftrich T, Heil M, Heine M, Holl M, Ignatov A, Johansson HT, Kalantar N, Langer C, Le Bleis T, Litvinov YA, Marganiec J, Movsesyan A, Najafi MA, Nilsson T, Nociforo C, Panin V, Pietri S, Plag R, Prochazka A, Rastrepina G, Reifarth R, Ricciardi V, Rigollet C, Rossi DM, Savran D, Simon H, Sonnabend K, Streicher B, Terashima S, Thies R, Togano Y, Volkov V, Wamers F, Weick H, Weigand M, Wiescher M, Wimmer C, Winckler N, Woods PJ (2014) First experimental constraint on the Fe59(n,γ)Fe60 reaction cross section at astrophysical energies via the coulomb dissociation of Fe60. Phys Rev Lett 112(21):211101. https://doi.org/10.1103/PhysRevLett.112.211101

Uttenthaler S, Lebzelter T, Palmerini S, Busso M, Aringer B, Lederer MT (2007) Low-mass lithium-rich AGB stars in the Galactic bulge: evidence for cool bottom processing? Astron Astrophys 471:L41–L45, https://doi.org/10.1051/0004-6361:20077879, 0707.1380

van Raai MA, Lugaro M, Karakas AI, Iliadis C (2008) Reaction rate uncertainties and ^{26}Al in AGB silicon carbide stardust. Astron Astrophys 478:521–526. https://doi.org/10.1051/0004-6361:20078307, 0712.3702

van Raai MA, Lugaro M, Karakas AI, García-Hernández DA, Yong D (2012) Rubidium, zirconium, and lithium production in intermediate-mass asymptotic giant branch stars. Astron Astrophys 540:A44. https://doi.org/10.1051/0004-6361/201117896, 1202.2620

Verchovsky AB, Wright IP, Pillinger CT (2004) Astrophysical significance of asymptotic giant branch stellar wind energies recorded in meteoritic SiC grains. Astrophys J 607:611–619. https://doi.org/10.1086/383230

Vollmer C, Hoppe P, Brenker FE (2008) Si isotopic compositions of presolar silicate grains from red giant stars and supernovae. Astrophys J 684:611–617. https://doi.org/10.1086/589913

Wallner A, Bichler M, Buczak K, Dillmann I, Käppeler F, Karakas A, Lederer C, Lugaro M, Mair K, Mengoni A, Schätzel G, Steier P, Trautvetter HP (2016) Accelerator mass spectrometry measurements of the ^{13}C (n,γ)^{14}C and ^{14}N(n,p)^{14}C cross sections. Phys Rev C 93(4):045803. https://doi.org/10.1103/PhysRevC.93.045803

Wanajo S, Nomoto K, Janka H, Kitaura FS, Müller B (2009) Nucleosynthesis in electron capture supernovae of asymptotic giant branch stars. Astrophys J 695:208–220. https://doi.org/10.1088/0004-637X/695/1/208, 0810.3999

Wasserburg GJ, Busso M, Gallino R, Raiteri CM (1994) Asymptotic giant branch stars as a source of short-lived radioactive nuclei in the solar nebula. Astrophys J 424:412–428. https://doi.org/10.1086/173899

Wasserburg GJ, Boothroyd AI, Sackmann IJ (1995) Deep circulation in red giant stars: a solution to the carbon and oxygen isotope puzzles? Astrophys J 447:L37. https://doi.org/10.1086/309555

Wasserburg GJ, Busso M, Gallino R, Nollett KM (2006) Short-lived nuclei in the early solar system: possible AGB sources. Nucl Phys A 777:5–69. https://doi.org/10.1016/j.nuclphysa.2005.07.015, arXiv:astro-ph/0602551

Whittet DCB (2002) Dust in the galactic environment. Series in astronomy and astrophysics, 2nd edn. Institute of Physics (IOP) Publishing, Bristol

Willson LA (2000) Mass loss from cool stars: impact on the evolution of stars and stellar populations. Annu Rev Astron Astrophys 38:573–611. https://doi.org/10.1146/annurev.astro.38.1.573

Wolfenstein L (1978) Neutrino oscillations in matter. Phys Rev D 17:2369–2374. https://doi.org/10.1103/PhysRevD.17.2369

Wood PR (1979) Pulsation and mass loss in Mira variables. Astrophys J 227:220–231. https://doi.org/10.1086/156721

Yin QZ, Lee CTA, Ott U (2006) Signatures of the s-Process in presolar silicon carbide grains: barium through hafnium. Astrophys J 647:676–684. https://doi.org/10.1086/505188

Zinner E, Amari S, Lewis RS (1991) S-process Ba, Nd, and SM in presolar SiC from the Murchison meteorite. Astrophys J 382:L47–L50. https://doi.org/10.1086/186210

Zinner E, Nittler LR, Gallino R, Karakas AI, Lugaro M, Straniero O, Lattanzio JC (2006) Silicon and carbon isotopic ratios in AGB stars: SiC grain data, models, and the galactic evolution of the Si isotopes. Astrophys J 650:350–373. https://doi.org/10.1086/506957

Zinner E, Amari S, Guinness R, Jennings C, Mertz AF, Nguyen AN, Gallino R, Hoppe P, Lugaro M, Nittler LR, Lewis RS (2007) NanoSIMS isotopic analysis of small presolar grains: Search for $Si_3\ N_4$ grains from AGB stars and Al and Ti isotopic compositions of rare presolar SiC grains. Geochim Cosmochim Acta 71:4786–4813. https://doi.org/10.1016/j.gca.2007.07.012